



NOVEL POLYMERIC MEMBRANES FOR ARTIFICIAL PHOTOSYNTHESIS

Alireza Zare

ADVERTIMENT. L'accés als continguts d'aquesta tesi doctoral i la seva utilització ha de respectar els drets de la persona autora. Pot ser utilitzada per a consulta o estudi personal, així com en activitats o materials d'investigació i docència en els termes establerts a l'art. 32 del Text Refós de la Llei de Propietat Intel·lectual (RDL 1/1996). Per altres utilitzacions es requereix l'autorització prèvia i expressa de la persona autora. En qualsevol cas, en la utilització dels seus continguts caldrà indicar de forma clara el nom i cognoms de la persona autora i el títol de la tesi doctoral. No s'autoritza la seva reproducció o altres formes d'explotació efectuades amb finalitats de lucre ni la seva comunicació pública des d'un lloc aliè al servei TDX. Tampoc s'autoritza la presentació del seu contingut en una finestra o marc aliè a TDX (framing). Aquesta reserva de drets afecta tant als continguts de la tesi com als seus resums i índexs.

ADVERTENCIA. El acceso a los contenidos de esta tesis doctoral y su utilización debe respetar los derechos de la persona autora. Puede ser utilizada para consulta o estudio personal, así como en actividades o materiales de investigación y docencia en los términos establecidos en el art. 32 del Texto Refundido de la Ley de Propiedad Intelectual (RDL 1/1996). Para otros usos se requiere la autorización previa y expresa de la persona autora. En cualquier caso, en la utilización de sus contenidos se deberá indicar de forma clara el nombre y apellidos de la persona autora y el título de la tesis doctoral. No se autoriza su reproducción u otras formas de explotación efectuadas con fines lucrativos ni su comunicación pública desde un sitio ajeno al servicio TDR. Tampoco se autoriza la presentación de su contenido en una ventana o marco ajeno a TDR (framing). Esta reserva de derechos afecta tanto al contenido de la tesis como a sus resúmenes e índices.

WARNING. Access to the contents of this doctoral thesis and its use must respect the rights of the author. It can be used for reference or private study, as well as research and learning activities or materials in the terms established by the 32nd article of the Spanish Consolidated Copyright Act (RDL 1/1996). Express and previous authorization of the author is required for any other uses. In any case, when using its content, full name of the author and title of the thesis must be clearly indicated. Reproduction or other forms of for profit use or public communication from outside TDX service is not allowed. Presentation of its content in a window or frame external to TDX (framing) is not authorized either. These rights affect both the content of the thesis and its abstracts and indexes.



Novel Polymeric Membranes for Artificial Photosynthesis

Alireza Zare

DOCTORAL THESIS

2022

UNIVERSITAT ROVIRA i VIRGILI



UNIVERSITAT ROVIRA I VIRGILI
NOVEL POLYMERIC MEMBRANES FOR ARTIFICIAL PHOTOSYNTHESIS
Alireza Zare

Department of Chemical Engineering

Novel Polymeric Membranes for Artificial Photosynthesis

Doctoral Thesis

By

Alireza Zare

Thesis Supervisor: Dr. Marta Giamberini

Thesis Co-Supervisor: Dr. José Antonio Reina Lozano



**UNIVERSITAT
ROVIRA i VIRGILI**

Tarragona

2022

UNIVERSITAT ROVIRA I VIRGILI
NOVEL POLYMERIC MEMBRANES FOR ARTIFICIAL PHOTOSYNTHESIS
Alireza Zare



Escola Tècnica Superior d'Enginyeria Química
Departament d'Enginyeria Química

Avinguda dels Països Catalans, 26
43007 Tarragona (Spain)
Tel. 977559603/04
Fax: 977559621

FAIG CONSTAR que aquest treball, titulat "Noves membranes polimèriques per a la fotosíntesi artificial", que presenta Alireza Zare per a l'obtenció del títol de Doctor, ha estat realitzat sota la meva direcció al Departament d'Enginyeria Química d'aquesta universitat.

HAGO CONSTAR que el presente trabajo, titulado "Nuevas membranas poliméricas para fotosíntesis artificial", que presenta Alireza Zare para la obtención del título de Doctor, ha sido realizado bajo mi dirección en el Departamento de Ingeniería Química de esta universidad.

I STATE that the present study, entitled "Novel polymeric membranes for artificial photosynthesis", presented by Alireza Zare for the award of the degree of Doctor, has been carried out under my supervision at the Department of Chemical Engineering of this university.

Tarragona, 2 de juny de 2022 / Tarragona, 2 de junio de 2022 / Tarragona, 2nd of June, 2022.

El/s director/s de la tesi doctoral
El/los director/es de la tesis doctoral
Doctoral Thesis Supervisor/s

[signatura] / [firma] / [signature]

Dr. Marta Giamberini

[signatura] / [firma] / [signature]

Dr. José Antonio Reina Lozano

UNIVERSITAT ROVIRA I VIRGILI
NOVEL POLYMERIC MEMBRANES FOR ARTIFICIAL PHOTOSYNTHESIS
Alireza Zare

Acknowledgment

The last three years have been filled with wonderful adventures, a lot of hard work, and much growth. I would like to express my appreciation to all the people who have accompanied me over these years and so have either directly or indirectly contributed to the dissertation.

First and foremost, I would like to record my sincere and heartfelt gratitude to my incredible and esteemed advisers, respected Dr. Marta Giamberini and Dr. José Antonio Reina Lozano for their supervision, invaluable advice, tutelage, and patience, as well as for providing me with remarkable experience and knowledge throughout the work. Above all, and perhaps most importantly, they trusted me and provided me with unflinching encouragement and continuous support in all steps of my Ph.D. life. Their immense knowledge and plentiful experience have encouraged me all the time in my academic research and daily life. During the course of my Ph.D. research, I could not have dreamed of having more helpful and pleasant advisors.

I would like to extend my thanks and appreciation to Chemical Engineering Department for all the support, advice, assistance, seminars, and training they provided us to further our knowledge, qualifications, and skills. To Núria Juanpere and Dr Alex Fragoso for their support and assistance. Always willing to help me in a friendly and professional manner, and attention to each of my requests.

My special sincere thanks also goes to Dr Alberto Puga, Dr Adrianna Nogalska and Dr Xavier Montane for successful collaboration, which has resulted in jointly published articles. I would be much obliged if express my deepest gratitude to MEMTEC group, full of extraordinary, smart, and approachable members with a great collaboration and support spirit. Thank you for your help: Dr. Ricard Garcia Valls, Dr. Bartosz Tylkowski, Dr Anna Trojanowska and Josefa Lázaro.

I would like to convey my gratefulness especially to an incredible person Dr. Àngels Serra for her hospitality, kindness and interesting conversations.

I would like to thank the following people, without whom I would not have been able to complete this research! Special thanks to Ramon, Debora, Francesco, and Mercè for their invaluable advice, continuous support, and patience during my sample analysis at every stage of the research project.

Additional appreciation goes to the Institute for Polymers, Composites and Biomaterials (IPCB-CNR), Italy, where I did my research stay. Please, accept my deepest gratitude for all your support regarding the administrative process and socialization activities. I am especially grateful to Dr. Pierfrancesco Cerruti for his tremendous help and valuable advice during my research stay. I would like to thank all the kind people whom I met in Italy.

In addition, I would like to express my deepest gratitude to my excellent colleagues in Lab 330, 312, 212 and Eurecat. I have felt privileged to be able to work in such an inspiring and friendly atmosphere. I will remember each and every one of you! Of course, I could not forget to mention you, David, Issacs, Francesco, Claudio, Jordi, Adrià, Federico, Sasan, Belén, Yaride, Yousof, Yonas, Anna, Tahere, and Andreu. From the first moment we met, we became very close friends. Thank you for your friendship and all your support when things would get a bit discouraging.

My deepest gratitude goes to my best friends- Tajiran, Maryam, Vahid, and Yaghoub- whose dedication, unwavering support, and unflinching confidence in me, have taken the load off my shoulder. Thank you so much for your companionship, encouragement, and support.

My heartfelt gratitude goes to my amazing family. I am extremely grateful to my parents, sisters, and brothers for their love, understanding, help, and support. My family inspired me to follow my heart as well as my mind to achieve the goals I set for myself. It would not have been possible without the support of my beautiful family. I love you! I owe my mother and older brother, special thanks; I have missed you, and you should be here to be proud of me now! I learned from you how to pursue my life's objectives with perseverance and self-confidence. Many thanks for all the life lessons and support that you shared with me! I love you!

In conclusion, I would like to thank everybody who was important to the successful realization of the thesis and express my regret that I could not mention you all individually.

Finally, financial support from the European Union's Horizon 2020 research and innovation programme under the Marie Skłodowska-Curie grant agreement No. 713679 and from the Universitat Rovira i Virgili (URV) are gratefully acknowledged.

Table of Contents

Chapter 1. General Introduction and Objective.....	1
1.1 Introduction.....	3
1.2 Membranes for energy production and storage.....	5
1.2.1 Artificial photosynthesis and fuel cells: an overview	5
1.2.2 Biomimetic ion transport: from biological systems to supramolecular self-assembled structures.....	9
1.2.3 Liquid-crystalline polymers	11
1.2.4 Supramolecular self-assembly of side-chain liquid-crystalline polymers (SCLCPs)	14
1.3 Membranes for CO ₂ capture.....	17
1.3.1 Membrane contactors in CO ₂ capture	18
1.3.2 Membranes for CO ₂ capture	20
1.3.3 Absorbents for CO ₂ capture	26
1.4 References.....	27
1.5 Objectives of the thesis	37
Chapter 2. Membranes for cation transport based on dendronized Poly (epichlorohydrin-co-ethylene oxide). Part 1: the effect of the dendron amount and column orientation on the copolymer mobility.....	39
2.1 Introduction.....	41
2.2 Materials and Methods.....	43
2.2.1 Materials	43
2.2.2 Membrane preparation	44
2.2.3 Characterization techniques	45
2.3 Results.....	46
2.3.1 Thermal, microscopic and X-ray diffraction characterization	47
2.3.2 Optimization of the orientation procedure	50
2.3.3 Dynamic-mechanical thermal analysis (DMTA).....	53

2.3.4	Dielectric thermal analysis (DETA).....	54
2.4	Conclusions.....	61
2.5	References.....	62
Chapter 3. Membranes for cation transport based on dendronized Poly (epichlorohydrin-co-ethylene oxide). Part 2: membrane characterization and transport properties67
3.1	Introduction.....	69
3.2	Materials and Methods.....	72
3.2.1	Materials	72
3.2.2	Membrane preparation and characterizations	72
3.3	Results.....	75
3.3.1	Morphological characterization, wettability and water uptake	75
3.3.2	Transport properties	80
3.4	Conclusions.....	84
3.5	References.....	85
Chapter 4. Polymer blends for improved CO₂ capture membranes.....		89
4.1	Introduction.....	91
4.2	Materials and Methods.....	93
4.2.1	Materials	93
4.2.2	Additive preparation	93
4.2.3	Membrane preparation	94
4.2.4	Membranes characterization	94
4.3	Results and Discussion.....	97
4.4	Conclusions.....	107
4.5	References.....	108
Chapter 5. Facilitated direct air capture of CO₂ in polysulfone membrane contactors by improving stability and hydrophobicity of amine additives111
5.1	Introduction.....	113
5.2	Materials and Methods.....	116

5.2.1	Materials	116
5.2.2	Additive preparation	116
5.2.3	Membrane preparation	117
5.2.4	Characterizations.....	117
5.3	Results.....	121
5.3.1	Additive synthesis and blended membrane preparation and morphological characterization.....	121
5.3.2	Additive distribution and membranes' chemical stability	126
5.3.3	Mechanical characterization	130
5.3.4	CO ₂ capture performance.....	132
5.4	Conclusions.....	136
5.5	References.....	137
Chapter 6. General Conclusions.....		141
Appendices.....		147

UNIVERSITAT ROVIRA I VIRGILI
NOVEL POLYMERIC MEMBRANES FOR ARTIFICIAL PHOTOSYNTHESIS
Alireza Zare

List of figures

Figure 1.1 Natural sources for the obtention of renewable energy.	3
Figure 1.2 Number of peer-reviewed scientific articles published by decades since 1932 in the field of “membranes in energy systems” (Source: Web of Science).	5
Figure 1.3 Schematic representation of a Direct Methanol Fuel Cell (DMFC).	6
Figure 1.4 Chemical structure of Nafion.	8
Figure 1.5 Representation of the proton transport mechanism in PEM: a) Grotthuss mechanism; b) Vehicular mechanism.	8
Figure 1.6 Types of natural transport across cell membranes: a) Carrier and b) Channel.	10
Figure 1.7 Ion channels by cylindrical packing of crown ether rings [48].	10
Figure 1.8 Schematic representation of the self-assembly process of TMV.	11
Figure 1.9 Schematic illustration of the molecular arrangement in different states of matter.	12
Figure 1.10 Types of LC mesogens as stated by their shape: a) Calamitic mesogens and b) Discotic mesogens.	13
Figure 1.11 Organization of molecules in different thermotropic LC mesophases.	13
Figure 1.12 Representation of the structure of: a) MCLCPs and b) SCLCPs.	14
Figure 1.13 Schematic representation of the self-assembly of SCLCPs into a hexagonal columnar structure.	15
Figure 1.14 Chemical structure of modified polymers with Tap mesogenic group: a) [P(ECH-co-EO)], b) PECH and c) PAZE [44,56,57].	15
Figure 1.15 Schematic of ion transportation in biomimetic membranes [59].	17
Figure 1.16 Example of a gas-liquid membrane contactor for CO ₂ capture.	19
Figure 1.17 Representation of the surface modification of a ceramic material with FAS.	21
Figure 1.18 Chemical structure of common polymers employed as membrane contactors.	22
Figure 1.19 Scheme of natural stomata (left), an artificial photosynthetic system (APS), water-splitting APS systems, to utilize solar energy through the conversion of photon-to-fuel by mimicking natural photosynthesis, electroreduction of CO ₂ system (right).	24
Figure 1.20 Chemical structure of some absorbents used to capture CO ₂	27
Figure 2.1 Optical micrographs under crossed polarizers of CP40 at 300 K (a), 335 K (b) and 433 K (c).	48
Figure 2.2 WAXD at room temperature of: CP0 (a), CP40 (b) and CP20 (c). Inset: SAXD of CP40 (b) and CP20 (c).	48
Figure 2.3 WAXD of CP40 at: 293 K (a), 323 K (b) and 393 K (c).	49

Figure 2.4 Debye ring pattern of CP40 (samples (a) – (d)) after the thermal treatment with different conditions.....	53
Figure 2.5 DMTA analysis for CP0, CP20 and CP40 samples. (a) $\tan\delta$ (b) loss modulus and (c) storage modulus evolution with temperature.....	56
Figure 2.6 Comparison of DMTA analysis for CP20 (a) and CP40 (b) oriented and unoriented samples.....	57
Figure 2.7 (a, b) Real part of the complex permittivity; (c, d) Imaginary part of the complex permittivity; (e, f) loss tangent of the unmodified copolymer (CP0) of the modified oriented and unoriented copolymers CP20 and CP40, respectively, for a frequency of 10 Hz.	58
Figure 2.8 $\tan \delta$ of the unmodified (COP0), modified oriented and unoriented copolymers CP20 (Top) and CP40 (Bottom), respectively, for a frequency of 10 Hz.	60
Figure 3.1 a) Chemical structure of: CP0 (unmodified PECH-co-EO), CP20 (PECH-co-EO modified with 20% Tap dendron), and CP40 (PECH-co-EO modified with 40% Tap dendron). b) Homeotropic alignment of the liquid-crystalline columns of the polymer to the membrane surface.....	71
Figure 3.2 Topographic 3-D images of CP20 unoriented (a) and oriented (b), of CP40 unoriented (c) and oriented (d). Scanned area: $5 \mu\text{m} \times 5 \mu\text{m}$	76
Figure 3.3 FESEM images of membrane cross-sections of: CP40 (a) and CP40 oriented (b).....	79
Figure 3.4 FESEM image of the scratched surface of CP40 oriented membrane. Left: membrane surface with scratched portion; Right: zoom of the scratched area.	80
Figure 3.5 Linear sweep voltammetry curve of CP40 and 0.1M NaCl as electrolyte (a) and example of curves for different monovalent cations for CP20 (b).	83
Figure 4.1 Chemical structure of Lupasol.....	93
Figure 4.2 Permeability system: 1) CO ₂ gas bottle, 2) valve, 3) pressure transducer, 4) manometer,5) steel module containing membrane, 6) gas flow meter.	96
Figure 4.3 The pores size distribution histograms of membranes: (a) L0; (b) L2; (c) L5; (d) L10; (e) L20.	99
Figure 4.4 ESEM micrographs of the cross-section of PSf-mG20 membranes: (a) L0; (b) L2; (c) L5; (d) L10; (e) L20.	100
Figure 4.5 Atomic Force Microscopy (AFM) topographic images of bottom side of PSf-mG20 membranes: (a) L0; (b) L2; (c) L5; (d) L10; (e) L20.	101
Figure 4.6 Raman spectra between 200 and 2500 cm^{-1} of: (a) mG20; (b) Top surface of L20; (c) L0. The arrow indicates the band at 1030 cm^{-1}	103
Figure 4.7 CO ₂ absorption flux into L0-L20 membranes as a function of liquid absorbent flow rate. (a) L20; (b) L10; (c) L0; (d) L2; (e) L5.....	104

Figure 4.8 ESEM micrographs with BSED of L2 membrane after 4 experiments in a flat sheet membrane contactor: (a) bottom surface; (b) cross-section; (c) X-ray analysis (EDX) analysis of the white spots seen in the micrographs.....	105
Figure 4.9 Mass transfer coefficient of L0-L20 membranes relative to: N ₂ (green bar); CO ₂ (red bar) ..	107
Figure 5.1 Chemical structure of Lupasol.....	116
Figure 5.2. Permeability system: (1) N ₂ or CO ₂ gas tank, (2) Valve, (3) Steel module containing membrane, (4) Digital gas pressure sensor, (5) Computer, (6) Membrane.....	119
Figure 5.3 Direct air capture system for CO ₂ absorption: (1) KOH solution tank, (2) Pump, (3) Module containing membrane, (4) Membrane.....	120
Figure 5.4 Environmental scanning electron microscope (ESEM) images of the cross-section of studied membranes: (a) M0; (b) M2; (c) M5; (d) M10.	123
Figure 5.5 Cumulative pore volume of M0-M10 membranes.	124
Figure 5.6 Pore volume distribution zoomed between 0 and 250 Å of: (a) M0; (b) M5; (c) M10.	125
Figure 5.7 Infrared spectra between 500 and 2000 cm ⁻¹ of: (a) M0; (b) M2; (c) M5; (d) M10. The band around 1660 cm ⁻¹ is highlighted.....	127
Figure 5.8 FTIR spectra between 1000 and 2000 cm ⁻¹ of (a) fresh M10, (b) M10 after soaking 24 hours in 0.64 M KOH and (c) neat UG20 additive.....	128
Figure 5.9 Stacked ¹ H NMR spectra (in dmf-d ₆ , 400 MHz) between 6.8 and 8.7 ppm of M10 samples: as-prepared (red trace), after treatment 24 hours in 0.64 M KOH solution and following washing (green trace) and after treatment in water (blue trace). Green- and yellow-shaded areas indicate the regions of additive and polysulfone signals, respectively.....	129
Figure 5.10 Loss factor (ε'') versus temperature at 1 Hz of frequency for M0, M2 and M10 membranes.	131
Figure 5.11 CO ₂ solubility in M0-M10 membranes determined by the pressure decay method at 2 bar.	132
Figure 5.12 Mass transfer coefficient k as calculated from CO ₂ (red bar) and N ₂ (green bar) permeation through M0-M10 membranes. In the inset the corresponding selectivities calculated as kCO ₂ /kN ₂ are shown.	133
Figure 5.13 CO ₂ absorption flux into M0–M10 membranes in direct air capture tests as a function of liquid absorbent (0.64 M KOH) flow rate: (a) M0; (b) M2; (c) M10; (d) M5.	134
Figure 5.14 (a) ESEM image of M10 bottom surface; (b) EDX analysis of bottom surface observed by ESEM; (c) XRD pattern of M10 bottom surface; the arrows evidence the crystalline peaks which overlap with the pattern of crystalline KHCO ₃	136

UNIVERSITAT ROVIRA I VIRGILI
NOVEL POLYMERIC MEMBRANES FOR ARTIFICIAL PHOTOSYNTHESIS
Alireza Zare

List of tables

Table 2.1 Reaction conditions and resulting modification degrees and yields for P(ECH-co-EO) modification with Tap.....	44
Table 2.2 Calorimetric characterization of CP0, CP20 and C40. Glass transition (T_g), melting (T_m) and clearing (T_{cl}) temperatures; melting (ΔH_m) and clearing (ΔH_{cl}) enthalpies per mol repetitive unit; crystallization degree (X_c). Data relative to unoriented samples determined from DSC second heating scan.	47
Table 2.3 Different thermal treatments and resulting peak width at half height (WHH) and angle of orientation of annealed membranes of the CP40 sample.	52
Table 3.1 RMS roughness and kurtosis from AFM images for CP20 and CP40 samples.	77
Table 3.2 Water Contact angle values of unmodified Poly(epichlorohydrin-co-ethylene oxide) (CP0), CP20 and CP40 membranes.	77
Table 3.3 Water uptake (%) after 72 hours, and methanol permeability after 168 hours, of unmodified Poly(epichlorohydrin-co-ethylene oxide) (CP0), CP20 and CP40 membranes.....	78
Table 3.4 Proton permeabilities of CP0, CP20, and CP40 in the presence of different cations in the stripping compartment.	81
Table 3.5 A summary of data obtained from LSV experiments.....	84
Table 4.1 Composition and morphological characteristics of the investigated membranes.....	98
Table 4.2 RMS roughness of bottom side, water contact angle (CA) and Water Uptake (WU) of PSf-mG20 membranes.	101
Table 5.1 Composition and morphological characteristics of studied membranes.	122
Table 5.2 RMS roughness of bottom side, water contact angle, Water uptake (WU) and KOH (0.64 M solution) uptake of the studied membranes.....	126
Table 5.3 Mechanical properties and glass transition temperatures of M0-M10 membranes.....	130

UNIVERSITAT ROVIRA I VIRGILI
NOVEL POLYMERIC MEMBRANES FOR ARTIFICIAL PHOTOSYNTHESIS
Alireza Zare

List of abbreviations

AAS	Amino acid salt
AFC	Alkaline fuel cells
AFM	Atomic force microscopy
APS	3-(aminopropyl)triethoxysilane
APS	Artificial photosynthetic system
CA	Carbonic anhydrase
CCS	Carbon capture and storage
CCU	Carbon capture utilization
CA	Contact angle
Col	Columnar
DEA	Diethanolamine
DETA	Dielectric thermal analysis
DMFC	Direct methanol fuel cell
DMTA	Dynamic-mechanical thermal analysis
DSC	Differential scanning calorimetry
EDX	Energy dispersive X-ray analysis
FAS	Fluoroalkylsilane
FESEM	Field emission scanning electron microscopy
GHG	Greenhouse
GLHFMC	Gas-liquid hollow fiber membrane contactors
IPCC	Climate change
LC	Liquid crystal
MCLCPs	Main-chain liquid-crystalline polymers
MEA	Monoethanolamine
MEA	Monoethanolamine
Mn	Number average molecular weight
MOFCs	Molten-oxide fuel cells

MOFs	Metal-organic frameworks
Mw	Weight average molecular weight
N	Nematic
NMR	Nuclear magnetic resonance
P(ECH-co-EO)	Poly(epichlorhydrin-co-ethylene oxide)
PAC	Perfluorinated acrylic copolymer
PAZE	Poly[2-(aziridine-1-yl-ethanol)]
PE	Polyethylene
PECH	Dendronized poly(epichlorohydrin)
PEM	Polymer electrolyte membrane
PEMFC	Proton-exchange membrane fuel cells
PES	Polyethersulfone
PMMA	Polymethylmethacrylate
PMs	Polymeric membranes
POM	Polarized optical microscopy
POM	Polarised optical microscopy
PP	Polypropylene
PSF	Polysulfone
PSF	Polysulfone
PTFE	Polytetrafluoroethylene
PVC	Poly(vinyl chloride)
PVDF	Polyvinylidene fluoride
SAFCs	Solid acid fuel cells
SCLCPs	Side-chain liquid-crystalline polymers
SCLPCs	Side-chain liquid-crystalline polymers
Sm	Smectic
SOFC	Phosphoric acid fuel cells
SOFCs	Solid oxide fuel cells

SPAES	Sulfonated poly(arylene ether sulfone)s
SPEEK	Sulfonated poly(ether ether ketone)
SPI	Sulfonated polyimide
SPOP	Poly(phosphazene)
SPPO	Sulfonated poly(phenylene oxide)s
SPS	Sulfonated poly(styrene)
Tap	Potassium 3,4,5-tris[4-(n-dodecan-1-yloxy)benzyloxy]benzoate
TBAB	Tetrabutylammonium bromide
TEA	Triethanolamine
TMV	Tobacco mosaic virus
WHH	Width at half height
XRD	X-ray diffraction
ZIFs	Zeolitic imidazolate frameworks

UNIVERSITAT ROVIRA I VIRGILI
NOVEL POLYMERIC MEMBRANES FOR ARTIFICIAL PHOTOSYNTHESIS
Alireza Zare

Structure of the thesis

This doctoral thesis focuses on the synthesis and preparation of ion conductive and CO₂ capture membranes. This doctoral thesis was organized as a compendium of publications. Its structure is shown in Figure 1:

- The first chapter consists of a general introduction and explanation of its objectives.
- Chapters 2 and 3 involve two publications regarding biomimetic ion conductive membranes. In these chapters, we focused on the synthesis and preparation of biomimetic membranes as ion conductive membranes. Biomimetic membranes are interesting artificial materials based on a biomimicking approach. These membranes show ion transport through a channel formed by the self-assembly process. In this way, in chapter 2, the chemical modification of a linear copolymer, (Poly (epichlorohydrin-co-ethylene oxide) (PECH-co-EO)), was performed with the potassium 3,4,5-tris[4-(n-dodecan-1-yloxy)benzyloxy]benzoate (Tap) with different degrees of modification. The modified copolymer can self-assemble into columnar structures, as already reported (*Polymer Engineering & Science 53, no. 1 (2013): 159-167*). In this structure, the inner part of the columns is formed by the main chain of the copolymer, and the side-chain dendrons form the outer part of the columns. Therefore, the electron donor atoms in the polymer main chain could facilitate the ion transfer through these conducting pathways provided by columnar structures. The modified copolymers were characterized by nuclear magnetic resonance (NMR), differential scanning calorimetry (DSC), X-ray diffraction (XRD), and optical microscopy (POM). Membranes were prepared by immersion precipitation method.
- Additionally, to achieve efficient transport properties, homeotropically oriented membranes were obtained by means of optimized thermal annealing treatment. The mobility of unmodified membrane and unoriented and oriented membranes was studied by dynamic mechanical, thermal analysis (DMTA), and dielectric thermal analysis (DETA). In chapter 3, membranes were studied by various techniques in terms of morphology, contact angle (CA), water uptake, methanol permeability, and transport properties. The modified copolymers were compared to the unmodified copolymer and Nafion 117. These ion conductive membranes are promising candidates for use in artificial photosynthesis systems.
- In chapters 4 and 5, polysulfone based membranes were employed as gas-liquid membrane contactors. We focused on improving CO₂ absorption performance by using two different types

of additives in neat polysulfone (PSf). These additives are amine additives based on hyperbranched Lupasol G20 partially grafted with benzoyl chloride (mG20 in chapter 4) or phenyl isocyanate (UG20 in chapter 5). Membranes with different amounts of additives were prepared by phase inversion precipitation. Membranes were characterized in terms of morphology, porosity, wettability, thermal and mechanical properties, CO₂ solubility permeability and absorption, especially solubility, hydrophobicity and chemical resistance to the aqueous alkaline absorbent solution. Generally, the addition of the additives considerably increased the performance of the membranes in terms of CO₂ capture with respect to neat PSf. These CO₂ capture membranes are an interesting candidate for gas-liquid membrane contactors in artificial photosynthesis systems.

- A closing chapter summarizes the general conclusions of the thesis.

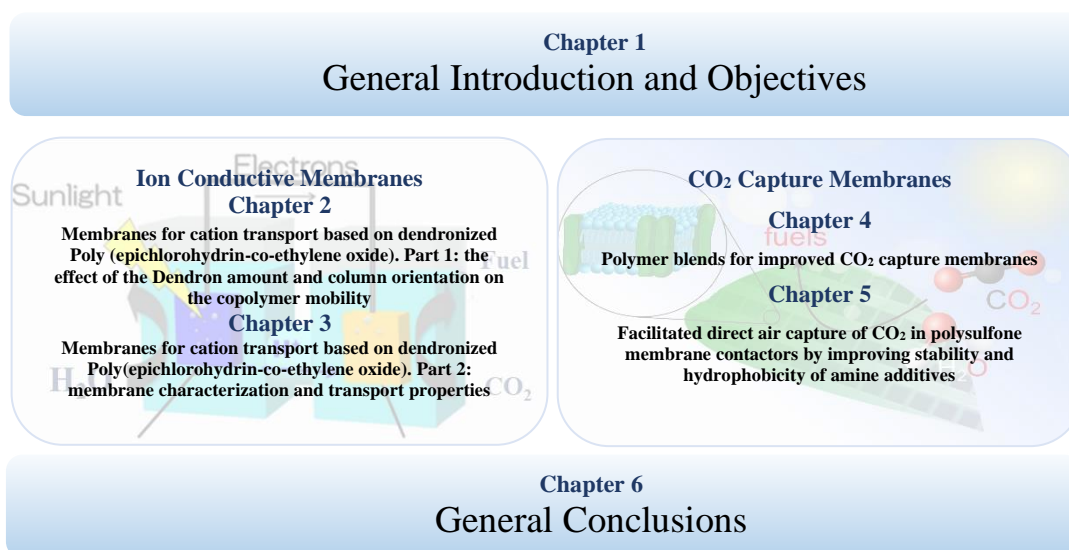


Figure 1 Structure of the thesis.



Chapter 1.

General Introduction and Objectives

UNIVERSITAT ROVIRA I VIRGILI
NOVEL POLYMERIC MEMBRANES FOR ARTIFICIAL PHOTOSYNTHESIS
Alireza Zare

1.1 Introduction

The exponential growth of the world population, which began in the second half of the eighteenth century, requires an increase in energy production. Since then, energy production has been mainly associated to the combustion of fossil fuels like carbon, petroleum, or natural gas, which are non-renewable and finite resources in nature, in addition to being correlated with the emission of polluting gases in the atmosphere that is detrimental to the health of our planet. In fact, the intensive use of fossil fuels contributes negatively to global warming [1-3].

During recent decades, it has been necessary to develop systems to produce clean or sustainable energy in order to guarantee the subsistence of the forthcoming generations as well as of our planet. This energy, called renewable or green energy, is obtained from inexhaustible natural sources: solar power, wind energy, geothermal energy, hydropower, tidal power, wave power, biomass, and biofuels (Figure 1.1) [4,5].

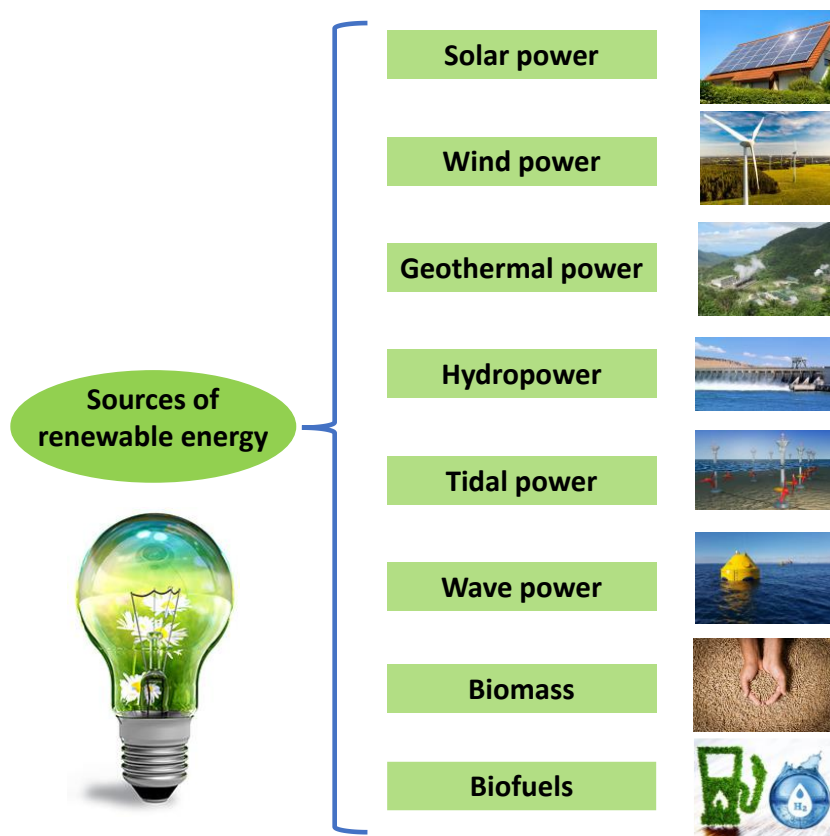


Figure 1.1 Natural sources for the obtention of renewable energy.

Moreover, the scientific community has made significant efforts to design and develop technological devices inspired by processes that occur spontaneously in nature, such as photosynthesis.

Thus, artificial photosynthesis is a system that mimics natural photosynthesis in green plants in which they efficiently convert water, carbon dioxide and sunlight into oxygen and simple organic compounds, which can be used as biofuels to power any energy device [6,7]. A similar energy system that is still under development are fuel cells, which take advantage of the chemical energy generated by mixing fuel and an oxidant to continuously convert it into electricity. Another benefit that encourages the development of these type of systems is the high energy efficiency that they exhibited ($> 90\%$) [8,9].

On the other hand, carbon dioxide (CO_2) is a by-product generated by the combustion of fossil fuels, wood, and other organic materials, as well as in industrial processes for obtaining ammonia, alcohols, and fertilizers [10,11]. It is well known that the accumulation of CO_2 in the atmosphere is associated to the greenhouse effect, which is closely related to global warming [12,13]. As published by the United States Environmental Protection Agency (EPA), CO_2 emissions represented around 80 % of the total amount of greenhouse gas emissions in the United States (2019) [14].

In this way, the reduction of the CO_2 concentration in the environment is a key requirement to avoid the negative consequences of climate change. Nowadays, there are different options to entrap atmospheric CO_2 (planting trees, forest management, good agricultural practices), being the capture and storing of carbon dioxide a highly attractive approach because the stored gas can then be used as a carbon source or as fuel in electrochemical devices such as fuel cells [15,16]. In this case, distinct separation technologies have been explored: absorption, adsorption, chemical looping, membrane gas separation, or gas hydration [17-20]. From all of them, in this chapter, we will focus on the membrane gas separation technologies used for CO_2 capture.

Besides, the membranes used in artificial photosynthesis and fuel cell devices are one aspect in which scientists try to address their efforts to improve it because membranes play an important role in all these devices [21,22]. Another aspect in common that these membrane-based technologies present is that the used membranes are commonly synthetic polymeric membranes [23], even though the number of research groups that center their investigations on the design and development of biomimetic membranes is increasing [24-26].

Figure 1.2 evidenced the increasing interest of “membranes in energy systems”, since it is observed that the number of peer-reviewed publications related to this topic has been increasing decade after decade. This growing interest is associated with the improvements observed in the field of energy systems, which provided promising results in addition to being “greener systems” [23,27].

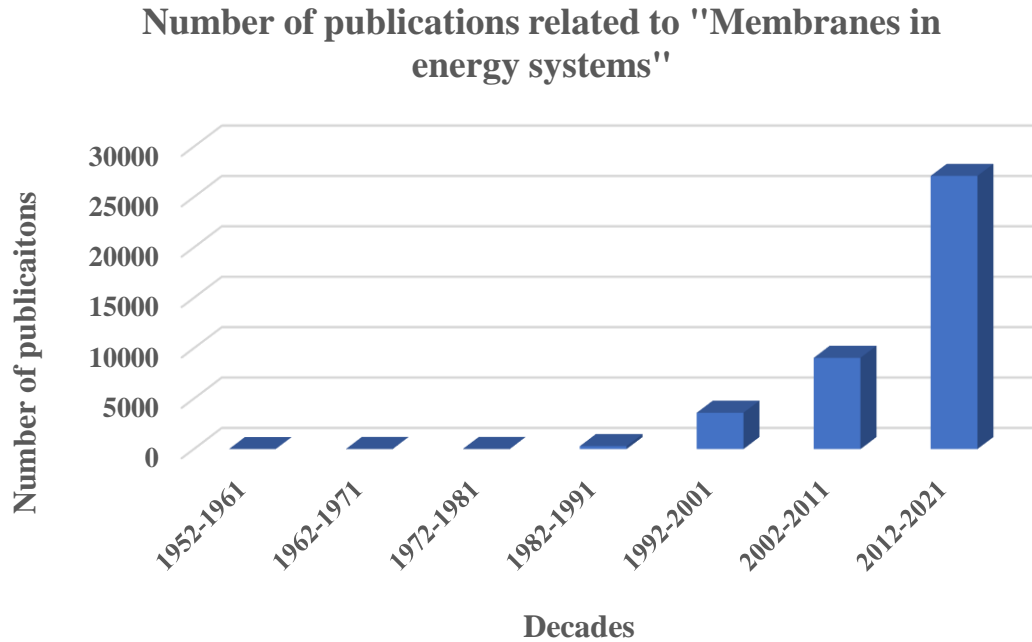


Figure 1.2 Number of peer-reviewed scientific articles published by decades since 1932 in the field of “membranes in energy systems” (Source: Web of Science).

Therefore, this chapter presents a detailed description of the different options that distinct materials offer in the construction of improved membranes that could be used in ion-transport devices, considering the possible transport pathways across the membranes. Furthermore, previous studies based on the biomimetic approach to design advanced membranes are presented, taking advantage of the flexible structure of liquid crystalline polymers. Afterwards, the second part of this chapter exposes an overview of the recent research that was carried out with membrane-based systems employed in carbon dioxide capture.

1.2 Membranes for energy production and storage

1.2.1 Artificial photosynthesis and fuel cells: an overview

Since Sir William Grove reported the invention of the first fuel cells in 1838, it was observed that these energy generation systems are much cleaner than traditional power generation because fuel cells use renewable energy sources as raw materials, showed a high flexibility in installation and operation, are silent, efficient and they exhibited low emissions of pollutants and toxic by-products. As of the year 1932, which was precisely when Francis Thomas Bacon brought out the first fuel cells for sale, some types of fuel cells have been developed and they are currently being used in various applications such

as power supply for fuel cell vehicles (automobiles, motorcycles, buses, boats, etc.) or to provide energy power for commercial, industrial and residential buildings among others.

When classifying fuel cells, different criteria can be considered (the type of electrolyte, the difference in startup time, the working temperature, etc.). According to the type of electrolyte they use, the following types of fuel cells can be found [28]:

- Proton-exchange membrane fuel cells (PEMFC), among which are direct methanol fuel cells (DMFC).
- Alkaline fuel cells (AFC).
- Phosphoric acid fuel cells (SOFC).
- Solid acid fuel cells (SAFCs).
- Solid oxide fuel cells (SOFCs).
- Molten-oxide fuel cells (MOFCs).

Even so, all of them work following the same general methodology because they are constituted by the same two compartments: an anode and a cathode. The third component, the electrolyte, is located between both compartments, as shown in the scheme of a Direct Methanol Fuel cell depicted in Figure 1.3.

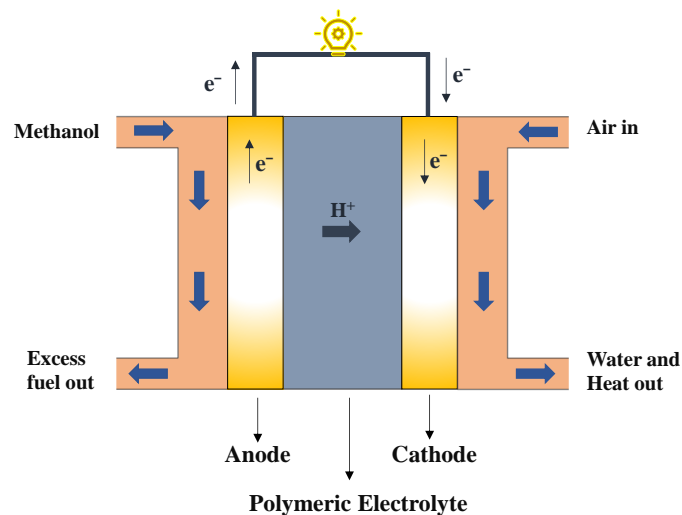
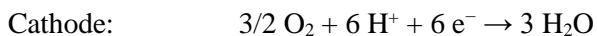


Figure 1.3 Schematic representation of a Direct Methanol Fuel Cell (DMFC).

Once a fuel is supplied (liquid methanol in the case of Direct Methanol Fuel cells), the fuel cell is working since two chemical reactions take place, one at each electrode:



As observed in the anode reaction, when methanol is mixed with water, it is split into protons and free electrons apart from generating carbon dioxide. The generated protons move to the cathode crossing the polymer electrolyte membrane (PEM), where they react with an oxidant (oxygen or air) to form water. At the same time, the electrons flow from anode to cathode produces an electric current that can be used to power electrical devices. Therefore, PEM is an essential component for transporting protons across the membrane in DMFC, since on the one hand it keeps apart both compartments (anode from cathode), but it also provides a selective pathway to transport protons from anode to cathode.

Since they began to be used during the 1960s, several types of polymer electrolyte membranes have been developed since 1960s, being polymers with sulfonated groups (sulfonated poly(ether ether ketone) (SPEEK), sulfonated poly(phenylene oxide)s (SPPO), sulfonated poly(arylene ether sulfone)s (SPAES), sulfonated poly(styrene) (SPS), sulfonated polyimide (SPI) and poly(phosphazene) (SPOP)) the first type of systems employed as polymer membranes in these electrochemical devices due to their low production cost, their exceptional thermal stability and mechanical properties combined with a low fuel crossover [29]. Nevertheless, the low molecular strength exhibited by partially and completely sulfonated polymers at higher temperatures than 100 °C limits their application as PEM [30].

Another type of polymers that gained a lot of interest during the 1960s in the preparation of membrane separators were sulfonated fluoropolymers, which are synthetic polymers encompassed in the well-known brand Nafion® (produced by a Dupont spin-off: Chemours). The chemical structure of Nafion is depicted in Figure 1.4. Nowadays, PEM membranes based on Nafion® polymers are still the most used membranes in fuel cells, which is due to the high proton conductivity and the good mechanical properties of perfluorinated sulfonic acid membranes. However, Nafion® membranes depend highly on water content, and neither can be applied at high temperatures (> 80 °C) because of dehydration. In addition to low efficiency at high temperatures due to water evaporation, Nafion® membranes present some important drawbacks that limit their applications: they exhibit low stability in water from a structural point of view because they swell easily, which can induce fuel crossover across Nafion® membranes. Furthermore, the production cost of fluorinated polymers is high and the recycling of Nafion® membranes at the end of their life cycle is a very complex process [31-34].

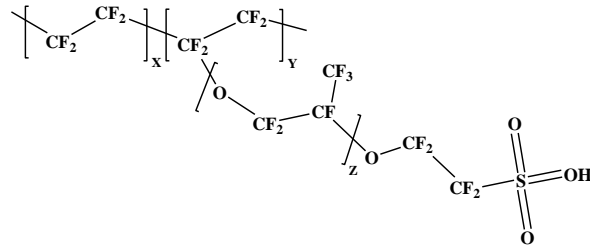


Figure 1.4 Chemical structure of Nafion.

Therefore, understanding the transport mechanisms through hydrated Nafion® membranes can help scientists comprehend the low selectivity of these types of membranes and will provide useful insights into the design and preparation of membranes for proton transport with better performance [6,35]. In point of fact, proton transport in Nafion® occurs by two main mechanisms (Figure 1.5):

- Grotthus mechanism: In this mechanism, proton transport happens by hopping from one hydrolyzed group to another one due to the formation and breaking of hydrogen bonds between the ionic groups (SO_3^-) present in the membrane chemical structure and moving protons.
- Vehicular mechanism: In this case, protons are bound to water molecules ($H^+(H_2O)_x$); which are involved in proton transport across the polymeric membrane. To favor this mechanism, high hydration degrees are required inside the fuel cell.

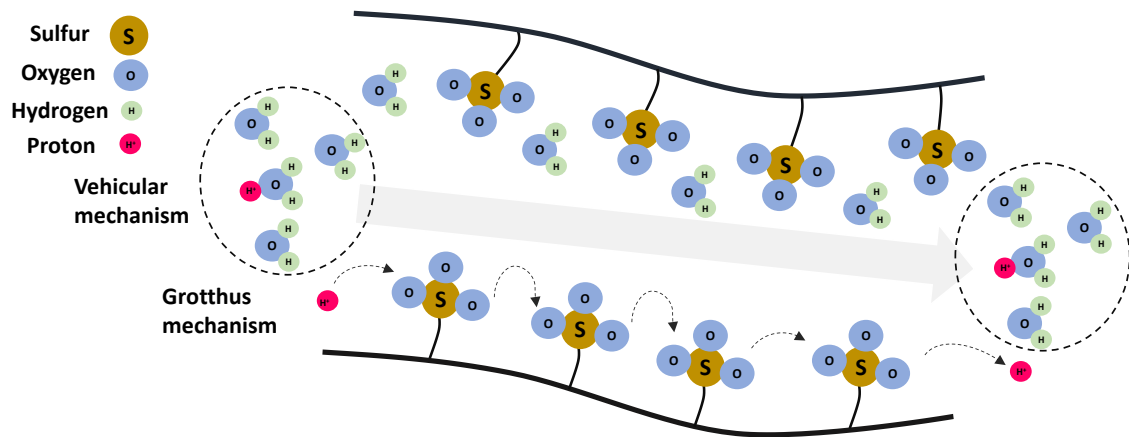


Figure 1.5 Representation of the proton transport mechanism in PEM: a) Grotthus mechanism; b) Vehicular mechanism.

So, the amount of water in contact with the electrolyte directly affects proton conductivity, in turn limiting PEM efficiency since high hydration degrees causes swelling and decreases mechanical properties and fuel crossover, while reducing the degree of hydration leads to poor membrane function. These crucial

requirements offer a necessary demand for further investigation to address some functional limitations in proton exchange membrane and fuel cell conditions to produce clean energy [6,35].

To minimize the inconveniences of perfluorinated membranes, other possibilities have been explored, including the preparation of hybrid membranes, polymeric blends, composites, the doping of polybenzimidazoles with phosphoric acid, etc. Even so, none of these alternatives has made it possible to overcome all the aforementioned drawbacks.

Therefore, the development of polymers that present a 3D structure that allow efficient proton transport regardless of the amount of water should be an interesting choice [36,37].

1.2.2 Biomimetic ion transport: from biological systems to supramolecular self-assembled structures

Nature has been an inexhaustible source of concepts, ideas, and resources over the years. Nowadays, several nature-inspired products that facilitate our daily tasks have been designed by the scientific community and are available in the market (as an example, biopolymers like starch or PLA are used in packaging while chitosan and bioceramics are playing important roles in medical applications) [38-41].

Considering that ion and water transport processes between cells are vital in biological systems, membranes and membrane processes have emerged in nature since life exists [42]. For instance, most biochemical reactions are sensitive to pH changes, and proton transfer plays a pivotal role in stabilizing cell pH and following biological activities [43]. The high selectivity and efficiency of proton transport in natural systems, even without the presence of water, has aroused a great interest in the scientific community [44].

In general, transport occurs mainly through two mechanisms in biological systems, which are carriers and channels. Both mechanisms allow the passage of water, ion, sugars, amino acids, and anything necessary to complete metabolism in cells. Carriers are usually proteins that connect to a molecule or an ion in one side of the membrane, from which they separate after crossing the membrane. On the other hand, channels create hydrophilic holes in the membranes, through which the target molecules or ions move past only in favor of the concentration gradient. Both transport mechanisms are illustrated in Figure 1.6.

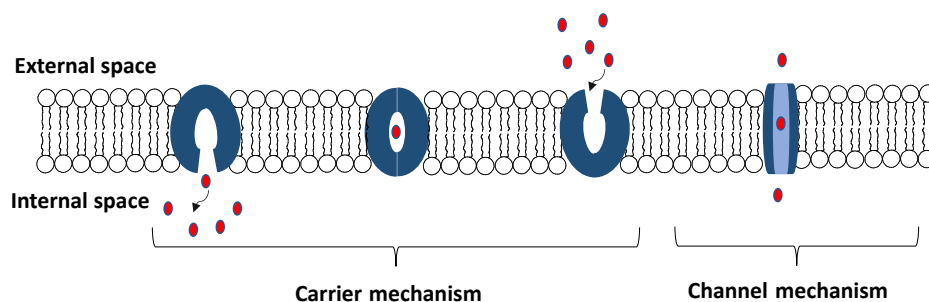


Figure 1.6 Types of natural transport across cell membranes: a) Carrier and b) Channel.

From these two types of mechanism, ion channels are the most common type of ion transport in biological cells. In this way, most of the research in proton transport have been focused on the design and development of artificial supramolecular assemblies capable of transporting ions across synthetic membranes trying to mimic ion transport as it takes place in natural ion channels.

In 1987, Dulyea and coworkers reported the first attempt to build synthetic membranes that mimic the ionic transport exhibited by ion-channels. The prepared membranes are constituted by crown ether carboxylic acids bonded to a polyamide backbone. Inside the membrane structure, the ions hop between the crown ethers, which are packed forming cylinders, *via* the Grotthus mechanism [45]. Following the same idea, Voyer *et al.* linked crown ethers to natural peptides as depicted in Figure 1.7 [46-48].

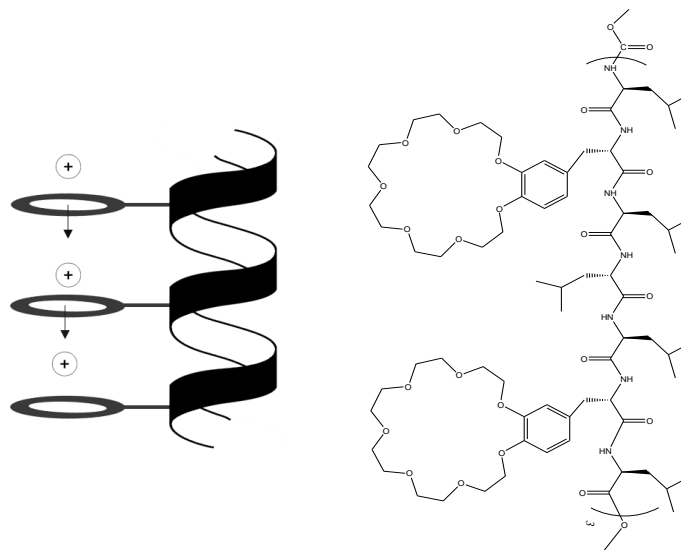


Figure 1.7 Ion channels by cylindrical packing of crown ether rings [48].

However, this molecular structure results in an unfavorable energy barrier and a discontinuous transport mechanism due to the high attraction of a cation within one crown ether unit inside the cylinder structure and the great energy barrier for a proton jump to the next crown ether molecule. Therefore, some

research was conducted to eliminate this energy barrier in the resulting cylindrical structure. In this regard, Koert and coworkers designed for the first time a polyether-based structure that would transport Na^+ and K^+ ions across a tunnel geometry system constituted by tetrahydrofuran oligomers [49].

Nonetheless, the large number and complex steps involved in the synthesis of these oligo(tetrahydrofuran)s led to the consideration of alternative routes for the development of artificial ion channels. Since that time, the vast majority of efforts have been devoted to the design of supramolecular polymers, which main chain can self-assembly into columnar structures. Supramolecular chemistry refers to the chemistry of complex entities generated through intermolecular and/or intramolecular noncovalent interactions (hydrogen bonding, Van der Waals forces, electrostatic interactions, hydrophobic interactions, etc.). Some examples observed in natural systems demonstrate that the self-assembly strategy can be applied to force polymer chains, which initially present a random coil conformation, to adopt a helical conformation via self-assembly as observed in nature in the case of Tobacco Mosaic Virus (TMV) [50]. TMV structure is constituted by 2130 tapered shape proteins and a ribonucleic acid (RNA) chain, which after interacting with each other self-assembly into a cylindrical structure that compel the RNA of the virus to self-organize into a helical conformation in the inner part of the structure (Figure 1.8). The similar shape and large contact area of the tapered proteins promote the exo-recognition between them around the RNA chain by intermolecular forces.

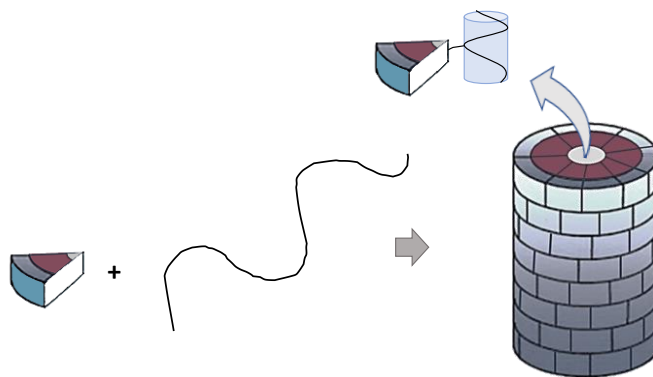


Figure 1.8 Schematic representation of the self-assembly process of TMV.

In the same manner, a cylindrical supramolecular structure could be reached by joining tapered shape moieties to a polymer chain. Thus, polymers that self-assembly into columnar structures, like columnar liquid-crystalline polymers, can be a promising approach to synthesize biomimetic ion channels.

1.2.3 Liquid-crystalline polymers

All the materials in the universe can be present in different forms, that are also known as states of matter aggregation. In each state of matter, atoms or molecules are aggregated in distinct ways, which

confers characteristic properties to each state. There are several states of matter, being the solid, liquid and gas the most typically observable. Even so, some materials present the ability to arrange in other types of states of matter. One clear example is the liquid crystalline state or liquid crystal (LC) mesophase, in which molecules can partially flow like liquids, in addition to exhibiting a long-range orientational order (Figure 1.9). This intermediate behavior showed by liquid-crystal mesophases may provide exceptional attributes that can be very useful in optical or technological applications.

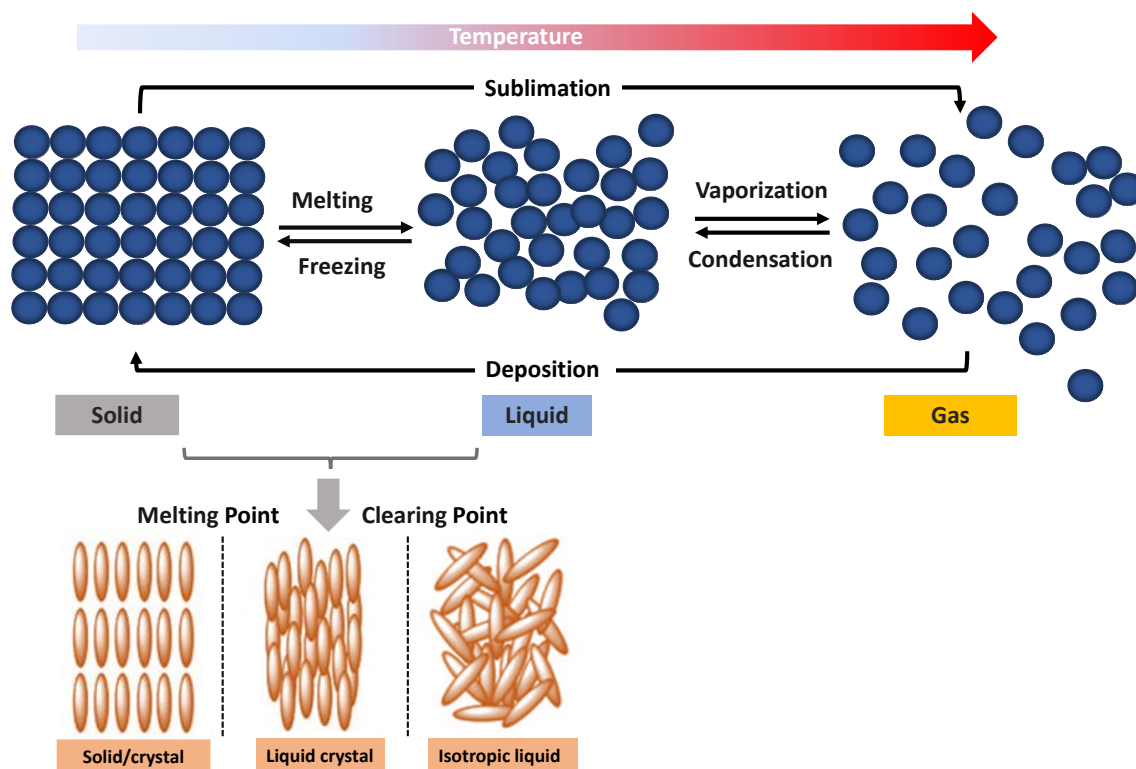


Figure 1.9 Schematic illustration of the molecular arrangement in different states of matter.

The molecules of a compound that can form a LC mesophase are called mesogens, whose main characteristic is its high anisotropy with respect to its shape. As a matter of fact, mesogens can be classified according to their shape into calamitic (rod-shape or discotic (disk-like shaped liquid crystals (Figure 1.10).

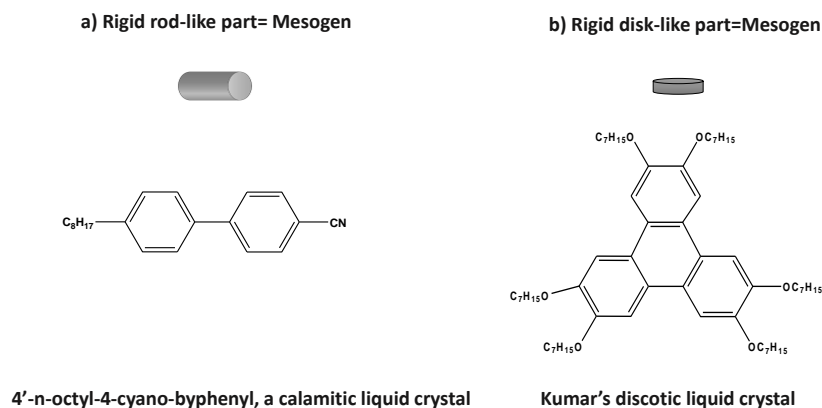


Figure 1.10 Types of LC mesogens as stated by their shape: a) Calamitic mesogens and b) Discotic mesogens.

Another classification separate liquid-crystals in thermotropic liquid-crystals and lyotropic liquid-crystals depending on whether its LC mesophase depends on the temperature or it is induced by adding a certain solvent, respectively. Moreover, three types of thermotropic liquid-crystalline mesophases can be differentiated according to the degree of order of the mesogens (Figure 1.11):

- Nematic (N) mesophases: The longitudinal axis of the mesogens is aligned in the same direction, showing a long-range directional orientation.
- Smectic (Sm) mesophases: In this type of mesophases, mesogens add positional order along one direction to the directional orientation exhibited by N mesophases. Therefore, mesogens are organized in well-defined layers that can slide over one another.
- Columnar (Col) mesophases: In this case, mesogens are packed in cylindrical structures.

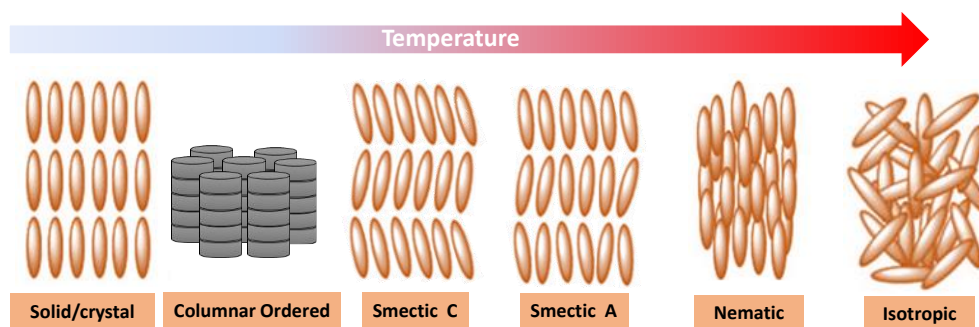


Figure 1.11 Organization of molecules in different thermotropic LC mesophases.

Mesogens can be inserted or bonded to polymer chains to form liquid-crystalline polymers (LCPs), which are very attractive materials because they combine the properties of polymers with the properties of

LCs. As observed in Figure 1.12, two types of LCPs can be found according to the relative position of the mesogens in the polymer structure:

- Main-chain liquid-crystalline polymers (MCLCPs): Mesogens are part of the polymer main chain. They are connected by flexible spacers.
- Side-chain liquid-crystalline polymers (SCLCPs): Mesogens are linked to the polymer main chain as pendant groups.

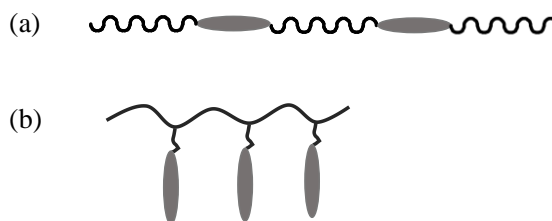


Figure 1.12 Representation of the structure of: a) MCLCPs and b) SCLCPs.

The molecular organization of LCPs can be influenced by different factors such as the nature of the mesogen, polymer molecular weight, chemical structure, and length of the spacer, etc. Thus, various LC mesophases can be formed.

1.2.4 Supramolecular self-assembly of side-chain liquid-crystalline polymers (SCLCPs)

The synthesis of SCLCPs that contains tapered mesogenic groups as side groups could lead to columnar structures. Apart from inducing the self-assembly process of the SCLCPs, the side-chain mesogens are expected to protect the polymeric main chain in the exo-recognition process between the dendrons. The resulting polymer chain, which adopts a helical structure, can act as an ion-channel owing to the presence of electronegative atoms that interact with the transported cations.

At the end of the last century, Percec and coworkers reported for the first time the self-assembly of dendronized LCPs into columnar structures (Figure 1.13) [51]. Since that time, Percec *et al.* have focused on the study of the self-assembly process of different supramolecular dendrons, dendrimers and dendronized polymers [52,53]. Concurrently, the interest in applying this synthetic route in the development of ion-conductive networks has been increasing.

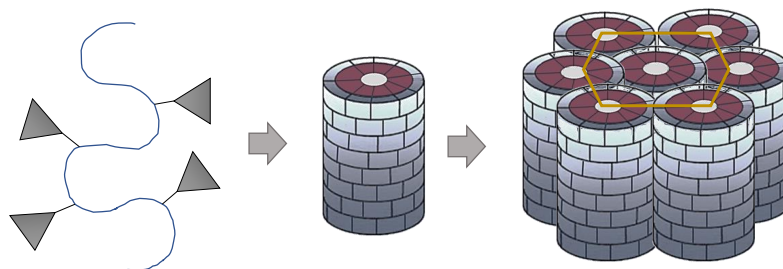


Figure 1.13 Schematic representation of the self-assembly of SCLCPs into a hexagonal columnar structure.

A similar work on this topic was conducted by Tylkowski et al. [54]. In their research, the authors described the synthesis of dendronized poly(epichlorohydrin) (PECH) with the dendron 3,4,5-tris[*p*-(*n*-dodecan-1-yloxy)benzyloxy]benzoate (Tap) by chemical modification to construct ionic channels that allow proton transport. Other polyamines and polyethers were modified with the same dendron to synthesize SCLCPs that self-assemble into columnar structures: poly(epichlorohydrin-co-ethylene oxide) [P(ECH-co-EO)] [44], linear polyglycidol (LPG) [55], poly[2-(aziridine-1-yl-ethanol)] (PAZE) [56]. The chemical structure of dendronized P(ECH-co-EO), PECH, and PAZE is shown in Figure 1.14. Based on the amount of Tap grafted to the polymer backbone, distinct columnar mesophases were obtained.

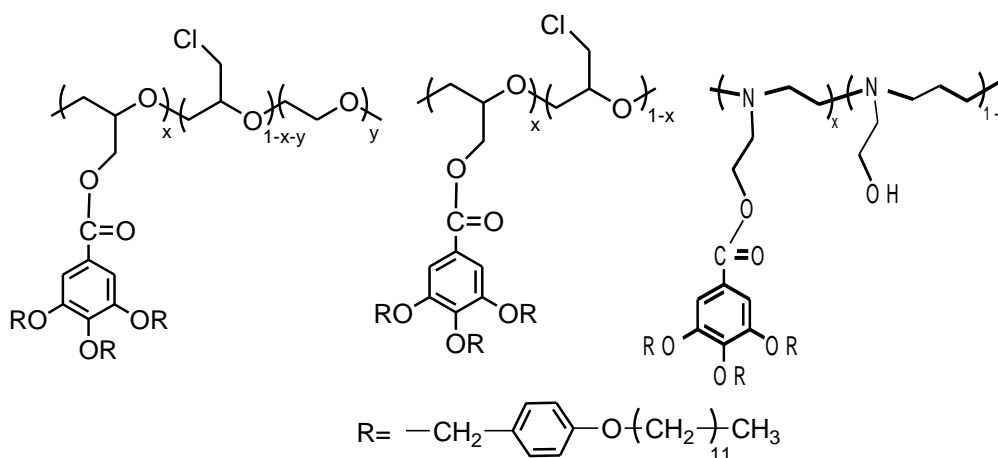


Figure 1.14 Chemical structure of modified polymers with Tap mesogenic group: a) [P(ECH-co-EO)], b) PECH and c) PAZE [44,56,57].

Even so, it is expected that the induction of a homeotropic orientation of the polymer channels is crucial for transport processes to achieve promising biomimetic polymer membranes that can be applied as PEM in environmentally friendly devices, such as fuel cells and artificial photosynthesis. By way of proof, Yoshio *et al.* proved the importance of inducing a macroscopic alignment of these nanostructures to enhance the ion-conductive properties of these materials. Actually, Yoshio and coworkers could

homeotropically align 1D columnar liquid crystals of a fan-shaped imidazolium salt containing acrylate groups at the periphery of the dendron to a chemically modified glass and indium tin oxide surfaces with 3-(aminopropyl)triethoxysilane (APS). On the other hand, parallel orientation of the polymeric columns was accomplished employing a simple mechanical shearing [58]. Comparing the ionic conductivity of the two oriented systems, the one with the columns oriented perpendicular to the surface shows a higher conductivity than the film in which the columns were oriented parallel to the surface.

According to that, Bartosz *et al.* prepared oriented membranes with dendronized PECH by sandwiching a polymer solution between two hydrophilic layers (water and glass) to finally obtain homogeneous films. Once tested in transport experiments, the oriented membranes presented a proton permeability similar to Nafion® N117, while protons did not pass through the non-oriented membranes. With the aim of optimizing the homeotropic orientation of the membranes, Bogdanowicz *et al.* reported a reproducible thermal treatment based on an annealing process to favor the homeotropic orientation of the

LC columnar mesophases (Figure 1.15) [59]. Specifically, unoriented membranes were heated above the clearing temperature of the SCLCPs, followed by a slow cooling that comprises three steps:

- 1st stage: Slow cooling to a temperature slightly below the clearing temperature of the SCLCPs.
- 2nd stage: Annealing or isothermal step at a temperature slightly below the clearing temperature of the SCLCPs.
- 3rd stage: Slow cooling to room temperature.

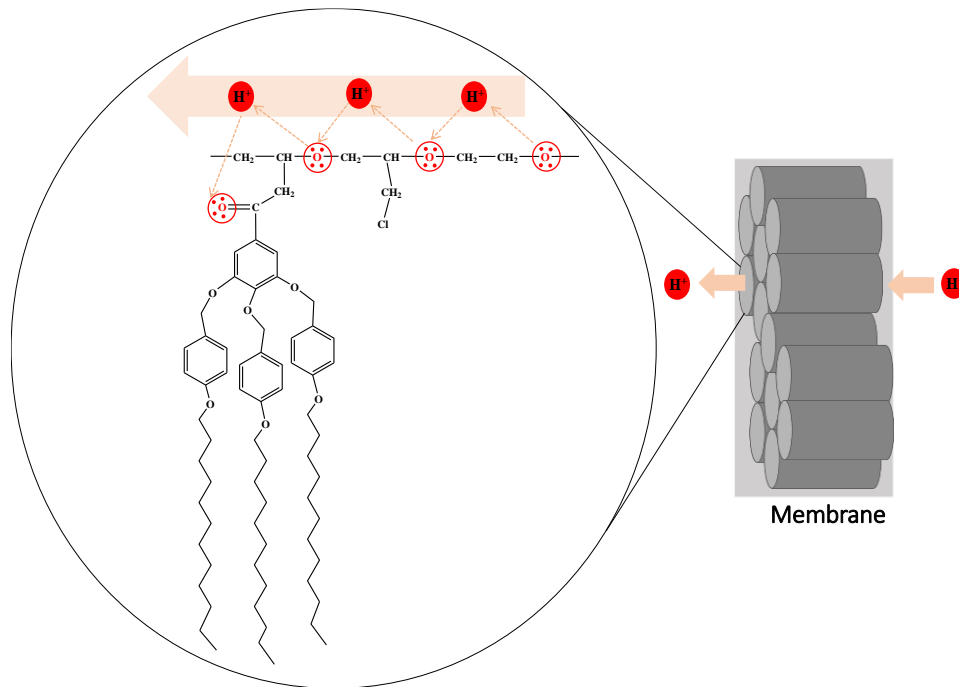


Figure 1.15 Schematic of ion transportation in biomimetic membranes [59].

The thermal procedure was used in the preparation of oriented membranes made of dendronized polyethers and polyamines, obtaining in all cases a perpendicular orientation of the SCLCPs columns to the surface of the membranes. The homeotropically oriented membranes exhibited an improved ion transport in addition to showing no water uptake and a low methanol crossover [55,57,60].

1.3 Membranes for CO₂ capture

Carbon capture and storage (CCS) technologies are a set of processes that allow the capture of carbon dioxide (CO₂), its fixing or storage. During the last years, CCS technologies have gained a lot of interest because CO₂ is the main greenhouse gas, and its emissions are highly linked to human activities

(burning of fossil fuels, vehicles, industry, etc.). Therefore, the main goal of CCS is to prevent CO₂ from damaging the Earth's atmosphere [61].

During this time, several separation technologies have been developed for carbon capture: membrane technologies, oxyfuel combustion, absorption, adsorption, chemical looping combustion, calcium looping or cryogenic [62]. From all of them, it seems that gas absorption into a chemical solvent containing an amine (such as diethanolamine, methanolamine, ethanolamine, diisopropanolamine among others) is the most efficient way to remove CO₂ from a gas stream [63]. After that, CO₂ is separated from the liquid solution at high temperatures. However, this process requires high energy demands since a large active area is needed to achieve an optimal absorption of CO₂ into the solvent (columns or towers of absorbent), which increases the cost of the CO₂ capture process.

Thus, researchers try to develop other mechanisms to overcome these limitations and at the same time improving the entrapment of CO₂. Besides, CO₂ can be used as starting material in the synthesis of chemical compounds or as a source of fuel or energy production in DMFC once isolated (Carbon capture utilization (CCU)). In this sense, the development of membrane contactors is an attractive option for CO₂ capture (gas-liquid membrane contactors) due to its low cost and high versatility. So, the following section present the role of gas-liquid membrane contactors in CO₂ capture processes and their optimal properties.

1.3.1 Membrane contactors in CO₂ capture

A membrane contactor is a device that allows the transfer of mass and/or heat between two phases that are in contact through the membrane contactor. Membrane contactors used in CO₂ capture are gas-liquid membrane contactors (Figure 1.16). In contrast to absorbent columns, membrane contactors present a flexible design, are moldable and cheaper [64]. As an example, Yeon and coworkers showed that a membrane contactor system consumes less energy than packed columns to achieve the same CO₂ absorption efficiency [65]. Additionally, membrane contactors have the advantage of independently controlling the liquid-phase and gas-phase and prevent the frequent operational problems of traditional absorbers such as flooding, entrainment, foaming, and channeling.

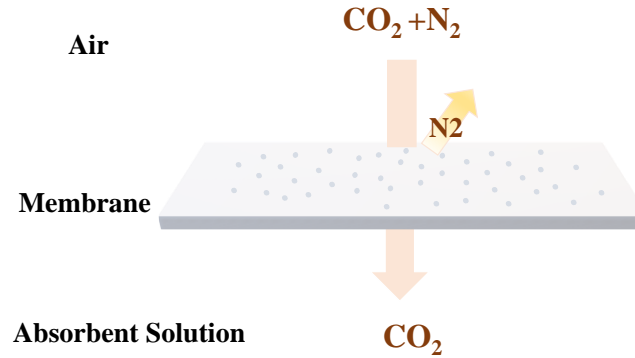


Figure 1.16 Example of a gas-liquid membrane contactor for CO₂ capture.

Furthermore, the desired properties of an ideal membrane contactor are:

- Great gas-liquid contact area.
- Small size and weight.
- Simple production.
- High selectivity for CO₂ transfer through concentration gradient rather than a pressure gradient.

In the development of a membrane contactor with a high efficiency, the selection of a membrane and the appropriate absorbent is vital. Polymeric membranes present a good thermal stability, chemical stability and mechanical strength. Moreover, membranes should have high gas permeability, be compatible with module design characteristics and solvent as well as be inexpensive [63].

Another important point to consider is the wetting of the membrane, which significantly reduce the CO₂ capture performance of gas-liquid membrane contactors [66,67]. In principle, membrane porous and open structures are advantageous for CO₂ absorption, although they contribute to membrane wetting, reducing membrane performance. This drawback can be reduced by designing hydrophobic membranes by surface modification such as Lim *et al.* have reported for the obtention of highly hydrophobic polymer membranes to prevent membrane wetting [68].

On the other hand, CO₂ is transported from the gas phase to the liquid phase by diffusion in gas-liquid membrane contactors. The CO₂ transfer can be divided into three steps:

- 1) Diffusion of CO₂ from the bulk gas-phase to the membrane.
- 2) Transport of CO₂ through the mesoporous membrane pores to the membrane-liquid interface.
- 3) CO₂ transfer from the membrane-liquid interface to the bulk liquid-phase, where liquid-phase is selective for CO₂ absorption.

The only driving force for CO₂ diffusion through the membrane is the carbon dioxide gradient concentration in gas phases and liquid phases.

1.3.2 Membranes for CO₂ capture

The most frequent classification of membrane materials employed in CO₂ separation is according to the material that constitutes it. According to that, 3 types of membranes can be differentiated:

- Ceramic membranes (CMs).
- Polymeric membranes (PMs).
- Biocomposite membranes (BMs).

In this section, some recent examples in literature of the application of each type of membranes in the field of CO₂ capture and separation are discussed. Furthermore, the advantages and drawbacks of each type of material used as membrane are remarked.

• Ceramic membranes

Ceramic membranes are membranes formed by inorganic materials like alumina (Al₂O₃), silica (SiO₂), zirconia (ZrO₂), titania (TiO₂) or other ceramic materials. Although they are more expensive than polymer membranes, ceramic membranes exhibit an excellent thermal and chemical stability. Thus, they can be used in aggressive media or at high temperatures [69]. Among the different types of ceramic membranes, ceramic hollow fiber membranes have been extensively investigated.

However, the most common issue of ceramic membranes is their hydrophilicity due to the presence of hydroxyl groups on their surface. During the last decade, many investigations were conducted to modify the surface hydrophobicity of ceramic membranes, being the surface treatment of the ceramic material by fluoroalkylsilane (FAS) coupling the most widely used approach [70]. As depicted in Figure 1.17, FAS reacts with hydroxyl groups of the ceramic materials without significantly affecting its thermal properties [70,71].

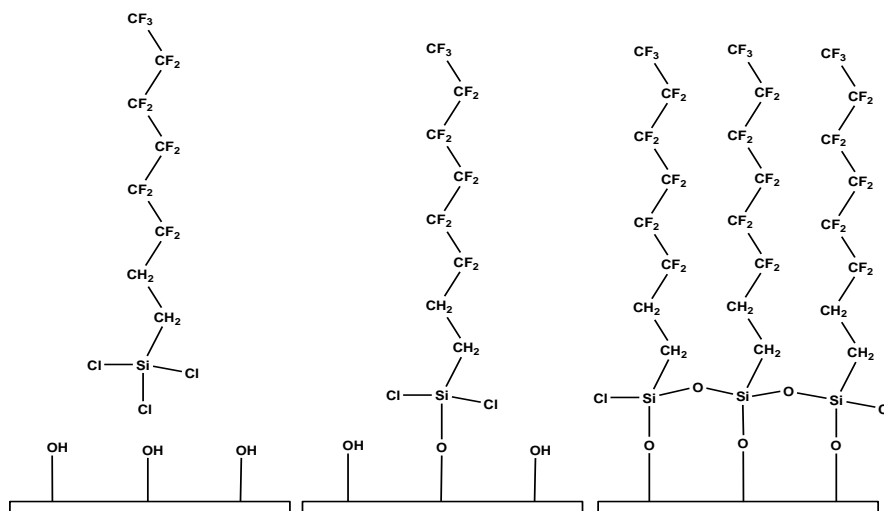


Figure 1.17 Representation of the surface modification of a ceramic material with FAS.

For example, Magnone *et al.* reported the direct modification of alumina hollow-fiber membrane contactor with a high-symmetric distribution of morphological elements. The modified membrane disclosed a higher CO₂ absorption flux at room temperature with a single-symmetric ceramic membrane compared to other conventional polymeric membranes for CO₂ absorption into monoethanolamine (MEA) solutions [72]. Moreover, Abdulmunen *et al.* suggested a low-cost and high-performance superhydrophobic kaolin-alumina hollow fiber membrane prepared via phase inversion-based extrusion and sintering techniques from a suspension of kaolin and alumina mixture and subsequently grafting with fluoroalkylsilane (FAS). After surface modification, the membrane contact angle was increased to 142° to improve the wettability resistance of the membrane. The grafted kaolin-alumina hollow fiber membrane seems appropriate for developing a high-performance gas-liquid membrane contactor system for CO₂ capture [73]. Lin *et al.* performed the coating of mesoporous silica aerogels on macroporous Al₂O₃ tubular membranes for shrinking the pore size for CO₂ absorption in membrane contactors. Then, membranes were modified with FAS. After four modifications with FAS, the value of surface contact angle reached 139°, showing membranes with high hydrophobicity. They are appropriate for CO₂ absorption as membrane contactors with suitable durability [71]. Yu *et al.* prepared a superhydrophobic ceramic (SC) membrane contactor from an alumina tube with a ZrO₂ layer through grafting with fluoroalkylsilane (FAS) in a triethoxy-1H,1H,2H,2H-tridecafluoro-n-octylsilane solution. The fabricated membrane contactor exhibited great potential in actual industrial CO₂ post-combustion capture due to its good anti-wetting and anti-fouling structures [74]. In another recent study, Hameed Saud *et al.* presented a membrane contactor that has a superhydrophobic surface where kaolin clay was modified by three types of fluoroalkylsilane (FAS) molecules (C6, C8, C10) to capture CO₂ from natural gas via contacting the gas-liquid system. C8 was

unveiled as the best type of FAS for separating CO₂ based on liquid entry pressure of water (LEP_w) and contact angle [75].

- **Polymeric membranes**

The second main group of materials that are widely investigated as membrane materials that can be used to capture CO₂ are polymers since several non-expensive methods to prepare membranes using polymers have been developed, like phase inversion, thermal processes such as melt extrusion or by mechanical stretching [68]. Moreover, the excellent properties of polymeric materials (among which stand out its high versatility, its hydrophobicity, its porosity, and its excellent mechanical properties) clearly encourage the scientific community to commit to the development of novel polymeric membranes for CO₂ capture. The chemical structure of some polymers that have been studied in the preparation of membrane contactors is shown in Figure 1.18, including polyethylene (PE) [63], polypropylene (PP), polytetrafluoroethylene (PTFE), polyvinylidene fluoride (PVDF), Nylon, polysulfone (PSF), polyethersulfone (PES), poly(vinyl chloride) (PVC) [76] and fluorinated polymers (for example Hyflon® AD 60).

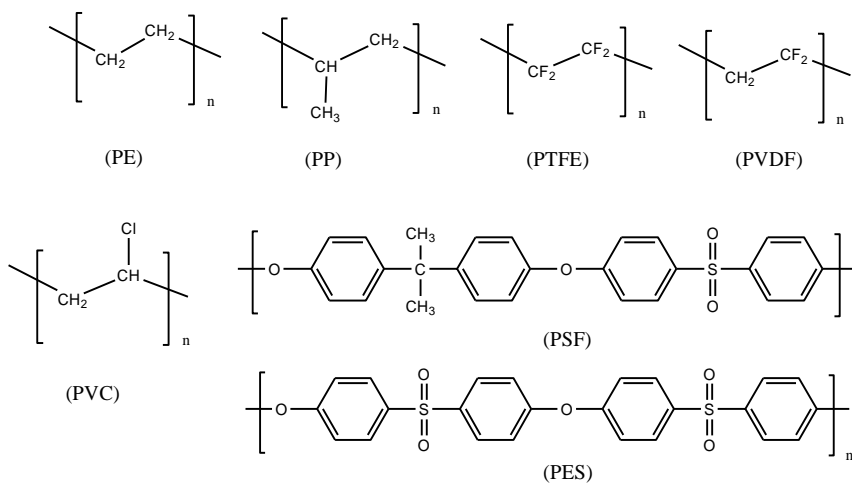


Figure 1.18 Chemical structure of common polymers employed as membrane contactors.

The properties of the resulting polymeric membranes are highly influenced by various factors, being the most important ones the intrinsic polymer properties and the fabrication conditions of the membrane, in addition to the use of additives.

In the previous decade, a comparison of the properties and the CO₂ absorption performance of three membrane contactors produced from different polymers (PTFE, PP, and PVDF) was reported by Khaisri et al. [77]. From the 3 types of studied contactors, the authors observed that PTFE exhibited the highest CO₂ absorption performance, while PP contactors showed the poorest CO₂ absorption capacity. On the other

hand, the authors examined the stability of PTFE and PVDF contactors during their operation time, noticing that PTFE membranes kept their absorption efficiency after 60 h of operation, something that was not detected in the case of PVDF membranes since a decrease in their capacity to absorb CO₂ was perceived. Despite the excellent absorption properties of PTFE contactors, the high production cost of fluorinated polymers limits their application as membrane contactors.

After that, Porcheron and coworkers evaluated the stability and resistance to contact with MEA solution of several commercial membrane contactors based on 4 different polymers (PP, PVDF, PTFE, and Nylon) to select a membrane that exhibited the best properties to be implemented in a pilot plant for CO₂ absorption [63]. In their work, the authors noticed that porous materials show the best results since PTFE native membranes present the highest gas permeability compared to the other tested membranes because of the methodology used to prepare it allows the obtention of a very porous membrane. In contrast, PP native membrane has the lowest effective permeability because it presents a very small porosity. Additionally, PTFE membranes exhibited the highest stability when they were in contact with MEA solution, as they had not degraded even after two months of use. Regarding PVDF and PP membranes, a notable degradation was detected after being in contact for two months with the solvent, while Nylon membranes exhibited an intense degradation in MEA solution.

Another polymer whose use in CO₂ absorption has not been considered until recent years is PVC due to its low production cost, great processability and good chemical resistance. Fashandi and coworkers described for the first time the preparation of PVC based membranes that were tested as gas-liquid hollow fiber membrane contactors (GLHFMC) to capture CO₂ [76]. After that, Jing Wang *et al.* reported PVC-derived carbon spheres with shape stability that showed remarkable performance in pure CO₂ adsorption, and a good adsorption capacity and recyclability in low-concentration [78].

As mentioned above, the most significant disadvantage of utilizing hydrophobic microporous membranes is that solvent often occupies the membrane porous, which over time decreases the efficiency of CO₂ transport through the membrane. In order to reduce the membrane hydration, different strategies have been investigated (chemical modification of membrane surface, incorporation of additives or preparation of composite membranes) [79]. Recently, the modification of the Polysulfone (PSF) membrane surface was attempted by several research groups. For instance, Kostyanaya and coworkers modified PSF through the deposition of a perfluorinated acrylic copolymer (PAC) in order to increase its inner surface hydrophobic properties, avoiding penetration of the liquid absorbent in the porous structure [80,81]. Moreover, PSF membranes have been modified with several inorganic fillers (mesoporous silicas, zeolites [83], carbon nanotubes [84], silica nanoparticles [85], porous crystals like metal-organic frameworks (MOFs) as core surrounded by a small pore zeolitic imidazolate frameworks (ZIFs) [86]) that showed

improved properties in CO₂ capture applications. Besides, Nogalska and coworkers described the incorporation of CuFe₂O₄ nanoparticles into PSF membrane contactors with distinct morphologies to capture ambient CO₂ and use it to produce other organic compounds [87]. Therefore, they designed and developed an artificial stomata for CO₂ absorption based on polysulfone membrane contactor that is supposed to work as the pores that are present in the leaves of the trees and are responsible for the exchange of gases (Figure 1.19). Moreover, the addition of these nanoparticles provided a higher roughness to the membrane surface and a greater hydrophobic character, properties that are correlated to the enhancement of the ambient CO₂ absorption (67.5 mmol/m²·s).

To produce sustainable and environmental friendly organic fuels such as formic acid or methanol, used in fuel cell systems, the separation and sequestering of CO₂ by membrane/solvent system integrated with an electroreduction system called artificial photosynthesis has shown great potential. The CO₂ electroreduction systems include an anode, cathode, ion conductive membrane, and membrane that mimics the leaf structure for the carbon dioxide capture process from the air (Figure 1.19). The electrochemical conversion of CO₂ is carried at the cathode; the required protons are supplied through the water splitting at the anode and transferred across the ion conductive membrane to the cathode for CO₂ reduction reaction; CO₂ is supplied via the CO₂ capture process from the air by porous membranes (Figure 1.19). In the carbon dioxide capture process, CO₂ gas fixation is achieved when gas penetrates pores of membranes as entitled artificial stomata. Indeed, this phenomenon naturally occurs in leaves where gas penetrates smart adjustable pores, known as stomata. Thus, as a biomimetic solution approach for CO₂ capture processes by gas-liquid membrane contactors in the energy system, artificial stomata are an exciting subject to complement artificial photosynthesis.

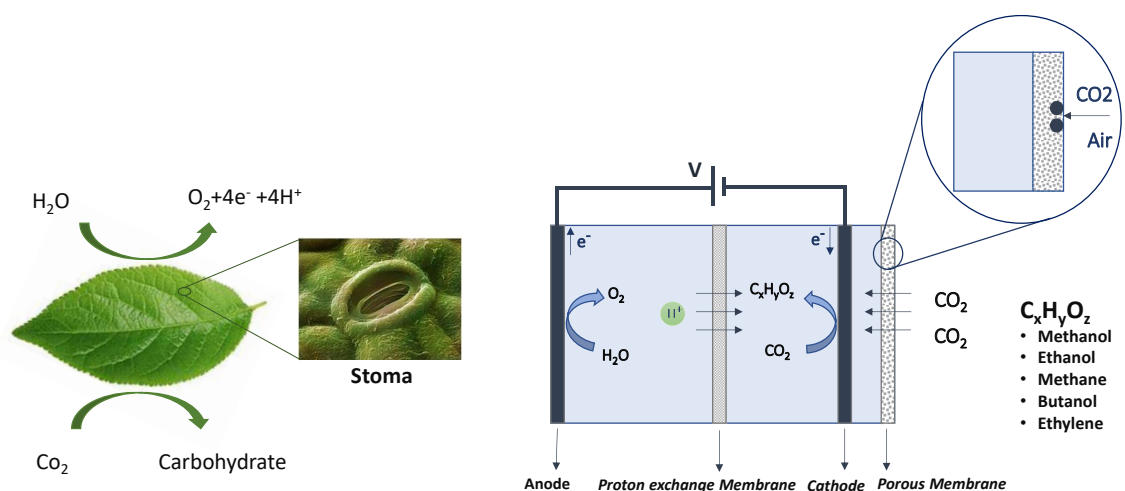


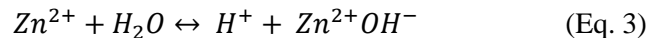
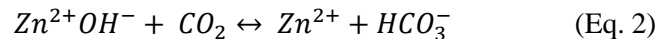
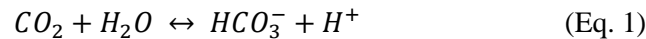
Figure 1.19 Scheme of natural stomata (left), an artificial photosynthetic system (APS), water-splitting APS systems, to utilize solar energy through the conversion of photon-to-fuel by mimicking natural photosynthesis, electroreduction of CO₂ system (right).

The doping of PVDF with inorganic additives was also recently explored by Pang and coworkers [88]. In this case, the authors prepared membranes containing different amounts of two additives (LiCl, phosphoric acid or a mixture of both additives), observing that PVDF membrane with 8 % of phosphoric acid showed the best performance in CO₂ capture, apart from improving the membrane mechanical properties. In the same manner than PSF, other inorganic fillers were employed to ameliorate the CO₂ capture of PVDF membranes: ZIF-7, ZIF-8, Cu-benzene-1,3,5-tricarboxylate (Cu-BTC) [89] or graphene nanosheets [90].

An alternative that has received much attention lately has been the construction of hybrid membranes by combining different polymers. In 2019, Heo *et al.* reported the preparation of PVDF/Polyacrylonitrile (PAN) hybrid membranes that combine the good properties of both porous polymers and showed an improved CO₂ capture performance compared to PAN membranes [91].

- **Bio-catalytic membrane contactors**

To improve CO₂ absorption in gas-liquid membrane contactor systems, membrane surface modification is an interesting option since it has been proven that high CO₂ concentrations on the opposite side of the membrane surface could eventually increase membrane performance, according to Fick's laws of diffusion. Several publications reported that the incorporation of enzymes such as carbonic anhydrase (CA) led to an enhancement of CO₂ absorption dynamics combined with a reduction of the membrane wetting [92]. In fact, carbonic anhydrase (CA) is recognized as a Zn-metalloenzymes that catalyzes the hydration of carbon dioxide into bicarbonate ions (Eq. 1) to maintain acid-base balance in blood and other tissues, and to help transport carbon dioxide out of tissues in both animal and plant cells (for example in natural photosynthesis). In the first part, the catalyst favors the nucleophilic attack of Zn²⁺ bounded to hydroxide ions to carbon dioxide. Then, the active site is then regenerated by ionization of Zn²⁺ bounded to a water molecule followed by the expelling a proton to complete the cycle (Eq. 3).



Generally, an enzyme is incorporated into the membrane through covalent binding or by physical adsorption [93]. Covalent binding on the membrane surface is based on the chemical attachment to functional groups, including epoxy, carboxyl, and amino [93], which results in a strong and stable enzyme support bonding, but it can also limit enzyme activity due to alterations in the enzyme's native structure. Some surface properties can be induced in the membrane by modification while maintaining the bulk

properties. Physical adsorption, that is based on hydrophobic, hydrophilic, or electrostatic interactions, is the most simple and common way of CA incorporation into the surface membrane. However, the only drawback is the leaching of the enzyme due to weaker enzyme-support interactions [94].

1.3.3 Absorbents for CO₂ capture

- **Liquid absorbent for membrane contactors**

Apart from the membrane contactor, the absorbent is the other main component in CO₂ capture technique. The most important factors to take into account when choosing an absorbent are [95]:

- Chemical compatibility with membranes.
- Low vapor pressure and high thermal stability.
- Affinity and selectivity to CO₂.
- Surface tension to prevent membrane wetting.
- Simple renewal
- Non-toxic and non-corrosive [96].

Liquid absorbents are employed in both membrane contactors and packed column contactors. Many types of liquid absorbents can be used, among which we find (Figure 1.20) [61,97]:

- Pure water, aqueous solutions of KOH and NaOH.
- Amino acid salt (AAS) solutions such as potassium glycinate, sodium glycinate, potassium sarcosine, and sodium sarcosine [98].
- Potassium carbonate aqueous solution (K₂CO₃).
- AgNO₃[81].
- Ionic liquids (ILs) [99].
- Alkanolamines: primary amines (monoethanolamine (MEA), ethylamine, propylamine, etc.), secondary amines (diethanolamine (DEA), piperazine, diethylamine, etc.), tertiary amines (triethanolamine (TEA), 1, dimethylamine-1-propanol (3DMA1P), etc.).

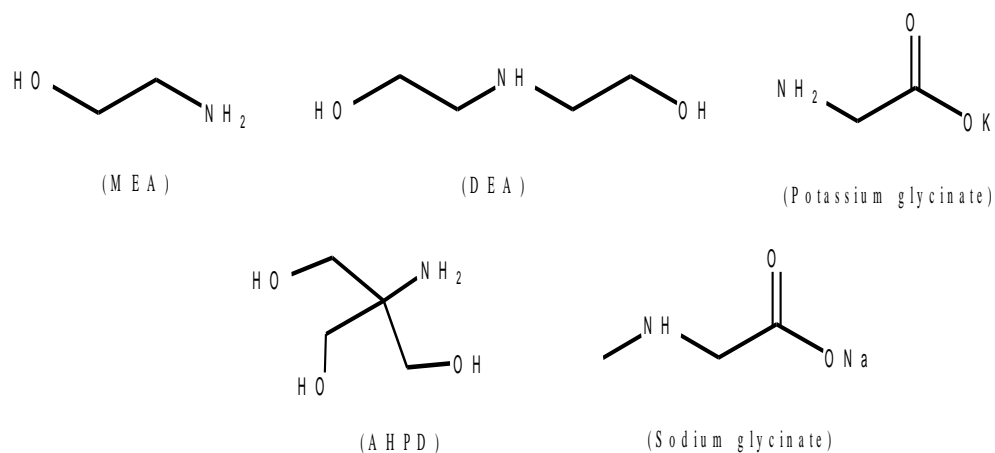


Figure 1.20 Chemical structure of some absorbents used to capture CO₂.

From all of them, MEA solutions are the most used absorbents to capture CO₂ because of many advantages they present (low operating pressure, high CO₂ absorption rate, solubility in water at all concentrations) [100]. Last year, Tian and coworkers built up and characterize a MEA/PEG200 absorbent for CO₂ capture that showed a higher desorption rate compared with a MEA/H₂O absorbent. Moreover, the authors managed to minimize the energy consumption during solvent regeneration up to 33 % compared to MEA/H₂O absorbent and the corrosion, which are the main drawbacks for using MEA in CO₂ absorption systems. Therefore, all the improvements exhibited by these novel MEA/PEG200 absorbent make it a serious candidate to consider for industrial applications [101]. In the same direction, Ulus *et al.* design an innovative blend with MEA/methyl diethanolamine (MDEA) that can work as liquid absorbent. Although MEA/MDEA absorbent exhibited a lower absorption capacity than MEA absorbent, the blend showed a slightly smaller regeneration energy compared to MEA absorbent [102]. However, the fabrication and selection of high-performance liquid absorbents for membrane contactors remain a challenge in the forthcoming years.

1.4 References

1. Höök, M.; Tang, X. Depletion of fossil fuels and anthropogenic climate change—A review. *Energy policy* 2013, 52, 797-809.
2. Perera, F. Pollution from fossil-fuel combustion is the leading environmental threat to global pediatric health and equity: Solutions exist. *International journal of environmental research and public health* 2018, 15, 16.

3. Welsby, D.; Price, J.; Pye, S.; Ekins, P. Unextractable fossil fuels in a 1.5 C world. *Nature* 2021, 597, 230-234.
4. Richards, P.D.; Myers, R.J.; Swinton, S.M.; Walker, R.T. Exchange rates, soybean supply response, and deforestation in South America. *Global environmental change* 2012, 22, 454-462.
5. Ellabban, O.; Abu-Rub, H.; Blaabjerg, F. Renewable energy resources: Current status, future prospects and their enabling technology. *Renewable and sustainable energy reviews* 2014, 39, 748-764.
6. Listorti, A.; Durrant, J.; Barber, J. Solar to fuel. *Nature materials* 2009, 8, 929-930.
7. Handoko, A.D.; Li, K.; Tang, J. Recent progress in artificial photosynthesis: CO₂ photoreduction to valuable chemicals in a heterogeneous system. *Current Opinion in Chemical Engineering* 2013, 2, 200-206.
8. Saikia, K.; Kakati, B.K.; Boro, B.; Verma, A. Current Advances and Applications of Fuel Cell Technologies. In *Recent Advancements in Biofuels and Bioenergy Utilization*; Springer: 2018; pp. 303-337.
9. Fan, L.; Tu, Z.; Chan, S.H. Recent development of hydrogen and fuel cell technologies: A review. *Energy Reports* 2021, 7, 8421-8446.
10. Eggleston, S.; Buendia, L.; Miwa, K.; Ngara, T.; Tanabe, K. IPCC guidelines for national greenhouse gas inventories. 2006.
11. Liu, Z. National carbon emissions from the industry process: Production of glass, soda ash, ammonia, calcium carbide and alumina. *Applied Energy* 2016, 166, 239-244.
12. Florides, G.A.; Christodoulides, P. Global warming and carbon dioxide through sciences. *Environment international* 2009, 35, 390-401.
13. Gür, T.M. Carbon Dioxide Emissions, Capture, Storage and Utilization: Review of Materials, Processes and Technologies. *Progress in Energy and Combustion Science* 2022, 89, 100965.
14. Agency, U.S.E.P. Overview of Greenhouse Gases. Available online: <https://www.epa.gov/ghgemissions/overview-greenhouse-gases#:~:text=Total%20U.S.%20Emissions%20in%202019,100%25%20due%20to%20independent%20rounding> (accessed on February 17, 2022).
15. Atsonios, K.; Panopoulos, K.D.; Kakaras, E. Investigation of technical and economic aspects for methanol production through CO₂ hydrogenation. *International Journal of hydrogen energy* 2016, 41, 2202-2214.
16. Parigi, D.; Giglio, E.; Soto, A.; Santarelli, M. Power-to-fuels through carbon dioxide Re-Utilization and high-temperature electrolysis: A technical and economical comparison between synthetic methanol and methane. *Journal of Cleaner Production* 2019, 226, 679-691.

17. D'Alessandro, D.M.; Smit, B.; Long, J.R. Carbon dioxide capture: prospects for new materials. *Angewandte Chemie International Edition* 2010, 49, 6058-6082.
18. Leung, D.Y.; Caramanna, G.; Maroto-Valer, M.M. An overview of current status of carbon dioxide capture and storage technologies. *Renewable and Sustainable Energy Reviews* 2014, 39, 426-443.
19. Bui, M.; Adjiman, C.S.; Bardow, A.; Anthony, E.J.; Boston, A.; Brown, S.; Fennell, P.S.; Fuss, S.; Galindo, A.; Hackett, L.A. Carbon capture and storage (CCS): the way forward. *Energy & Environmental Science* 2018, 11, 1062-1176.
20. Desport, L.; Selosse, S. An overview of CO₂ capture and utilization in energy models. *Resources, Conservation and Recycling* 2022, 180, 106150.
21. Curtin, D.E.; Lousenberg, R.D.; Henry, T.J.; Tangeman, P.C.; Tisack, M.E. Advanced materials for improved PEMFC performance and life. *Journal of power Sources* 2004, 131, 41-48.
22. Matyjaszewski, K.M.I.M.S.H.-W.U.M. *Polymer science: a comprehensive reference*. Vol. 5, Vol. 5; Elsevier: Amsterdam, 2012.
23. Lin, H.; Ding, Y. *Polymeric membranes: chemistry, physics, and applications*. 2020, 58, 2433-2434.
24. Mecke, A.; Dittrich, C.; Meier, W. Biomimetic membranes designed from amphiphilic block copolymers. *Soft Matter* 2006, 2, 751-759.
25. Ulbricht, M. Advanced functional polymer membranes. *Polymer* 2006, 47, 2217-2262, doi:<https://doi.org/10.1016/j.polymer.2006.01.084>.
26. Shen, Y.-x.; Saboe, P.O.; Sines, I.T.; Erbakan, M.; Kumar, M. Biomimetic membranes: A review. *Journal of Membrane Science* 2014, 454, 359-381, doi:<https://doi.org/10.1016/j.memsci.2013.12.019>.
27. Kamcev, J.; Freeman, B.D. Charged polymer membranes for environmental/energy applications. *Annual review of chemical and biomolecular engineering* 2016, 7, 111-133.
28. Kirubakaran, A.; Jain, S.; Nema, R.K. A review on fuel cell technologies and power electronic interface. *Renewable and Sustainable Energy Reviews* 2009, 13, 2430-2440, doi:<https://doi.org/10.1016/j.rser.2009.04.004>.
29. Deluca, N.W.; Elabd, Y.A. Polymer electrolyte membranes for the direct methanol fuel cell: a review. *Journal of Polymer Science Part B: Polymer Physics* 2006, 44, 2201-2225.
30. Yue, Z.; Cai, Y.-B.; Xu, S. Phosphoric acid-doped cross-linked sulfonated poly (imide-benzimidazole) for proton exchange membrane fuel cell applications. *Journal of Membrane Science* 2016, 501, 220-227.

31. Yee, R.S.L.; Rozendal, R.A.; Zhang, K.; Ladewig, B.P. Cost effective cation exchange membranes: A review. *Chemical Engineering Research and Design* 2012, 90, 950-959, doi:<https://doi.org/10.1016/j.cherd.2011.10.015>.
32. Kreuer, K.D.; Rabenau, A.; Weppner, W. Vehicle mechanism, a new model for the interpretation of the conductivity of fast proton conductors. *Angewandte Chemie International Edition in English* 1982, 21, 208-209.
33. Yang, C.; Costamagna, P.; Srinivasan, S.; Benziger, J.; Bocarsly, A.B. Approaches and technical challenges to high temperature operation of proton exchange membrane fuel cells. *Journal of Power Sources* 2001, 103, 1-9, doi:[https://doi.org/10.1016/S0378-7753\(01\)00812-6](https://doi.org/10.1016/S0378-7753(01)00812-6).
34. Mauritz, K.A.; Moore, R.B. State of Understanding of Nafion. *Chemical Reviews* 2004, 104, 4535-4586, doi:10.1021/cr0207123.
35. Armand, M.; Endres, F.; MacFarlane, D.R.; Ohno, H.; Scrosati, B. Ionic-liquid materials for the electrochemical challenges of the future. *Nature Materials* 2009, 8, 621-629, doi:10.1038/nmat2448.
36. Steele, B.C.H.; Heinzel, A. Materials for fuel-cell technologies. In *Materials for Sustainable Energy*; pp. 224-231.
37. Wang, Y.; Chen, K.S.; Mishler, J.; Cho, S.C.; Adroher, X.C. A review of polymer electrolyte membrane fuel cells: Technology, applications, and needs on fundamental research. *Applied energy* 2011, 88, 981-1007.
38. Del Bakhshayesh, A.R.; Asadi, N.; Alihemmati, A.; Nasrabadi, H.T.; Montaseri, A.; Davaran, S.; Saghati, S.; Akbarzadeh, A.; Abedelahi, A. An overview of advanced biocompatible and biomimetic materials for creation of replacement structures in the musculoskeletal systems: focusing on cartilage tissue engineering. *Journal of biological engineering* 2019, 13, 1-21.
39. Kumar, N.; Goel, G.; Hawi, S.; Goel, S. Nature inspired materials: Emerging trends and prospects. *NPG Asia Materials* 2021, 15.
40. Wang, H.; Yang, Y.; Guo, L. Nature-inspired electrochemical energy-storage materials and devices. *Advanced Energy Materials* 2017, 7, 1601709.
41. Drotleff, S.; Lungwitz, U.; Breunig, M.; Dennis, A.; Blunk, T.; Tessmar, J.; Göpferich, A. Biomimetic polymers in pharmaceutical and biomedical sciences. *European Journal of Pharmaceutics and Biopharmaceutics* 2004, 58, 385-407, doi:<https://doi.org/10.1016/j.ejpb.2004.03.018>.
42. Strathmann, H.; Giorno, L.; Drioli, E. *Introduction to membrane science and technology*; Wiley-VCH Weinheim, Germany:: 2011; Volume 544.

43. Williams, R.J.P. Proton Circuits in Biological Energy Interconversions. *Annual Review of Biophysics and Biophysical Chemistry* 1988, 17, 71-97, doi:10.1146/annurev.bb.17.060188.000443.
44. Bogdanowicz, K.A.; Bhosale, S.V.; Li, Y.; Vankelecom, I.F.J.; Garcia-Valls, R.; Reina, J.A.; Giamberini, M. Mimicking nature: Biomimetic ionic channels. *Journal of Membrane Science* 2016, 509, 10-18, doi:<https://doi.org/10.1016/j.memsci.2016.02.038>.
45. Dulyea, L.M.; Fyles, T.M.; Robertson, G.D. Coupled transport membranes incorporating a polymeric crown ether carboxylic acid. *Journal of membrane science* 1987, 34, 87-108.
46. Voyer, N. Preparation of supramolecular devices using peptide synthesis: design and synthesis of a tubular hexa-crown molecule. *Journal of the American Chemical Society* 1991, 113, 1818-1821, doi:10.1021/ja00005a054.
47. Voyer, N.; Robitaille, M. Novel Functional Artificial Ion Channel. *Journal of the American Chemical Society* 1995, 117, 6599-6600, doi:10.1021/ja00129a027.
48. Meillon, J.C.; Voyer, N. A synthetic transmembrane channel active in lipid bilayers. *Angewandte Chemie International Edition in English* 1997, 36, 967-969.
49. Koert, U.; Stein, M.; Harms, K. A Convergent Synthesis of 2, 5-trans-Linked Oligo (tetrahydrofuran) s: Potential Building Blocks for a Polyether Helix with Ion Channel Activity. *Angewandte Chemie International Edition in English* 1994, 33, 1180-1182.
50. Shenton, W.; Douglas, T.; Young, M.; Stubbs, G.; Mann, S. Inorganic-organic nanotube composites from template mineralization of tobacco mosaic virus. *Advanced Materials* 1999, 11, 253-256.
51. Percec, V.; Heck, J. Liquid crystalline polymers containing mesogenic units based on half-disc and rod-like moieties. I. Synthesis and characterization of 4-(11-undecan-1-yloxy)-4'-[3, 4, 5-tri (p-n-dodecan-1-yloxybenzyloxy) benzoate] biphenyl side groups. *Journal of Polymer Science Part A: Polymer Chemistry* 1991, 29, 591-597.
52. Percec, V.; Schlueter, D.; Ungar, G.; Cheng, S.Z.D.; Zhang, A. Hierarchical control of internal superstructure, diameter, and stability of supramolecular and macromolecular columns generated from tapered monodendritic building blocks. *Macromolecules* 1998, 31, 1745-1762.
53. Percec, V.; Wilson, D.A.; Leowanawat, P.; Wilson, C.J.; Hughes, A.D.; Kaucher, M.S.; Hammer, D.A.; Levine, D.H.; Kim, A.J.; Bates, F.S.; et al. Self-Assembly of Janus Dendrimers into Uniform Dendrimersomes and Other Complex Architectures. *Science* 2010, 328, 1009, doi:10.1126/science.1185547.

54. Tylkowski, B.; Castelao, N.; Giamberini, M.; Garcia-Valls, R.; Reina, J.A.; Gumí, T. The importance of orientation in proton transport of a polymer film based on an oriented self-organized columnar liquid-crystalline polyether. *Materials Science and Engineering: C* 2012, 32, 105-111.
55. Montané, X.; Bhosale, S.V.; Reina, J.A.; Giamberini, M. Columnar liquid crystalline polyglycidol derivatives: A novel alternative for proton-conducting membranes. *Polymer* 2015, 66, 100-109.
56. Montané, X.; Bogdanowicz, K.A.; Colace, G.; Reina, J.A.; Cerruti, P.; Lederer, A.; Giamberini, M. Advances in the design of self-supported ion-conducting membranes-new family of columnar liquid crystalline polyamines. Part 1: Copolymer synthesis and membrane preparation. *Polymer* 2016, 105, 298-309, doi:<https://doi.org/10.1016/j.polymer.2016.10.047>.
57. Bogdanowicz, K.A.; Rapsilber, G.A.; Reina, J.A.; Giamberini, M. Liquid crystalline polymeric wires for selective proton transport, part 1: Wires preparation. *Polymer* 2016, 92, 50-57, doi:<https://doi.org/10.1016/j.polymer.2016.03.073>.
58. Yoshio, M.; Kagata, T.; Hoshino, K.; Mukai, T.; Ohno, H.; Kato, T. One-dimensional ion-conductive polymer films: alignment and fixation of ionic channels formed by self-organization of polymerizable columnar liquid crystals. *Journal of the American Chemical Society* 2006, 128, 5570-5577.
59. Bogdanowicz, K.A.; Pirone, D.; Prats-Reig, J.; Ambrogi, V.; Reina, J.A.; Giamberini, M. In Situ Raman Spectroscopy as a Tool for Structural Insight into Cation Non-Ionomeric Polymer Interactions during Ion Transport. *Polymers* 2018, 10, doi:10.3390/polym10040416.
60. Bogdanowicz, K.A.; Sístat, P.; Reina, J.A.; Giamberini, M. Liquid crystalline polymeric wires for selective proton transport, part 2: Ion transport in solid-state. *Polymer* 2016, 92, 58-65, doi:<https://doi.org/10.1016/j.polymer.2016.03.080>.
61. Yu, C.-H.; Huang, C.-H.; Tan, C.-S. A review of CO₂ capture by absorption and adsorption. *Aerosol and Air Quality Research* 2012, 12, 745-769.
62. Koytsoumpa, E.I.; Bergins, C.; Kakaras, E. The CO₂ economy: Review of CO₂ capture and reuse technologies. *The Journal of Supercritical Fluids* 2018, 132, 3-16, doi:<https://doi.org/10.1016/j.supflu.2017.07.029>.
63. Porcheron, F.; Ferré, D.; Favre, E.; Nguyen, P.T.; Lorain, O.; Mercier, R.; Rougeau, L. Hollow fiber membrane contactors for CO₂ capture: From lab-scale screening to pilot-plant module conception. *Energy Procedia* 2011, 4, 763-770, doi:<https://doi.org/10.1016/j.egypro.2011.01.117>.
64. Ansaloni, L.; Hartono, A.; Awais, M.; Knuutila, H.K.; Deng, L. CO₂ capture using highly viscous amine blends in non-porous membrane contactors. *Chemical Engineering Journal* 2019, 359, 1581-1591.

65. Yeon, S.-H.; Lee, K.-S.; Sea, B.; Park, Y.-I.; Lee, K.-H. Application of pilot-scale membrane contactor hybrid system for removal of carbon dioxide from flue gas. *Journal of Membrane Science* 2005, 257, 156-160, doi:<https://doi.org/10.1016/j.memsci.2004.08.037>.
66. Cao, Y.; Khan, A.; Nakhjiri, A.T.; Albadarin, A.B.; Kurniawan, T.A.; Rezakazemi, M. Recent advancements in molecular separation of gases using microporous membrane systems: A comprehensive review on the applied liquid absorbents. *Journal of Molecular Liquids* 2021, 337, 116439.
67. Mavroudi, M.; Kaldis, S.P.; Sakellaropoulos, G.P. A study of mass transfer resistance in membrane gas-liquid contacting processes. *Journal of Membrane Science* 2006, 272, 103-115, doi:<https://doi.org/10.1016/j.memsci.2005.07.025>.
68. Lim, H.; Goh, K.; Tian, M.; Wang, R. Membrane-based air dehumidification: A comparative review on membrane contactors, separative membranes and adsorptive membranes. *Chinese Journal of Chemical Engineering* 2022.
69. Shimekit, B.; Mukhtar, H.; Ahmad, F.; Maitra, S. Ceramic membranes for the separation of carbon dioxide—a review. *Transactions of the Indian Ceramic Society* 2009, 68, 115-138.
70. Lu, J.; Yu, Y.; Zhou, J.; Song, L.; Hu, X.; Larbot, A. FAS grafted superhydrophobic ceramic membrane. *Applied Surface Science* 2009, 255, 9092-9099, doi:<https://doi.org/10.1016/j.apsusc.2009.06.112>.
71. Lin, Y.-F.; Chang, J.-M.; Ye, Q.; Tung, K.-L. Hydrophobic fluorocarbon-modified silica aerogel tubular membranes with excellent CO₂ recovery ability in membrane contactors. *Applied Energy* 2015, 154, 21-25, doi:<https://doi.org/10.1016/j.apenergy.2015.04.109>.
72. Magnone, E.; Lee, H.J.; Che, J.W.; Park, J.H. High-performance of modified Al₂O₃ hollow fiber membranes for CO₂ absorption at room temperature. *Journal of Industrial and Engineering Chemistry* 2016, 42, 19-22, doi:<https://doi.org/10.1016/j.jiec.2016.07.022>.
73. Abdulhameed, M.A.; Othman, M.H.D.; Ismail, A.F.; Matsuura, T.; Harun, Z.; Rahman, M.A.; Puteh, M.H.; Jaafar, J.; Rezaei, M.; Hubadillah, S.K. Carbon dioxide capture using a superhydrophobic ceramic hollow fibre membrane for gas-liquid contacting process. *Journal of Cleaner Production* 2017, 140, 1731-1738, doi:<https://doi.org/10.1016/j.jclepro.2016.07.015>.
74. Yu, X.; An, L.; Yang, J.; Tu, S.-T.; Yan, J. CO₂ capture using a superhydrophobic ceramic membrane contactor. *Journal of Membrane Science* 2015, 496, 1-12, doi:<https://doi.org/10.1016/j.memsci.2015.08.062>.
75. Saud, I.H.; Othman, M.H.D.; Hubadillah, S.K.; Aziz, M.H.A.; Pauzan, M.A.B.; Ismail, A.F.; Jaafar, J.; Rahman, M.A. Superhydrophobic ceramic hollow fibre membranes for trapping carbon

- dioxide from natural gas via the membrane contactor system. *Journal of the Australian Ceramic Society* 2021, 57, 705-717.
76. Fashandi, H.; Ghodsi, A.; Saghafi, R.; Zarrebini, M. CO₂ absorption using gas-liquid membrane contactors made of highly porous poly(vinyl chloride) hollow fiber membranes. *International Journal of Greenhouse Gas Control* 2016, 52, 13-23, doi:10.1016/j.ijggc.2016.06.010.
77. Khaisri, S.; deMontigny, D.; Tontiwachwuthikul, P.; Jiraratananon, R. Comparing membrane resistance and absorption performance of three different membranes in a gas absorption membrane contactor. *Separation and Purification Technology* 2009, 65, 290-297, doi:<https://doi.org/10.1016/j.seppur.2008.10.035>.
78. Wang, J.; Wang, F.; Duan, H.; Li, Y.; Xu, J.; Huang, Y.; Liu, B.; Zhang, T. Polyvinyl Chloride-Derived Carbon Spheres for CO₂ Adsorption. *ChemSusChem* 2020, 13, 6426-6432.
79. Seoane, B.; Coronas, J.; Gascon, I.; Benavides, M.E.; Karvan, O.; Caro, J.; Kapteijn, F.; Gascon, J. Metal-organic framework based mixed matrix membranes: a solution for highly efficient CO₂ capture? *Chemical Society Reviews* 2015, 44, 2421-2454, doi:10.1039/C4CS00437J.
80. Kostyanaya, M.; Bazhenov, S.; Borisov, I.; Plisko, T.; Vasilevsky, V. Surface modified polysulfone hollow fiber membranes for ethane/ethylene separation using gas-liquid membrane contactors with ionic liquid-based absorbent. *Fibers* 2019, 7, 4.
81. Ovcharova, A.; Vasilevsky, V.; Borisov, I.; Bazhenov, S.; Volkov, A.; Bildyukevich, A.; Volkov, V. Polysulfone porous hollow fiber membranes for ethylene-ethane separation in gas-liquid membrane contactor. *Separation and Purification Technology* 2017, 183, 162-172, doi:<https://doi.org/10.1016/j.seppur.2017.03.023>.
82. Kim, S.; Marand, E.; Ida, J.; Guliants, V.V. Polysulfone and Mesoporous Molecular Sieve MCM-48 Mixed Matrix Membranes for Gas Separation. *Chemistry of Materials* 2006, 18, 1149-1155, doi:10.1021/cm052305o.
83. Gür, T.M. Permselectivity of zeolite filled polysulfone gas separation membranes. *Journal of Membrane Science* 1994, 93, 283-289, doi:[https://doi.org/10.1016/0376-7388\(94\)00102-2](https://doi.org/10.1016/0376-7388(94)00102-2).
84. Kim, S.; Chen, L.; Johnson, J.K.; Marand, E. Polysulfone and functionalized carbon nanotube mixed matrix membranes for gas separation: Theory and experiment. *Journal of Membrane Science* 2007, 294, 147-158, doi:<https://doi.org/10.1016/j.memsci.2007.02.028>.
85. Ahn, J.; Chung, W.-J.; Pinnau, I.; Guiver, M.D. Polysulfone/silica nanoparticle mixed-matrix membranes for gas separation. *Journal of Membrane Science* 2008, 314, 123-133, doi:<https://doi.org/10.1016/j.memsci.2008.01.031>.
86. Song, Z.; Qiu, F.; Zaia, E.W.; Wang, Z.; Kunz, M.; Guo, J.; Brady, M.; Mi, B.; Urban, J.J. Dual-Channel, Molecular-Sieving Core/Shell ZIF@MOF Architectures as Engineered Fillers in Hybrid

- Membranes for Highly Selective CO₂ Separation. *Nano Letters* 2017, 17, 6752-6758, doi:10.1021/acs.nanolett.7b02910.
87. Nogalska, A.; Ammendola, M.; Tylkowski, B.; Ambrogi, V.; Garcia-Valls, R. Ambient CO₂ adsorption via membrane contactors – Value of assimilation from air as nature stomata. *Journal of Membrane Science* 2018, 546, 41-49, doi:<https://doi.org/10.1016/j.memsci.2017.10.007>.
88. Pang, H.; Gong, H.; Du, M.; Shen, Q.; Chen, Z. Effect of non-solvent additive concentration on CO₂ absorption performance of polyvinylidene fluoride hollow fiber membrane contactor. *Separation and Purification Technology* 2018, 191, 38-47, doi:<https://doi.org/10.1016/j.seppur.2017.09.012>.
89. Li, W.; Meng, Q.; Zhang, C.; Zhang, G. Metal–organic framework/PVDF composite membranes with high H₂ permselectivity synthesized by ammoniation. *Chemistry–A European Journal* 2015, 21, 7224-7230.
90. Wu, X.; Zhao, B.; Wang, L.; Zhang, Z.; Zhang, H.; Zhao, X.; Guo, X. Hydrophobic PVDF/graphene hybrid membrane for CO₂ absorption in membrane contactor. *Journal of Membrane Science* 2016, 520, 120-129.
91. Heo, Y.-J.; Zhang, Y.; Rhee, K.Y.; Park, S.-J. Synthesis of PAN/PVDF nanofiber composites-based carbon adsorbents for CO₂ capture. *Composites Part B: Engineering* 2019, 156, 95-99, doi:<https://doi.org/10.1016/j.compositesb.2018.08.057>.
92. Yong, J.K.; Stevens, G.W.; Caruso, F.; Kentish, S.E. In situ layer-by-layer assembled carbonic anhydrase-coated hollow fiber membrane contactor for rapid CO₂ absorption. *Journal of Membrane Science* 2016, 514, 556-565.
93. Jochems, P.; Satyawali, Y.; Diels, L.; Dejonghe, W. Enzyme immobilization on/in polymeric membranes: status, challenges and perspectives in biocatalytic membrane reactors (BMRs). *Green chemistry* 2011, 13, 1609-1623.
94. Zhang, Y.-T.; Zhang, L.; Chen, H.-L.; Zhang, H.-M. Selective separation of low concentration CO₂ using hydrogel immobilized CA enzyme based hollow fiber membrane reactors. *Chemical Engineering Science* 2010, 65, 3199-3207.
95. Li, J.-L.; Chen, B.-H. Review of CO₂ absorption using chemical solvents in hollow fiber membrane contactors. *Separation and Purification Technology* 2005, 41, 109-122.
96. Davidson, R.M. Post-combustion carbon capture from coal fired plants-solvent scrubbing. 2007.
97. Mansourizadeh, A.; Ismail, A.F. Hollow fiber gas–liquid membrane contactors for acid gas capture: A review. *Journal of Hazardous Materials* 2009, 171, 38-53, doi:<https://doi.org/10.1016/j.jhazmat.2009.06.026>.

98. Rahim, N.A.; Ghasem, N.; Al-Marzouqi, M. Absorption of CO₂ from natural gas using different amino acid salt solutions and regeneration using hollow fiber membrane contactors. *Journal of Natural Gas Science and Engineering* 2015, 26, 108-117, doi:<https://doi.org/10.1016/j.jngse.2015.06.010>.
99. Martins, C.F.; Neves, L.A.; Chagas, R.; Ferreira, L.M.; Afonso, C.A.M.; Crespo, J.G.; Coelho, I.M. CO₂ removal from anaesthesia circuits using gas-ionic liquid membrane contactors. *Separation and Purification Technology* 2020, 250, 116983, doi:<https://doi.org/10.1016/j.seppur.2020.116983>.
100. Liu, J.; Kong, C.; Zhang, Z.; Yang, L. A hybrid method combining membrane separation and chemical absorption for flexible CH₄ refinement and CO₂ separation in natural gas. *Greenhouse Gases: Science and Technology* 2022, 12, 189-199.
101. Tian, W.; Ma, K.; Ji, J.; Tang, S.; Zhong, S.; Liu, C.; Yue, H.; Liang, B. Nonaqueous MEA/PEG200 absorbent with high efficiency and low energy consumption for CO₂ capture. *Industrial & Engineering Chemistry Research* 2021, 60, 3871-3880.
102. Ulus, N.; Syed Ali, S.A.; Khalifa, O.; Orhan, O.Y.; Elkamel, A. Optimization of novel nonaqueous hexanol-based monoethanolamine/methyl diethanolamine solvent for CO₂ absorption. *International Journal of Energy Research* 2022.

1.5 Objectives of the thesis

Ion conductive and CO₂ capture membranes play an essential role in the CO₂ reduction system to capture and convert CO₂ to raw fuel to restore or use in renewable energy devices. The objectives of this doctoral thesis can be summarized as follows:

A) Biomimetic ion conductive membranes

- Deep investigation on how different parameters, such as grafting degree, annealing temperature, annealing time, and cooling rate, influence the self-assembly and self-organization of synthesized side-chain liquid crystalline copolyethers.
- Investigation of the effects of the dendron amount and of the orientation on copolymer mobility by dynamic mechanical thermal analysis (DMTA) and dielectric thermal analysis (DETA) to understand the role of the backbone in self-assembled structure and the interaction between dendritic side groups.
- Determination of how the presence of two different amounts of grafted dendrons can affect the cation transport capacity of oriented membranes by means of methanol and proton permeability, together with linear sweep voltammetry (LSV) analysis.
- Examination of the properties such as the wettability, the morphology, and the topography of unoriented and oriented membranes to understand the evolution of the self-assembly process that occurs in the ionic channels and the final organization of the polymeric columns, for the purpose of optimizing the design of membranes, and obtain good performance in operative conditions.

B) Polymeric membranes as contactors in a gas/liquid system for CO₂ capture from air

- Synthesis and characterization of two different types of amine additives based on a commercial hyperbranched Polyethylene imine Lupasol G20, partially chemically modified with benzoyl chloride (mG20) or phenyl isocyanate via urea linkages (UG20).
- Preparation of flat sheet polysulfone (PSf) membrane by blending PSf with two different types of modified Lupasol G20 additives (mG20 and UG20) with the different amounts by a phase inversion precipitation method as membrane contactor for direct air CO₂ capture at ambient pressure.
- Assessment of the influence of amine additives on the final characteristics of the membranes, as regards morphology, porosity, wettability, stability to aqueous KOH, thermal, dielectrical, and mechanical properties
- Analysis of the performance of the resulting membranes in terms of CO₂ solubility, mass transfer coefficient and capture in the final device.



Chapter 2.

Membranes for cation transport based on dendronized Poly (epichlorohydrin-co-ethylene oxide). Part 1: the effect of the dendron amount and column orientation on the copolymer mobility

UNIVERSITAT ROVIRA I VIRGILI
NOVEL POLYMERIC MEMBRANES FOR ARTIFICIAL PHOTOSYNTHESIS
Alireza Zare

2.1 Introduction

Since Daniel Vorländer described in 1923 the synthesis of the first polymers that contains benzenes connected by ester bonds in the main chain [1], LCP (liquid-crystalline polymers) have been widely investigated due to their exceptional mechanical, optical and electrical properties [2,3], with their unique attribute being that LC phases can flow like liquids and can preserve the natural anisotropic structure of the glassy solid state [4,5]. This singular combination of properties is responsible for the wide range of applications that LCP presents, such as in optical data storage [6], non-linear optics [7], optical compensators [8], electronic devices [9], solid polymer electrolytes [10] and separation membranes [11]. The design and construction of membranes from LCP have aroused a great deal of interest recently owing to the importance of producing energy in a sustainable manner (artificial photosynthesis devices and fuel cells) and also for storing energy (electric batteries) [12-14], with the aim of trying to reproduce biological liquid-crystalline structures [15,16].

Percec and co-workers were the first to discover and examine the intramolecular self-assembly and self-organization processes of side-chain liquid-crystalline polymers (SCLCPs) into columnar structures, in which the main polymer chain is arranged into a helical inner channel surrounded by the side-chain dendrons due to an exo-recognition process of the aromatic moieties in the side-chain mesogenic groups [17,18].

In the last decade, the synthesis of side-chain liquid-crystalline polyethers and polyamines bearing different amounts of the dendron 3,4,5-tris[4-(n-dodecan-1-yloxy)bezyloxy]benzoate (Tap) grafted to the polymer backbone that self-assemble into a columnar structure and the subsequent preparation of membranes derived from these SCLCPs have been extensively studied by our research group [19-22]. The presence of electronegative atoms like oxygen or nitrogen in the polymeric backbone could favour interaction with cations, providing hydrophobic selective transport systems that exhibit proton permeability compared to Nafion[®], the benchmark material in proton conductivity [23-25]. However, the complex self-assembly and self-organization processes of dendronized polymers can be tuned using different methods (e.g., thermal or light treatment, shearing, spinning) in order to obtain a precise channel orientation of the polymeric columns that facilitates ion transport across them [26]. As a matter of fact, several studies conducted by our research group have shown that the thermal orientation can substantially favour the self-assembly process induced by the dendronized polymeric columns, providing a more ordered structure in which an alignment of the polymeric columns perpendicular to the surface of the membrane is desired [21-23,27]. Therefore, an in-depth characterization of these membranes and their orientation is essential to achieve our goal, which was accomplished in recent studies by means of differential scanning calorimetry

(DSC), polarized optical microscopy (POM), X-ray diffraction (XRD) and dynamic-mechanical thermal analysis (DMTA). Moreover, dielectric spectroscopy and solid-state NMR experiments have provided information on the mobility of each region of dendronized polyamines and polyethers, respectively [28,29]. These investigations focused on studying the effects that the degree of modification has on the orientation of the polymer columns and the molecular dynamics in unoriented and oriented polymer membranes, showing that the external aliphatic moieties of the side dendrons are mobile even at low temperatures, while increasing the temperature gradually increases the mobility of the central units of the polymer chains. Nonetheless, other factors, such as the length of the polymer chains, which may affect the final organization of the membrane polymer chains must also be considered before carrying out the process of annealing of the membranes.

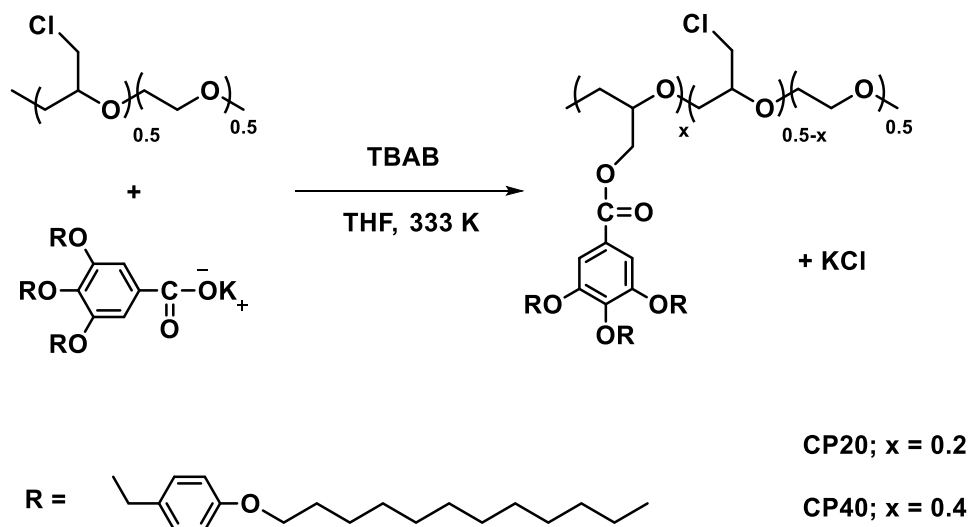
Thus, the purpose of this work was to carry out a deep investigation on how different parameters, such as grafting degree, annealing temperature, annealing time and cooling rate, influence the self-assembly and self-organization of synthesized side-chain liquidcrystalline copolyethers. These parameters were analysed in two Poly(epichlorohydrin-co-ethylene oxide) (PECH-co-EO) liquid crystalline polymers, which presented a different amount of grafted side-chain dendron methyl 3,4,5-tris[4-(n-dodecan-1-yl-oxo)benzyloxy]benzoate (Tap) in quantities of 20% (CP20) and 40% (CP40), respectively. For sake of comparison, we also analysed the features of the unmodified PECH-co-EO (CP0). The experiments performed with these liquid crystalline copolyethers show that the cooling rate from the isotropic phase to the annealing temperature and the selection of the annealing temperature play crucial roles in the orientation of the columns of both copolymers. In addition, it was found that grafting induces crystallinity in the copolymer main chain, which increases upon the orientation of the columns. In the present work, the effects of the dendron amount and of the orientation on copolymer mobility were investigated by dynamic mechanical thermal analysis (DMTA) and dielectric thermal analysis (DETA). Therefore, it is possible to understand the role of the backbone in self-assembled structures and the interaction between dendritic side groups. This information is very important to design membranes that offer a specific orientation and size of their columnar structure, and consequently to obtain good performance in operative conditions, for instance, for fuel cell applications [30].

2.2 Materials and Methods

2.2.1 Materials

Inorganic and organic compounds were purchased from Sigma Aldrich (Sigma Aldrich Química, Madrid, Spain) and Fisher Scientific (Fisher Scientific Spain, Madrid, Spain) and used as received. All the solvents were purchased from Scharlab (Scharlab, S.L., Barcelona, Spain). Potassium 3,4,5-tris[4-(n-dodecan-1-yloxy)benzyloxy]benzoate (Tap) was synthesized according to the previous report [22]. Poly(epichlorohydrin-co-ethylene oxide) (P(ECH-co-EO) 1:1, $M_w = 5.01 \times 10^5$, $M_n = 1.08 \times 10^5$ determined by gel permeation chromatography) was purchase from Sigma-Aldrich and used as received.

For modification of Poly(epichlorohydrin-co-ethylene oxide) (PECH-co-EO), 0.500 g of PECH-co-EO was dissolved in 70 mL THF. Then, the stoichiometric amount of potassium methyl 3,4,5-tris[4-(n-dodecan-1-yloxy)benzyloxy] benzoate (Tap) was added to the copolymer. After that, stoichiometric amount of tetrabutylammonium bromide (TBAB) was added in a flask and stirred for 8 or 10 days at 333 K. The mixture was poured in ice water, and the obtained precipitate was filtered. For further purification, the precipitate was dissolved in THF and precipitated in ethanol twice to yield 2.37 g (55%) of a white product. The modification degree was calculated by the ^1H NMR spectra of the copolymer. The mechanism of modification of the copolymer with the Tap group is shown in Scheme 2.1.



Scheme 2.1 Synthesis of the copolymers.

In this study, this chemical modification was carried out under different reaction conditions, which are given in Table 2.1. The copolymers were obtained with modification degrees of 20, 35, 40, respectively, which consisted of the total modification degrees of PECH-co-EO units with Tap. ^1H NMR was used to determine the modification degree of these copolymers by comparing the normalized area value of a

chemically modified region with Tap and the normalized area value of modified plus unmodified regions. In fact, 3 different modified regions (benzylic positions, aliphatic chains of the TAP and aromatic units) were used to calculate the chemical modification degrees. In all the cases the same modification degree was obtained in the 3 regions for each polymer. In this paper, we focused our attention on the copolymers modified at 20 and 40%, which were labelled CP20 and CP40, according to Scheme 2.1. The unmodified PECH-co-EO was labelled as CP0.

Table 2.1 Reaction conditions and resulting modification degrees and yields for P(ECH-co-EO) modification with Tap.

Sample	Chlorine/Tap (mol/mol)	PECH-coEO (mol·10 ⁻³)	Tap (mol·10 ⁻³)	Time (days)	T(K)	Modification degree of PECH-co-EO (%)	Yield (%)
CP20	1:0.5	7.4	3.7	8	333	20	75
CP35	1:1	3.7	3.7	8	333	35	55
CP40	1:1	3.7	3.7	10	333	40	65

2.2.2 Membrane preparation

Membranes were prepared by the immersion precipitation method. The modified copolymer was dissolved in THF (30% w/w). After that, the homogeneous solution was cast by a casting machine (K-paint applicator, RK Paintcoat Instruments Ltd., Litlington, UK) on an FEP (fluorinated ethylene propylene) sheet support with a controlled thickness (gap size 300 μm). Then, the support, including the wet film on top, was immersed in a bath of Milli-Q water in which the polymeric membrane was formed with an asymmetric structure. After 24 h, the formed membrane was dried overnight at room temperature. The thicknesses of membranes were measured using a micrometer with a sensitivity of 2 μm..

To achieve the homeotropically oriented structure of the modified copolymer, the polymeric membrane (approx. 2 cm diameter) was placed on a hot stage (Linkam TP92, Linkam Scientific Instruments Ltd., Tadworth, UK) for the orientation process. In general, for annealing, the membrane was heated up to above its clearing temperature. Afterwards, it was allowed to cool slowly to the annealing temperature where it was kept for a variable time. After annealing, the membrane was cooled to room temperature. Finally, the uniform membrane was left at room temperature for 1h and then detached from the FEP support. In order to find the best conditions for orientation, different thermal treatment procedures were carried out, including different cooling rates (1 K/min to 0.1 K/min), annealing temperatures (363 to 380 K), and annealing times (50 h to 120 h). For scale-up, the same procedure was performed in a Hewlett Packard 5890 Series II Gas Chromatograph oven (Hewlett Packard, Palo Alto, CA, USA).

2.2.3 Characterization techniques

X-ray diffraction measurements (XRD) were made using a Bruker-AXS D8-Advance diffractometer (Billerica, USA) with vertical theta-theta goniometer, incident- and diffracted-beam Soller slits of 2.5° , a fixed 0.5° receiving slit and an air-scattering knife on the sample surface. The angular 2θ range was between 1 and 40° . The data were collected with an angular step of 0.02° at a step/time of 0.5s . $\text{CuK}\alpha$ radiation was obtained from a copper X-ray tube operated at 40 kV and 40 mA . Diffracted X-rays were detected with a PSD detector LynxEye-XE-T (Bruker, Billerica, USA) with an opening angle of 2.94° . Sample was placed inside a MTC-LOWTEMP chamber for in-situ temperature analysis.

The diffractograms were interpreted with the software DIFFRAC.EVA 5.2 from BRUKER.AXS and the database PDF-2 release 2018 from ICDD (International Center for Diffraction Data).

Calorimetric analyses were performed in aluminium standard $40\ \mu\text{L}$ crucibles without pin (ME-26763) with a Mettler DSC822e thermal analyser (Mettler Toledo, Columbus, OH, USA) at the heating rate of $10\text{K}/\text{min}$ with about 5 mg of sample, nitrogen as a purge gas ($100\text{ mL}/\text{min}$) and liquid nitrogen for the cooling system. The equipment was previously calibrated with indium (156.6°C) and zinc (418.6°C) pearls.

^1H NMR spectra were recorded at 400 MHz on a Varian Gemini 400 spectrometer (Varian, UK). Deuterated chloroform (CDCl_3) was used as solvent and the chemical shifts were given in parts per million from TMS (Tetramethylsilane). A pulse delay time of 5 s was always used to record ^1H NMR spectra of the polymers.

Clearing temperatures and LC mesophases were investigated by polarised optical microscopy (POM); textures of the samples were observed with an Axiolab Zeiss (Carl Zeiss, Jena, Germany) optical microscope equipped with a Linkam TP92 hot stage (Linkam Scientific Instruments Ltd., Tadworth, UK).

DMTA measurements were performed using a TA Q800 analyzer, TA Instruments (New Castle, DE., USA) in tensile mode in rectangular films of circa 15 mm in length, 0.07 mm in thickness and 1.1 mm in width. An oscillation strain of 0.08 at 10 Hz was imposed from 123 K to 373 K at $2\text{ K}/\text{min}$.

The Dielectric Thermal Analysis (DETA) was performed using a Dielectric Spectrometer from Novocontrol Technologies GmbH & Co. KG, Hundsangen, Germany. The measurements were performed in the frequency range of 10^{-1} to 10^7 Hz between 123 K to 383 K , under isothermal conditions by increasing steps of 10 K . The dielectric experiments were performed in a cell constituted by two gold electrodes were the sample electrode assembly (SEA), consisting of two stainless steel electrodes, was located.

The measured dielectric relaxation spectra were fitted using the Havriliak-Negami (HN) functions, by adding as many HN functions as needed, following the proposal of Charlesworth. All the characteristic parameters of each relaxation process were determined as shown in Equation (1) [31-33].

$$\varepsilon^*(\omega) - \varepsilon_\infty = \sum_k \text{Im} \left[\frac{\Delta\varepsilon}{\left\{ 1 + (i\omega\tau_{HNk})^{a_k} \right\}^{b_k}} \right] \quad (1)$$

Where:

τ_{HN} is the Havriliak-Negami relaxation time. Thus, the sub index k represents the number of the individual HN contributions.

a and b are parameters corresponding to the width and asymmetry broadening of the relaxation peak of the relaxation time distributions.

$\Delta\varepsilon$ is the value of the dielectric intensity or relaxation strength.

2.3 Results

Chemical modification of Poly(epichlorohydrin-co-ethylene oxide) (PECH-co-EO) was performed with the dendron potassium 3,4,5-tris[4-(n-dodecan-1-yloxy)benzyloxy]benzoate (Tap). Based on our previous results, the best results were obtained in THF at 333 K for 8 days with stoichiometric amounts of TBAB. It was shown that no improvement resulted from either changing the solvent to NMP or DMF, or increasing the Tap/chlorine molar ratio above 1:1 [19]. On the other hand, in this investigation we found that by performing the reaction for 10 days, the modification degree could be slightly increased in the case of the 1:1 Tap/chlorine molar ratio from around 70 to 80%, although the complete reaction of the nucleophile Tap could never be reached. The modification degree of the copolymers was calculated from the ^1H NMR experiments in CDCl_3 by comparing the areas of the aromatic peaks between 7.4 and 6.8 ppm, the benzylic proton signals at 4.8 ppm and the methylenic protons of modified units at 4.4 ppm, with the broad signal between 4 and 3.5 ppm, relative to the methylenic and methynic protons from the unmodified and modified units, as previously reported [19]. For the sake of clarity, the ^1H NMR spectrum in CDCl_3 of CP40 is reported in Figure 2.S1. In this study, in order to elucidate how the Tap amount affects the final material characteristics, we focused our attention on the copolymers modified by 40 (CP20) and 80% (CP40), respectively.

2.3.1 Thermal, microscopic and X-ray diffraction characterization

The copolymers under investigation, and the unmodified PECH-co-EO, were characterized by differential scanning calorimetry (DSC), polarized optical microscopy (POM) and X-ray diffraction (XRD), in order to establish the presence or absence of crystallinity and/or liquid crystallinity. In the case of CP20 and CP40, DSC and XRD characterizations were also performed on the membranes oriented as described below.

The results of calorimetric analysis are shown in Table 2.2.

Table 2.2 Calorimetric characterization of CP0, CP20 and C40. Glass transition (T_g), melting (T_m) and clearing (T_{cl}) temperatures; melting (ΔH_m) and clearing (ΔH_{cl}) enthalpies per mol repetitive unit; crystallization degree (X_c). Data relative to unoriented samples determined from DSC second heating scan.

Sample	T_g (K)	T_m (K)	ΔH_m (kJ/mol)	X_c (%)	T_{cl} (K)	ΔH_{cl} (kJ/mol)
CP0	241	-	-	-	-	-
CP20	262	308	2.79	32	378	0.061
CP20 oriented	n.d.	312	3.27	38	377*	n.d.
CP40	262	308	2.56	30	383	0.17
CP40 oriented	258	314	4.78	52	383	0.14

* From POM observation. N.d.: Not determined.

In the case of the unmodified CP0, only the glass transition could be evidenced in the DSC thermogram, at around 241 K. Nevertheless, the presence of some crystallinity cannot be totally ruled out. For instance, Jin et al. reported on amorphous blends of poly (methyl methacrylate)/poly (ethylene oxide). They found some difference between the calculated composition from NMR and the known bulk composition that suggested the presence of ~5 wt % phase-separated PEO in addition to a mixed amorphous phase and postulated that the phase-separated PEO arose from the constrained and crystalline units, but no PEO crystallinity was detected by DSC [34].

The glass transition temperature was shown to increase as a consequence of the copolymer modification with Tap. This could be reasonably expected, based on the restrictions on main chain mobility determined by the steric hindrance of this moiety. On the other hand, CP20 and CP40 showed two endotherms, which, according to POM observation and XRD experiments, could be attributed to the melting of the main chain and the clearing of the LC phase, respectively. Figure 2.1 shows optical micrographs under crossed polarizers of CP40 at various temperatures.

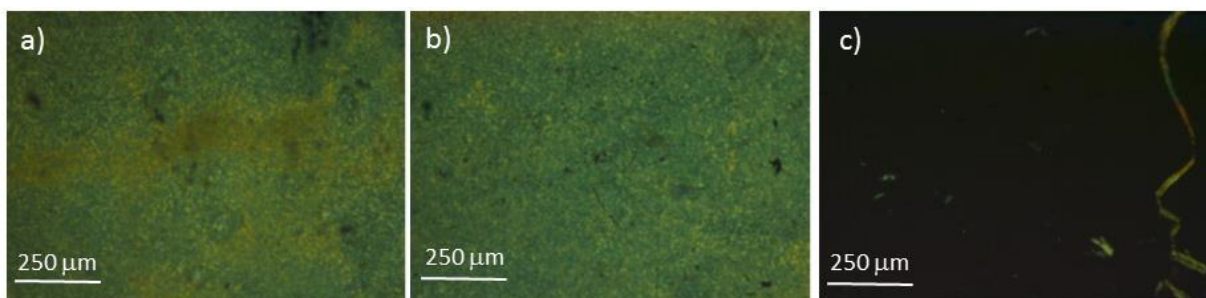


Figure 2.1 Optical micrographs under crossed polarizers of CP40 at 300 K (a), 335 K (b) and 433 K (c).

At 300 K and 335 K, a birefringent texture characteristic of a liquid crystalline phase, could be observed by POM (Figure 2.1a,b). The differences between the patterns observed at these temperatures are difficult to describe. Nevertheless, birefringence completely disappeared above 383 K, thus suggesting that the endotherm observed at this temperature in DSC corresponds to the clearing of the LC phase. The clearing temperatures found for CP20 and CP40 are in agreement with those determined for the copolymers from the same family that have been previously report [19]. In our previous investigation, we could not evidence any crystallinity from XRD and the presence of a crystalline phase was suggested by the presence of two relaxation processes in the ^{13}C NMR spectrum of the methylenic carbon of the modified units.

Figure 2.2. demonstrates the Wide Angle (WA) XRD pattern of CP0, CP20 and CP40 at room temperature.

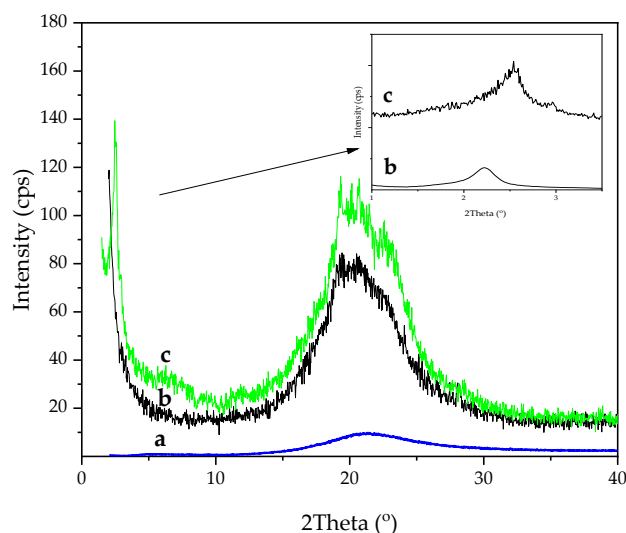


Figure 2.2 WAXD at room temperature of: CP0 (a), CP40 (b) and CP20 (c). Inset: SAXD of CP40 (b) and CP20 (c).

As far as CP0 is concerned, the XRD pattern only showed a halo around $2\theta=20^\circ$, indicative of an amorphous phase. This sample was annealed at 328 K for variable time, but no change could be detected in its XRD pattern. CP20 and CP40 exhibited a more intense, clearly asymmetric halo around $2\theta=20^\circ$, which suggests the presence of some crystalline reflections approximately between $2\theta=18^\circ$ and 24° . This asymmetry vanished when the sample was heated to 323 K, as shown in Figure 2.3 for CP40.

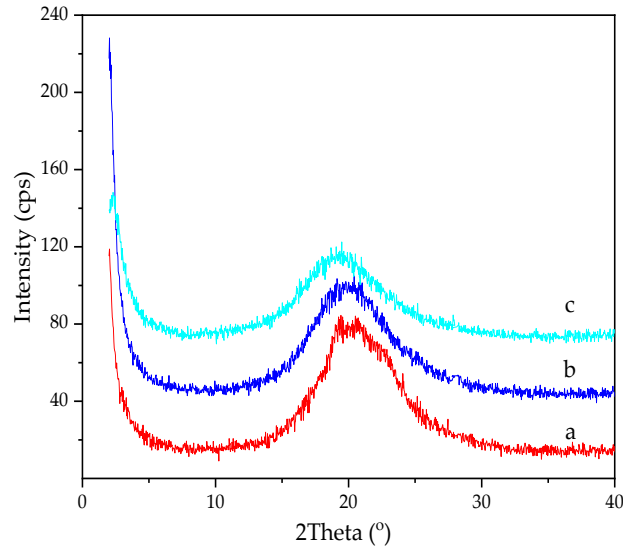


Figure 2.3 WAXD of CP40 at: 293 K (a), 323 K (b) and 393 K (c).

This diffraction angle region also coincides with the WAXD pattern of crystalline poly (ethylene oxide) [35]. Therefore, it can be reasonably concluded that the melting observed in CP20 and CP40 comes from a main chain partial crystallization of the polyether chain.

From the calorimetric data, as an approximation, we could roughly estimate the degree of crystallinity X_c of the copolymers using the following equation:

$$x_c = \frac{\Delta H_m}{\Delta H_{m100}} \cdot 100 \quad (2)$$

Where ΔH_m is the experimental melting enthalpy value and ΔH_{m100} is the reported melting enthalpy for 100% crystalline Poly(ethylene oxide), used as a reference [36]. The resulting values are shown in Table 2.2. Although the calculated absolute values of crystallinity are strongly affected by the approximations performed, the comparison among the different systems showed interesting evidence. While the unoriented CP40 and CP20 exhibited similar X_c and melting temperature values, both samples obtained after the

orientation of the columns, as described below, exhibited increased melting temperatures and crystallinity degrees over the unoriented copolymer. This effect was much more evident for CP40, which had the highest modification degree. Therefore, it can be reasonably concluded that the presence of the dendrons is able to induce order in the copolymer main chain, and this effect is more evident when they are oriented. A certain order in the main chain induced by side modification was also evidenced by Reina et al. in PECH-co-EO modified with 10-undecenoate and 4-pentenoate [37]. The effect found in CP20 and CP40 was more deeply investigated by DMTA and DETA analyses, as reported below.

Concerning the XRD pattern in the small angle region (SAXD), a sharp reflection at $2\theta = 2.2^\circ$ (CP40) and $2\theta = 2.3^\circ$ (CP20), respectively, could be seen (Figure 2.2, inset), which was compatible with the presence of a columnar mesophase. The corresponding spacing of 40 Å and 38 Å, respectively, corresponded to the (100) plane and can be attributed to the distance between columns, similarly to our previously investigated systems [19,22,23,38,39]. The diffuse halo around $2\theta = 20^\circ$ was related to the distance between disks. From these values, we could calculate the dimension of the unit cell (parameter a), which was about 46 Å for CP40 and 44 Å for CP20, respectively.

As far as the mesophase stability of the oriented membranes is concerned, when determined by DSC (Table 2.2), we found no difference in the clearing temperature and a slight decrease of the clearing enthalpy for CP40, while in the thermogram of the oriented CP20, neither T_g nor the peak corresponding to the clearing could be detected, and the clearing temperature was detected by POM. Therefore, the clearing enthalpy could not be calculated.

2.3.2 Optimization of the orientation procedure

As previously stated, the use of membranes based on columnar polymers for cation transport requires the proper orientation of the columns for them to work as ion channels. For this purpose, we based our analysis on the findings of Percec et al., who stated that the columnar self-assembly of dendronized polymers is driven by the aromatic moieties, which induce a helical arrangement. Therefore, these materials can be homeotropically oriented by slowly cooling them from the molten state to room temperature, due to the π - π stacking of aromatic moieties [30]. Indeed, we could successfully apply this approach to several systems of our synthesis, based on dendronized polyethers or polyamines [20-25,27]. In a previous paper, we investigated the influence of the used support on the final polymer orientation [23], and found that it does not play a crucial role, which seems to indicate that the hierarchical structures of these dendronized copolymers tend to form down from the top surface. It must be remembered that the aliphatic tails present in the dendrons possess high mobility and low surface energy. Therefore, their higher air compatibility and entropy may favour their movement toward the air interface over the main chain components.

Consequently, one can suppose the anchoring of the dendrons to the air interface. An analogous behaviour was recently found in the case of the nanocylinder orientation of a liquid crystal block of copolymer film based on poly(ethylene oxide) and a polymethacrylate bearing azobenzene mesogen side chains [40]. In the end, we chose FEP as a convenient support for membrane preparation and thermal orientation, since they could be easily peeled off.

In our previous studies [21-23,27], we could get satisfactory orientation of the mesogenic columns, which led to promising transport properties; nevertheless, we did not examine the influence of different parameters, i.e., annealing temperature, cooling rate and annealing time, on the final degree of orientation. In this paper, we tried to optimize the procedure for the thermal orientation of CP20 and CP40. Given the similarities of the two systems in the initial clearing temperatures and crystallinity degrees, we fine-tuned the thermal treatment on CP40 membranes and successfully applied the same procedure to CP20. In this regard, four procedures were carried out:

- For sample CP40 (a), the membrane was heated up (10 K/min) to 398 K, then it was cooled slowly (1 K/min) to 363 K where it was kept for 50 h and subsequently cooled to room temperature at a rate of 10 K/min.

- For sample CP40 (b), the membrane was heated up (10 K/min) to 413 K, then it was cooled slowly (1 K/min) to 378 K where it was kept for 50 h. In the end, the membrane was allowed to cool (10 K/min) to room temperature.

- In the case of sample CP40 (c), the membrane was heated up (10 K/min) to 413 K, then it was cooled slowly (0.1 K/min) to 378 K where it was kept for 69 h. Finally, the membrane was allowed to cool (10 K/min) to room temperature.

- For sample CP40 (d), the membrane was heated up (10 K/min) to 413 K. It was kept at the same temperature for 30 min. Then it was cooled slowly (0.1 K/min) to 380 K where it was kept for 120 h. Finally, the membrane was allowed to cool to room temperature at 10 K/min.

As a parameter indicating the achieved columnar orientation, we chose the width at half height (WHH) of the peak obtained from the azimuthal scan of the reflection at $2\theta = 2.2^\circ$ (corresponding to the intercolumnar distance). The different procedures applied are summarized in Table 2.3. The resulting WHH values and Debye rings of XRD patterns indicative of the achieved orientation are shown in Table 2.3 and Figure 2.4, respectively. The Intensity versus azimuthal angle graphs are shown in Figure 2.S2.

Table 2.3 Different thermal treatments and resulting peak width at half height (WHH) and angle of orientation of annealed membranes of the CP40 sample.

Sample	Annealing Temperature (K)	Cooling rate (K/min)	Annealing Time (hours)	WHH (°)	Angle of orientation (°)
CP40 (a)	363	1	50	No orientation	-
CP40 (b)	378	1	50	No orientation	-
CP40 (c)	378	0.1	69	92	90
CP40 (d)	380	0.1	120	8.3	90

As it is evident from Figure 2.4a,b, samples CP40 (a) and CP40 (b) show no column orientation at all, as demonstrated by the absence of any polarization of the 2θ reflection at 2.2° . On the other hand, for sample CP40 (c) this reflection exhibits some polarization (Figure 2.4c), giving a WHH = 92° and in CP40 (d) it lies in the equator (Figure 2.4d), which corresponds to a diffraction in the membrane plane. In this last case, the WHH was 8.3° , indicating that the intercolumnar distance is mainly lying in this plane. The peak maximum in the azimuthal scan as located at 90° both in CP40(c) and (d), confirming that homeotropic orientation of the columns can be achieved, Although it was just partially in the case of CP40(c). Given this evidence, one can draw the following conclusions with regards to the orientation procedure:

- The cooling rate from the isotropic phase to the annealing temperature seems to play a crucial role: the lower the rate, the better the orientation.

- The annealing temperature should be as close as possible to the clearing point determined by DSC. In this regard, given the higher mobility of the copolymer at higher temperatures, one has to increase the annealing time accordingly, i.e., we passed from 69 hours in the case of $T_{\text{clearing}} - T_{\text{annealing}} = 5 \text{ K}$ (CP40(c)), to 120 hours for $T_{\text{clearing}} - T_{\text{annealing}} = 3 \text{ K}$ (CP40(d)). It must be also pointed out that when CP40 was annealed at 378 K ($T_{\text{clearing}} - T_{\text{annealing}} = 5 \text{ K}$) for longer times, no improvement in column orientation was achieved.

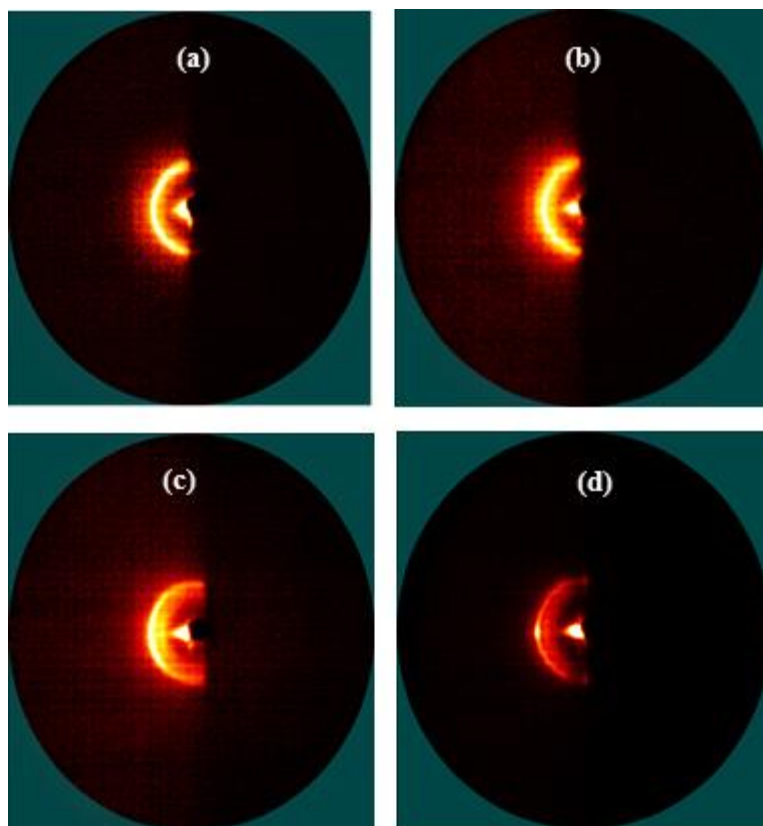


Figure 2.4 Debye ring pattern of CP40 (samples (a) – (d)) after the thermal treatment with different conditions.

2.3.3 Dynamic-mechanical thermal analysis (DMTA)

The modified copolymers CP20 and CP40, and the unmodified CP0, were further investigated by dynamic mechanical thermal analysis (DMTA). Changes in the complex moduli and peaks in the $\tan\delta$ curve can be used to identify the amount of crystallinity and/or liquid crystallinity as it affects the transition temperatures (T_g and T_m), and the viscoelastic properties. In the case of CP20 and CP40, a DMTA characterization was also performed on the oriented membranes.

In Figure 2.5 significant differences can be observed in the DMTA behavior between unmodified CP0 and the modified CP20 and CP40 samples. $\tan\delta$ peak (Figure 2.5a) in sample CP0 is sharp and high, but shifts to higher temperature, decreases in amplitude and significantly widens as the degree of modification increases. This effect is similar but more evident in loss modulus peaks (Figure 2.5b) located at around 237 K for CP0, 238 K for CP20 and 250 K for CP40. The degree of crystallinity has the effect of limiting the motion of the main chain, which becomes more mobile as it is heated up through its glass transition temperature. Since the glass transition is due to the increased movement of the amorphous phase, an increase in the degree of crystallinity produces an increase in the T_g , together with a widening of the

transition, because more thermal energy is needed for the main chain to become mobile and able to dissipate energy. The increase in the degree of modification was also evidenced by a slight increase in the melting temperature of the main chain detected with a small peak in the $\tan\delta$ curve or a sharp decrease in loss modulus from 314 K for CP20 to 319 K for CP40. Concerning the storage modulus evolution (Figure 2.5c) the behavior in the glass transition region was similar to the loss modulus or $\tan\delta$, although less evident. For the CP0 sample, the drop of the storage modulus in the transition region was sudden and sharp, but this decrease changed to a more progressive and smooth one as the degree of modification increased, being almost inappreciable in CP40. Contrarily, the melting point in samples CP20 and CP40 was evidenced by a sharp drop as the crystalline structure approached the melting point. Both transition temperatures (T_g and T_m) obtained from DMTA were in accordance with those obtained from DSC and shown in Table 2.2.

DMTA experiments were also performed in the oriented samples, and the results can be seen in Figure 2.6. As a general trend, in the oriented samples, the thermomechanical behaviour became less evident and defined, and it was difficult to detect the transition zones at high temperatures, especially for CP40. When comparing the peak of the loss modulus (and $\tan\delta$ peak) of the oriented and unoriented samples, no appreciable changes were evidenced in T_g for sample CP20 (Figure 2.6a) with only a slight decrease in the height of the $\tan\delta$ peak for the oriented peak. On the contrary, for sample CP40 (Figure 2.6b) a change seemed to appear in the temperatures of the loss modulus and the $\tan\delta$ peaks, and in the shape of the curve one could observe a decrease in T_g , but the curves looked wider and less defined. The melting temperature also seemed to decrease in both samples but the signal was difficult to detect and no proven conclusions could be obtained.

2.3.4 Dielectric thermal analysis (DETA)

The dielectric relaxation spectra of unoriented and oriented modified copolymers CP20 and CP40, and the unmodified CP0, were obtained in terms of the real and imaginary parts of the complex dielectric permittivity and the loss tangent angle. Figure 2.7 plots the isochronal curves of all these properties as a function of the temperature range (123 to 383 K), respectively, for a frequency of 10 Hz. The dielectric relaxation spectrum of these copolymers is much more complex than the mechanical spectrum. At least three Havriliak–Negami functions related to intra or inter-molecular motions were observed.

The dielectric spectra of the unmodified copolymer (CP0) are composed of four dielectric relaxations, as shown in Figure 2.7. More precisely, two dielectric relaxations were located at low temperatures and two relaxations were located at mid to high temperatures, in an increasing temperature order. The first dielectric relaxation appeared in the range of 123 K to 173 K at a frequency of 10 Hz. At these low temperatures, the molecular arrangements are of intramolecular origin, and only local modes of

mobility can be attributed as the origin of this relaxation. In this case, this relaxation can be assigned to local motions in the amorphous part of the PEO segments [41].

A second dielectric relaxation occurred between 163 K and 223 K at a frequency of 10 Hz. This is a very complex zone that other authors have attributed to the overlapping of two types of motions. One is the γ' relaxation, which is similar to the γ , but it occurs in the amorphous zone, hindered by the lamellae that are part of the crystalline domains [41]. In our case, as the work previously referenced, the γ' relaxation appears to be overlapped with the β relaxation. Though no clear evidence of crystallinity was found for CP0, a certain local order cannot be ruled out. Therefore, one can postulate the existence of amorphous zones but with restricted mobility, the relaxation of which can be evidenced by the higher sensitivity of DETA. The other relaxation is attributed to the cooperative motion of the amorphous region of the PEO segments. For this reason, this relaxation could be labelled as a β relaxation because it is a cooperative movement but of only one part of the copolymer, or an α_{PEO} relaxation to define exactly the nature of the molecular movement.

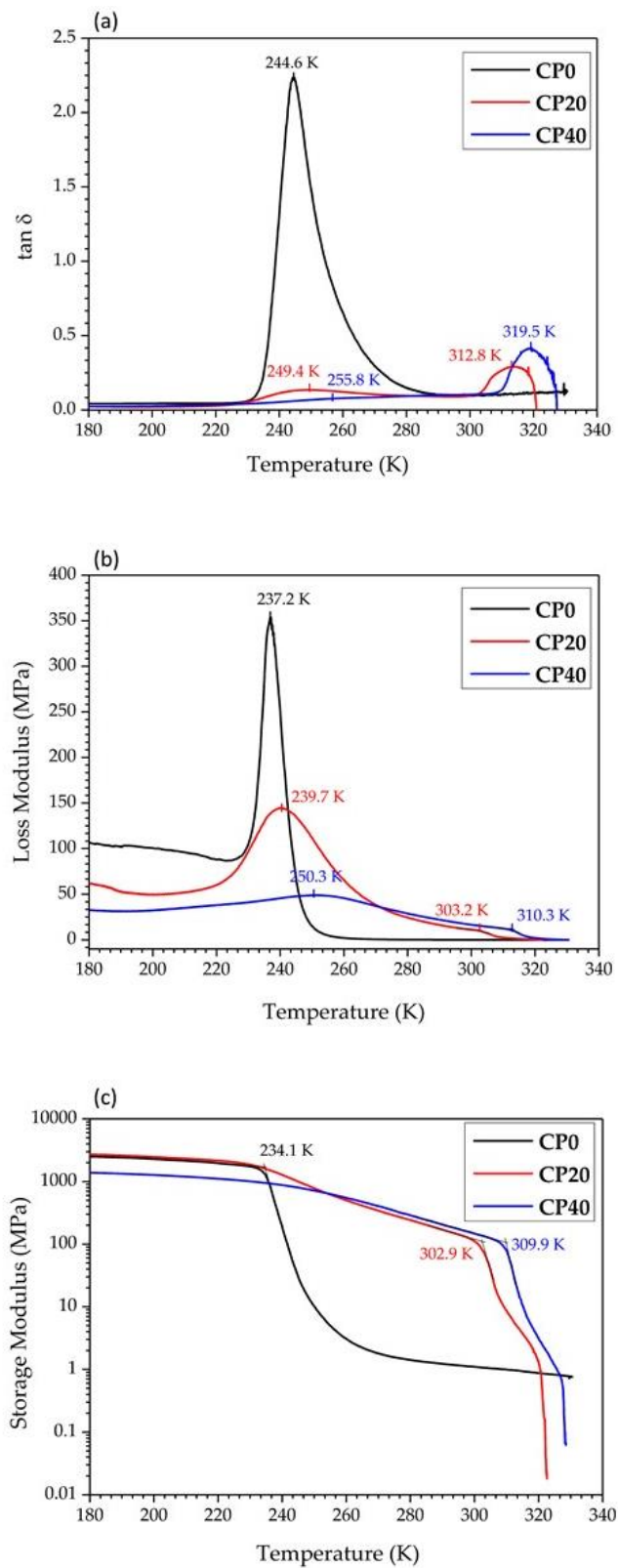


Figure 2.5 DMTA analysis for CP0, CP20 and CP40 samples. (a) $\tan \delta$ (b) loss modulus and (c) storage modulus evolution with temperature.

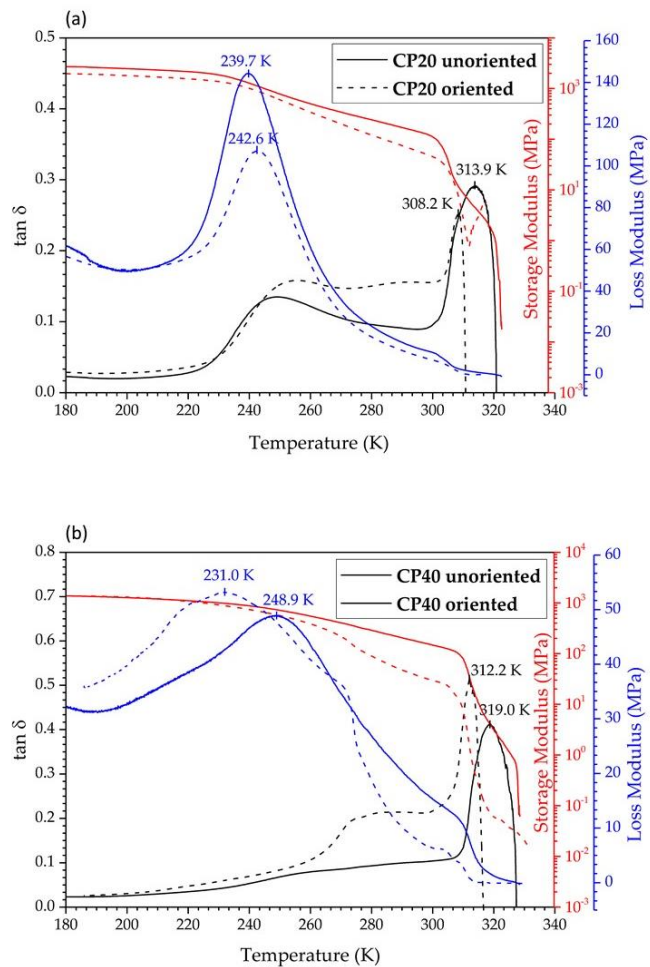


Figure 2.6 Comparison of DMTA analysis for CP20 (a) and CP40 (b) oriented and unoriented samples.

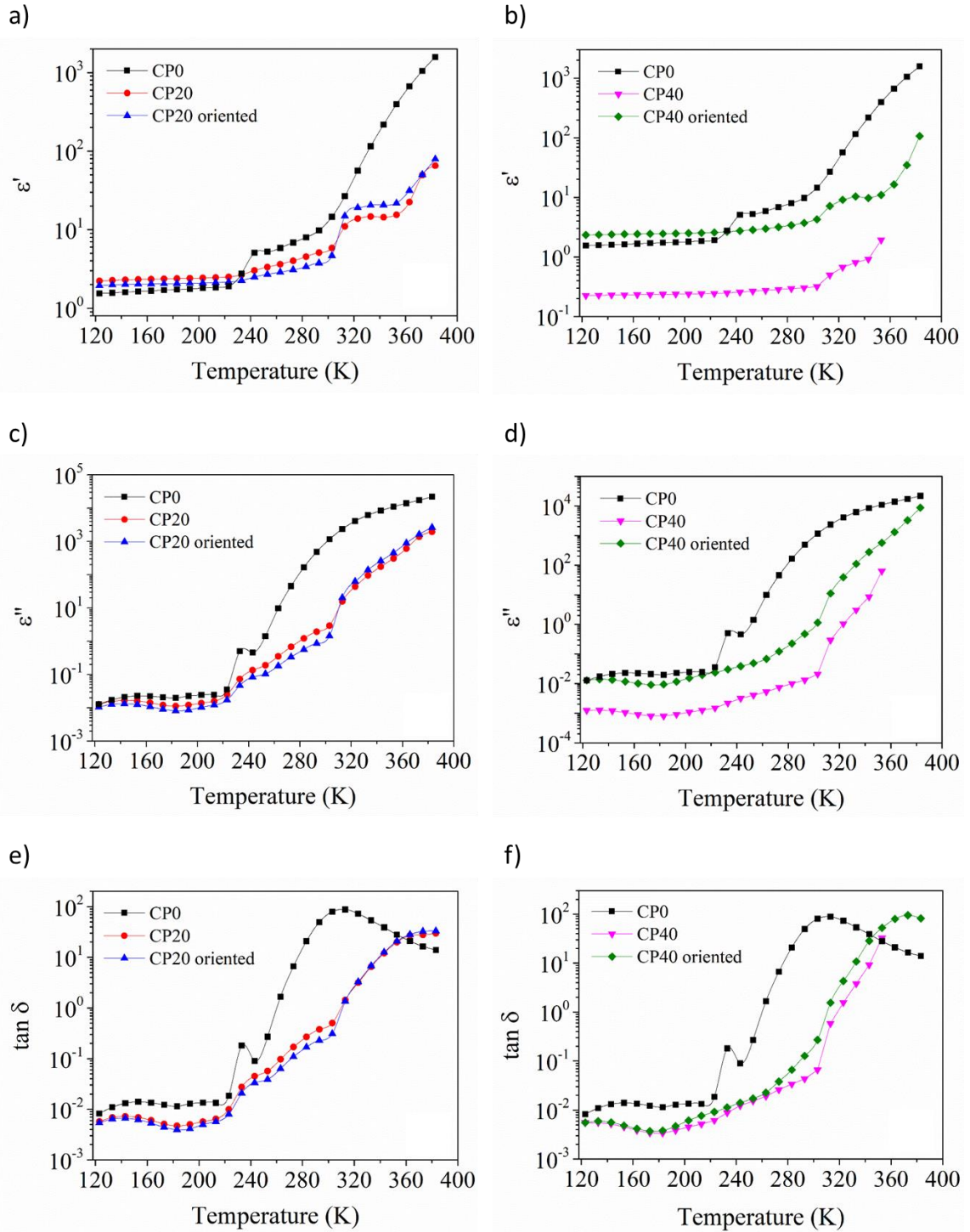


Figure 2.7 (a, b) Real part of the complex permittivity; (c, d) Imaginary part of the complex permittivity; (e, f) loss tangent of the unmodified copolymer (CP0) of the modified oriented and unoriented copolymers CP20 and CP40, respectively, for a frequency of 10 Hz.

The next molecular relaxation is found in the temperature range between 223 K and 248 K at a frequency of 10 Hz. As other researchers have discussed, this dielectric relaxation is attributed to the

cooperative motion of the PECH segments, which would already affect the whole main chain. Thus, this relaxation was considered as the glass transition T_g , and therefore it is called the α relaxation [28,29,42,43]. This peak would be related to the maximum found in the spectrum of mechanical relaxations in the same temperature range.

Additionally, between 253 K to 383K another dielectric relaxation was found, whose maximum peak value was found at 323 K at a frequency of 10 Hz. The temperature at which this relaxation appears fully coincides with the values observed by Silva et al. for the crystallization peak followed by the melting of PECH-co-EO [43]. These authors suggest that the crystalline phase is probably formed by the organization of the ethylene oxide blocks present in the copolymer structure. Therefore, this relaxation can be attributed to a molecular motion that promoted the melting transition.

Figure 2.7 also shows the dielectric spectra of the copolymers CP20 and CP40, which are composed of four molecular relaxations. However, not all of them have the same molecular origin as those of CP0.

At the lowest temperature, from 123 K to 173 K at a frequency of 10 Hz, a relaxation appears. Note that this relaxation appears at lower temperatures than the γ relaxation found in CP0. These results are in accordance with the molecular mobility found, for instance, in the dielectric spectra of PECH40 and PECH80 [29], as well as in the PAZE100 and PAZE40 [28]. Thus, this relaxation can be ascribed to an intramolecular motion related to the benzyloxy terminal group of the dendrimer side groups.

The second relaxation, from 163 K to 223 K at a frequency of 10 Hz, coincided with the molecular arrangements observed in the copolymer (COP0) in the same temperature interval. Therefore, it was related to the motion of the PEO segments. The intensity of this relaxation was lower since the dendritic chains hindered this motion. Figure 2.8 displays a comparison between the dielectric spectra of the oriented and unoriented CP20 and CP40, respectively. The orientation process did not produce any significant variation in the dielectric spectra of either copolymer, regardless of the number of dendronized units. Indeed, the same molecular mobility was observed, and only slight shifts towards higher temperatures were found. This is to be expected due to the high level of restrictions imposed by the orientation process. The trend observed in the dielectrical plots (Figure 2.8a,b) is similar to that observed in DMTA results (Figure 2.6a,b). There are no appreciable differences between the unoriented and oriented CP20 samples which both present similar shapes in the evolution of the $\tan\delta$. Contrarily, for the oriented sample CP40, the $\tan\delta$ curve slightly differed from its unoriented counterpart and presented a shape more undefined, with no significant changes in the slope, and without a clear peak in the transition zone, as was also observed in the DMTA curves.

The third relaxation, as Figure 2.7 indicates, from 223 K to 273 K at a frequency of 10 Hz, is attributed to the glass transition of the copolymers. The intensity of this relaxation decreased progressively

going from CP20 to CP40, which is in agreement with the increase of cristallinity consequent to the side modification of the copolymer.

Finally, in the same Figure 2.7, the last broad relaxation at temperatures higher than 348 K at a frequency of 10 Hz corresponded to two overlapping processes, i.e., the melting of the copolymer main chain (initial segment of the transition) and the clearing (end segment of the transition) of the copolymer liquid crystalline phase.

It is possible to assume that the differences observed between the different copolymers in this higher temperature range were mainly due to the melting process. Figure 2.8 shows that, at lower temperatures there are differences between the copolymers due to their different degree of cristallinity. Therefore, these differences also appear during the melting process and are more evident in the case of CP40.

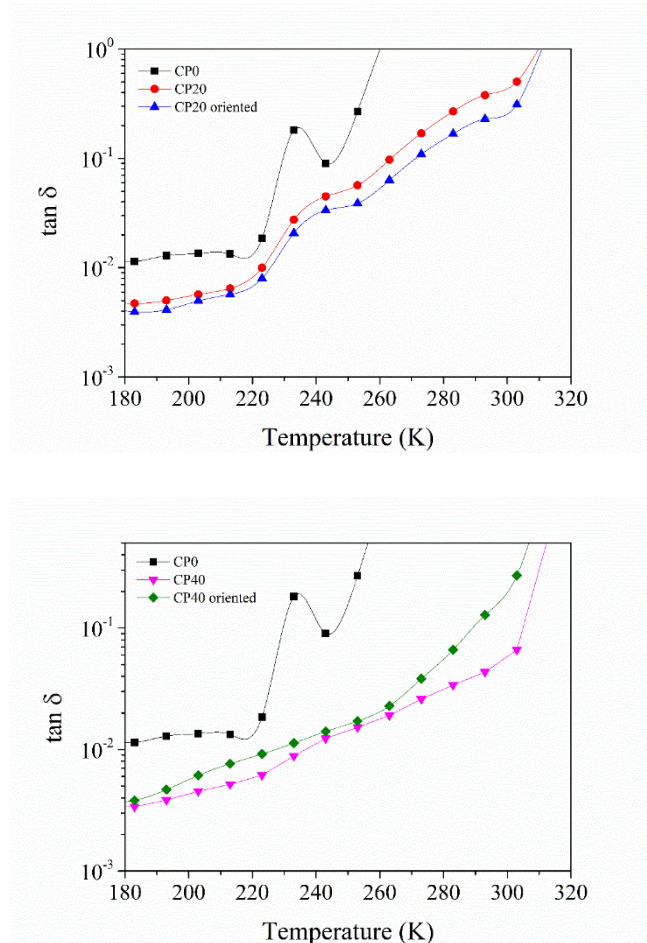


Figure 2.8 Tan δ of the unmodified (COP0), modified oriented and unoriented copolymers CP20 (Top) and CP40 (Bottom), respectively, for a frequency of 10 Hz.

2.4 Conclusions

PECH-co-EO was modified with the Dendron 3,4,5-tris[4-(n-dodecan-1-yloxy)benzyloxy] benzoate (Tap), at two different extents, producing two copolymers with 20% (CP20) and 40% (CP40) dendronized repetitive units, respectively. Both copolymers exhibited a liquid crystalline columnar mesophase. Moreover, the presence of the Dendron induced a partial crystallization of the main chain with respect to the unmodified PECH-co-EO (CP0), probably involving the ethylene oxide units. Membranes were prepared out of these copolymers, and a proper orientation of the columnar channels was achieved by means of a thermal treatment. A fine-tuning of this procedure revealed that the cooling rate and the annealing temperature were crucial parameters to obtain the highest homeotropic orientation.

Copolymer mobility was investigated by DMTA and DETA in both the unoriented and oriented membranes. Mechanical tests evidenced that grafting with the dendron strongly hindered copolymer motions, as expected, such that the higher the modification degree, the higher the degree of crystallinity, T_g and melting temperature; that is, the copolymer needed more thermal energy for the main chain to become mobile and dissipate energy. A DETA analysis showed four molecular relaxations in both the unmodified and modified copolymers, although some of them had different origins. In the case of CP0, the unmodified copolymer, we could distinguish local motions of the amorphous PEO portions and relaxations of chain portions with somewhat restricted mobility, the glass transition, and finally a molecular motion that promoted the melting transition. On the other hand, CP20 and CP40 showed an intramolecular motion related to the benzyloxy terminal group of the dendrimer side groups, and another relaxation related to the motion of the PEO segments, which had lower intensity than in CP0, which we attributed to the presence of the dendritic moieties. At higher temperature, we could distinguish the glass transition and the partially overlapped main chain melting and liquid crystalline phase clearing. The analysis of the dielectric spectra of these copolymers was quite complex and intriguing. Therefore, it will be deepened in a forthcoming paper.

Neither DMTA nor DETA evidenced great differences between the unoriented and oriented membranes, regardless of the quantity of dendrons. Indeed, we observed the same molecular mobility and slight shifts towards higher temperatures as expected, on the basis of the restrictions imposed by the orientation process.

The differences in the modification degree of the copolymers through the introduced crystallinity and modified molecular mobility will surely affect their performances as membranes. Therefore, in part 2 of this paper we report on the membrane characterization and their transport properties.

2.5 References

1. Vorländer, D. Research on molecular shape with the aid of crystalline fluids. *Zeitschrift für Phys. Chemie--Stoichiometrie und Verwandtschaftslehre* 1923, 105, 211-254.
2. Lyu, X.; Xiao, A.; Shi, D.; Li, Y.; Shen, Z.; Chen, E.Q.; Zheng, S.; Fan, X.H.; Zhou, Q.F. Liquid crystalline polymers: Discovery, development, and the future. *Polymer* 2020, 202, 122740, doi:doi:10.1016/j.polymer.2020.122740.
3. Kato, T.; Uchida, J.; Ichikawa, T.; Soberats, B. Functional liquid-crystalline polymers and supramolecular liquid crystals. *Polym. J.* 2018, 50, 149-166, doi:doi:10.1038/pj.2017.55.
4. Shibaev, V. *Liquid Crystalline Polymers. Basic Concepts and Polymer Properties* 2012, 1, 259-285.
5. Kato, T.; Gupta, M.; Yamaguchi, D.; Gan, K.P.; Nakayama, M. Supramolecular association and nanostructure formation of liquid crystals and polymers for new functional materials. *Bull. Chem. Soc. Jpn.* 2021, 94, 357-376, doi: doi:10.1246/BCSJ.20200304.
6. Vicari, L. *Optical applications of liquid crystals.* 2010.
7. Bustamante, E.A.S.; Haase, W. Synthesis and characterization of new liquid crystalline monomers for non-linear optics. X-ray study of re-entrant nematic behaviour with smectic-like fluctuations of C-type. *Liq. Cryst.* 1997, 23, 603-612, doi:doi:10.1080/026782997208217.
8. Shih, H.F.; Wu, D.Y.; Tien, C.L.; Dai, C.L. Optical compensator with switchable modes using polymer stabilized liquid crystals. *Opt. Rev.* 2013, 20, 218-223, doi:doi:10.1007/s10043-013-0039-9.
9. Funahashi, M. Development of liquid-crystalline semiconductors with high carrier mobilities and their application to thin-film transistors. *Polym. J.* 2009, 41, 459-469, doi:doi:10.1295/polymj.PJ2008324.
10. Sakuda, J.; Hosono, E.; Yoshio, M.; Ichikawa, T.; Matsumoto, T.; Ohno, H.; Zhou, H.; Kato, T. Liquid-crystalline electrolytes for lithium-ion batteries: Ordered assemblies of a mesogen-containing carbonate and a lithium salt. *Adv. Funct. Mater.* 2015, 25, 1206-1212, doi:doi:10.1002/adfm.201402509.

11. Gin, D.L.; Noble, R.D. Designing the next generation of chemical separation membranes. 2011, 332, 674-676, doi:doi:10.1126/science.1203771.
12. Rahman, S.N.A.; Masdar, M.S.; Rosli, M.I.; Majlan, E.H.; Husaini, T.; Kamarudin, S.K.; Daud, W.R.W. Overview biohydrogen technologies and application in fuel cell technology. *Renew. Sustain. Energy Rev.* 2016, 66, 137-162, doi:doi:10.1016/j.rser.2016.07.047.
13. Sazali, N.; Salleh, W.N.W.; Jamaludin, A.S.; Razali, M.N.M. New perspectives on fuel cell technology: A brief review. *Membranes (Basel)* 2020, 10, 99, doi:doi:10.3390/membranes10050099.
14. Yoshio, M.; Kato, T. Liquid Crystals as Ion Conductors. In *Handbook of Liquid Crystals*, Goodby, J.W., Collings, P.J., Kato, T., Tschierske, C., Gleeson, H., Eds.; Wiley-VCH: Weinheim (Germany), 2012; pp. 727-749.
15. Boden, N. Micellar Liquid Crystals. In *Micelles, Membranes, Microemulsions, and Monolayers*, Gelbart, W.M., Ben-Shaul, A., Eds.; Springer New York: New York, NY, 1994; pp. 153-217.
16. Strzelecka, T.E.; Davidson, M.W.; Rill, R.L. Multiple liquid crystal phases of DNA at high concentrations. *Nature* 1988, 331, 457-460, doi:doi:10.1038/331457a0.
17. Percec, V.; Heck, J. Liquid crystalline polymers containing mesogenic units based on half-disc and rod-like moieties - 4. Side chain liquid crystalline polymethylsiloxanes containing hemiphasmidic mesogens based on 4-[3,4,5-tri-(alkan-1-yloxy)benzoate]biphenyl groups. *J. Polym. Sci. Part A Polym. Chem.* 1991, 29, 591-597, doi:doi:10.1002/pola.1991.080290416.
18. Sun, H.J.; Zhang, S.; Percec, V. From structure to function via complex supramolecular dendrimer systems. *Chem. Soc. Rev.* 2015, 44, 3900-3923, doi:doi:10.1039/c4cs00249k.
19. Bhosale, S.V.; Rasool, M.A.; Reina, J.A.; Giamberini, M. New Liquid crystalline Columnar Poly(epichlorohydrin-co-ethylene oxide) Derivatives Leading to Biomimetic Ion Channels. *Polymer Engineering and Science* 2013, 53, 159-167.
20. Šakalytė, A.; Reina, J.A.; Giamberini, M. Liquid Crystalline Polyamines Containing Side Dendrons: To-ward the Building of Ion Channels Based on Polyamines. *Polymer (Guildf)* 2013, 54, 5133-5140.
21. Montané, X.; Bhosale, S.V.; Reina, J.A.; Giamberini, M. Columnar Liquid Crystalline Polyglycidol Derivatives: A Novel Alternative for Proton-Conducting Membranes. *Polymer (Guildf)* 2015, 66, 100-109.

22. Montané, X.; Bogdanowicz, K.A.; Colace, G.; Reina, J.A.; Cerruti, P.; Lederer, A.; Giamberini, M. Advances in the Design of Self-Supported Ion-Conducting Membranes-New Family of Columnar Liquid Crystalline Polyamines. Part 1: Copolymer Synthesis and Membrane Preparation. *Polymer (Guildf)* 2016, 105, 298–309.
23. Bogdanowicz, K.A.; Bhosale, S.V.; Li, Y.; Vankelecom, I.F.J.; Garcia-Valls, R.; Reina, J.A.; Giamberini, M. Mimicking Nature: Biomimetic Ionic Channels. *J. Membr. Sci.* 2016, 509, 10–18.
24. Bogdanowicz, K.A.; Sístat, P.; Reina, J.A.; Giamberini, M. Liquid Crystalline Polymeric Wires for Selective Proton Transport, Part 2: Ion Transport in Solid-State. *Polymer (Guildf)* 2016, 92, 58–65.
25. Montané, X.; Bogdanowicz, K.A.; Prats-Reig, J.; Colace, G.; Reina, J.A.; Giamberini, M. Advances in the Design of Self-Supported Ion-Conducting Membranes – New Family of Columnar Liquid Crystalline Polyamines. Part 2: Ion Transport Characterisation and Comparison to Hybrid Membranes. *Polymer (Guildf)* 2016, 105, 234–242.
26. Wang, T.; Li, X.; Dong, Z.; Huang, S.; Yu, H. Vertical Orientation of Nanocylinders in Liquid-Crystalline Block Copolymers Directed by Light. *ACS Appl. Mater. Interfaces* 2017, 9, 24864–24872, doi:doi:10.1021/acsami.7b06086.
27. Bogdanowicz, K.A.; Rapsilber, G.A.; Reina, J.A.; Giamberini, M. Liquid Crystalline Polymeric Wires for Selective Proton Transport, Part 1: Wires Preparation. *Polymer (Guildf)* 2016, 92, 50–57.
28. R. Teruel-Juanes; Bogdanowicz, K.A.; Badia, J.D.; Juano-Arbona, V.S.d.S.d.; Graf, R.; Reina, J.A.; Giamberini, M.; Ribes-Greus, A. Molecular Mobility in Oriented and Unoriented Membranes Based on Poly[2-(Aziridin-1-yl)ethanol]. *Polymers* 2021, 13, 1060, doi: <https://doi.org/10.3390/polym13071060>.
29. Teruel-Juanes, R.; Pascual-Jose, B.; Graf, R.; Reina, J.A.; Giamberini, M.; Ribes-Greus, A. Effect of Dendritic Side Groups on the Mobility of Modified Poly(epichlorohydrin) Copolymers. *Polymers* 2021, 13, 1961.
30. Percec, V.; Glodde, M.; Bera, T.K.; Miura, Y.; Shiyanovskaya, I.; Singer, K.D.; Balagurusamy, V.S.K.; Heiney, P.A.; Schnell, I.; Rapp, A.; et al. Self-organization of supramolecular helical dendrimers into complex electronic materials. *Nature* 2002, 417, 384–387.
31. Charlesworth, J.M. Deconvolution of overlapping relaxations in dynamic mechanical spectra. *J. Mater. Sci.* 1993, 28, 399–404, doi: <https://doi.org/10.1007/BF00357816>.

32. Havriliak, S.; Negami, S. A complex plane analysis of α -dispersions in some polymer systems. *J. Polym. Sci. Part C Polym. Symp.* 1966, 14, 99–117, doi:<https://doi.org/10.1002/polc.5070140111>.
33. Havriliak, S.; Negami, S. A complex plane representation of dielectric and mechanical relaxation processes in some polymers. *Polymer (Guildf)* 1967, 8, 161–210, doi:[https://doi.org/10.1016/0032-3861\(67\)90021-3](https://doi.org/10.1016/0032-3861(67)90021-3).
34. Jin, X.; Zhang, S.; Runt, J. Broadband Dielectric Investigation of Amorphous Poly (methyl methacrylate)/Poly (ethylene oxide) Blends. *Macromolecules* 2004, 37, 8110-8115.
35. Tong, Y.; Lin, Y.; Wang, S.; Song, M. A study of crystallisation of poly (ethylene oxide) and polypropylene on graphene surface. *Polymer* 2015, 73, 52-61.
36. Buckley, C.P.; Kovacs, A.J. Melting behaviour of low molecular weight poly (ethylene-oxide) fractions. *Prog. Colloid. Polym. Sci.* 1975, 58, 44-52.
37. Reina, J.A.; Serra, A.; Mantecón, A.; Cádiz, V. Thermosets obtained by chemical modification of epichlorohydrin-ethylene oxide copolymer and their crosslinking through double bonds. *Journal of Polymer Science: Part A: Polymer Chemistry* 1995, 33, 941-948.
38. Ronda, J.C.; Reina, J.A.; Cádiz, V.; Giamberini, M.; Nicolais, L. Self-organized Liquid-crystalline Poly-ethers Obtained by Grafting Tapered Mesogenic Groups onto Poly (Epichlorohydrin): Toward Biomimetic Ion Channels. *J. Polym. Sci. Part A Polym. Chem.* 2003, 41, 2918–2929.
39. Ronda, J.C.; Reina, J.A.; Giamberini, M. Self-organized Liquid-crystalline Polyethers Obtained by Grafting Tapered Mesogenic Groups onto Poly (Epichlorohydrin): Toward Biomimetic Ion Channels 2. *J. Polym. Sci. Part A Polym. Chem.* 2004, 42, 326–340.
40. Komura, M.; Yoshitake, A.; Komiyama, H.; Iyoda, T. Control of Air-Interface-Induced Perpendicular Nanocylinder Orientation in Liquid Crystal Block Copolymer Films by a Surface-Covering Method. *Macromolecules* 2015, 48, 672-678.
41. Jin, X.; Zhang, S.; Runt, J. Observation of a fast dielectric relaxation in semi-crystalline poly(ethylene oxide). *Polymer (Guildf)* 2002, 43, 6247-6254, doi:[https://doi.org/10.1016/S0032-3861\(02\)00560-8](https://doi.org/10.1016/S0032-3861(02)00560-8).
42. Alegría, A.; Elizetxea, C.; Cendoya, I.; Colmenero, J. Anomalous Dynamical Homogeneity of the Dielectric α -Relaxation in Miscible Polymer Blends of Poly(epichlorohydrin) and Poly(vinyl methyl ether). *Macromolecules* 1995, 28, 8819-8823, doi:<https://doi.org/10.1021/ma00130a014>.

43. Silva, M.A.; De Paoli, M.-A.; Felisberti, M.I. Flory-Huggins interaction parameter of poly (ethylene oxide)/poly (epichlorohydrin) and poly (ethylene oxide)/poly (epichlorohydrin-co-ethylene oxide) blends. *Polymer* 1998, 39, 2551-2556.



Chapter 3.

Membranes for cation transport based on dendronized Poly (epichlorohydrin-co-ethylene oxide). Part 2: membrane characterization and transport properties

UNIVERSITAT ROVIRA I VIRGILI
NOVEL POLYMERIC MEMBRANES FOR ARTIFICIAL PHOTOSYNTHESIS
Alireza Zare

3.1 Introduction

During the last decades, the interest in finding more sustainable and respectful methods for generating energy such as artificial photosynthesis and electrochemical energy storage systems has greatly attracted the scientific community [1-5]. Proton conducting membranes are one of the most important components in both energy systems taking into account their roles: separation of the two compartments and conduct selectively the protons from anode to cathode [6]. On the other hand, the design of proton-conducting membranes should also take into account how to avoid the permeation of active species. For example, in direct-methanol fuel cell and flow battery systems, the membrane must have a low permeability/crossover rate toward active methanol and metallic species [7,8].

Within the wide variety of materials that have been developed in the design of proton-conducting membranes, the synthesis of polymers capable for transport cations by mimicking the phenomena of ion transport that take place in biological membranes [9] was explored in the last decades.

In this direction, Percec et al. carried out an extensive investigation on the synthesis and subsequent self-assembly process of supramolecular dendrons, dendrimers, and dendronized polymers into columnar liquid-crystalline (LC) mesophases [10,11]. As a result, the intramolecular self-assembly process induces a helical conformation of the polymer backbones of these polymers, which are encircled by hydrophobic dendrons, providing to these materials the ability to transport cations in a selective manner, just as it happens in complex biological membranes [12,13].

The design of side-chain liquid-crystalline polyethers and polyamines that can work as ion transport channels due to the self-assembling of their polymeric columns, a process that is induced by the exo-recognition of the side-chain dendrons 3,4,5-tris[4-(n-dodecan-1-yloxy)bezyloxy]benzoate (Tap), is a topic which has been widely investigated by our research group [14-17]. The resulting self-organized structures shows the complexity of its molecular design [16], which might be of value, for instance, for fuel cell applications. Additionally, membranes in which the polymer columns were homeotropically oriented have been prepared with the previously synthesized low molecular weight side-chain liquid-crystalline polymers (SCLCPs), which also showed proton transport results similar to those of Nafion® when they were tested as proton transport membranes [16,18-20]. However, in some cases the prepared membranes were brittle and exhibited poor mechanical properties, drawbacks that can be partially minimized by the preparation of hybrid membranes [18,19] or by using dendronized polymers with higher molecular weights such as Polyepichlorhydrin or Poly(epichlorhydrin-co-ethylene-oxide) (PECH-co-EO) [21]. Some of the most important factors that must be considered in the design of membranes that have the potential to transport cations are:

- The chemical composition of the polymer backbone, emphasizing which type of electron-withdrawing atom is present in polymer main chains.
- The amount of grafted mesogenic groups into the polymer backbone.
- The method (or combined methods) employed to favor the homeotropic alignment of the polymeric columns (thermal or light treatment, shearing, spinning) [22].

Among all of them, we have recently focused on studying the relationship between the orientation of distinct SCLCPs according to their degree of modification with Tap dendrons [23,24]. Furthermore, the analysis of how different parameters involved in the annealing process (annealing temperature, annealing time, and cooling rate) of the membranes prepared with dendronized Poly(epichlorohydrin-co-ethylene oxide) that present 20% and 40% of grafted Tap dendrons have been deeply studied in Part 1 of this paper, entitled: “Membranes for cation transport based on dendronized Poly(epichlorohydrin-coethylene oxide). Part 1: The effect of the Dendron amount and column orientation on the copolymer mobility” [25]. In that study, PECH-co-EO PECH-co-EO units were chemically modified with Tap, and copolymers with different modification degrees of Tap were synthesized. The chemical structure of PECH-co-EO (CP0) and the copolymers modified with 20% (CP20) and 40% (CP40) of Tap, which are used for the preparation of membranes, are depicted in Figure 3.1a. Moreover, the resulting structure of the homeotropically oriented PECH-co-EO columns modified with Tap are shown in Figure 3.1b.

As reported, the decrease in the cooling rate results in an improvement in the orientation of the polymeric columns perpendicular to the membrane surface. Nonetheless, the most relevant factor is the selection of the annealing temperature, which should be as close as possible to the clearing temperature (T_c) determined by differential scanning calorimetry (DSC) since a higher mobility of the copolymer structure is favored when the temperature is increased. Moreover, this study showed that the orientation method produces an increment of the crystalline fractions and the melting temperature (T_m) of these SCLCPs. Even though the analysis of all these properties is crucial, the assessment of the membranes in transport systems will allow for evaluating their efficacy in applications related to proton transport. Thus, the preparation and characterization of membranes derived from two side-chain liquid crystalline copolyethers that differ in the amount of Tap side-chain dendrons (20 and 40%, respectively) have been carried out in present work. According to Part 1 of this paper, membranes were exposed to a thermal treatment that induces the self-assemble of the polymer chains into columnar structures. In this sense, the main goal of this study is to investigate how the presence of two different amounts of grafted dendrons can affect the transport capacity of oriented membranes by means of methanol and proton permeability, together with linear sweep voltammetry (LSV) analysis. The results obtained were compared with the commercial membrane Nafion 117. Moreover, other properties such as the wettability, the morphology, and the topography of unoriented

and oriented membranes have been examined; in this way, one can understand the evolution of the self assembly process that occurs in these ionic channels and the final organization of the polymeric columns, for the purpose of optimizing the design of membranes, and obtain good performance in operative conditions.

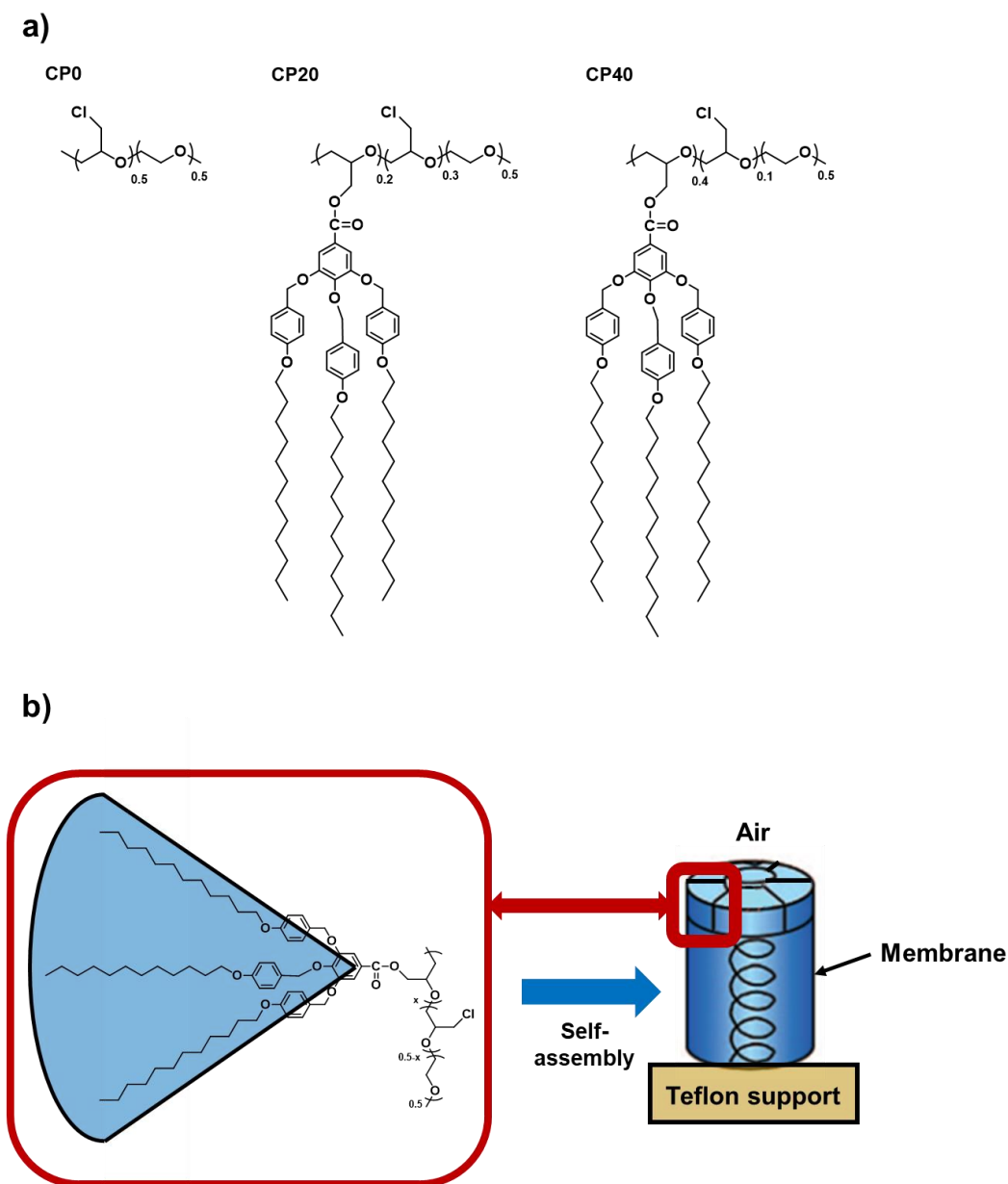


Figure 3.1 a) Chemical structure of: CP0 (unmodified PECH-co-EO), CP20 (PECH-co-EO modified with 20% Tap dendron), and CP40 (PECH-co-EO modified with 40% Tap dendron). b) Homeotropic alignment of the liquid-crystalline columns of the polymer to the membrane surface.

3.2 Materials and Methods

3.2.1 Materials

Inorganic and organic compounds were purchased from Sigma Aldrich (Sigma Aldrich Química, Madrid, Spain) and Fisher Scientifics (Fisher Scientific Spain, Madrid, Spain) and used as received. All the solvents were purchased from Scharlab (Scharlab, S.L., Barcelona, Spain). Potassium 3,4,5-tris[4-(n-dodecan-1-yloxy)bezyloxy]benzoate (Tap) was synthesized according to the previous report [16]. Poly(epichlorohydrin-co-ethylene oxide) (P(ECH-co-EO) 1:1, $M_w = 5.01 \times 10^5$, $M_n = 1.08 \times 10^5$ determined by gel permeation chromatography) was purchased from Sigma-Aldrich and used as received. The Nafion® 117 membrane from DuPont was provided by Fuel Cell Etc (College Station, Texas, USA) and cleaned before using [26]. For the cleaning treatment of Nafion, the following steps were performed; the membrane was washed in a hydrogen peroxide aqueous solution 5% for 1h at 80°C to removes residual impurities. Then, the membrane was washed in sulfuric acid solution 0.5M for 1h at 80°C. The membrane was put in boiling deionized water for 1 hour to remove the remaining impurities. Finally, the membrane was immersed in a container of H₂O₂ 3% for 1.5h at 80°C, deionized water for 1h at 80°C, H₂SO₄ 0.5M for 1h at 80°C and washed in deionized water for 1h at 80°C, respectively. Before experiments, the membrane was kept in deionized water at room temperature.

The chemical modification of P(ECH-co-EO) was performed as described in Part 1 [25]. In the present paper, we focused our attention on the polymer modified at 20 and 40%, which are labelled as CP20 and CP40. On the other hand, the unmodified PECH-co-EO was labelled as CP0.

3.2.2 Membrane preparation and characterizations

Membranes were prepared by immersion precipitation method. The modified copolymer was dissolved in THF (30% w/w). After that, the homogeneous solution was casted by a casting machine (K-paint applicator, RK Paintcoat Instruments Ltd., Litlington, UK) on a FEP (Fluorinated Ethylene Propylene) sheet support with a controlled thickness (gap size 300 µm). Then, the support including the wet film on top was immersed in a bath of Milli-Q water in which the polymeric membrane was formed with an asymmetric structure. After 24 h, the formed membrane was dried overnight at room temperature. Additionally, the membranes were vacuum dried at room temperature 48 h before weighing.

The thickness of membranes was measured using a micrometer with a sensitivity of 2 µm. The measurements were carried out at various points, and the membranes were found to have constant thickness.

To achieve homeotropically oriented structure of modified copolymer, the polymeric membrane (approx. 2 cm diameter) was placed on a hot stage (Linkam TP92, Linkam Scientific Instruments Ltd.,

Tadworth, UK) for the *baking* process, described as follows. For annealing, membranes were heated up to 140 °C. They were kept at the same temperature for 30 minutes. Then they were slowly cooled (0.1 °C/min) to 107°C where they were kept for 120 h. Finally, the membranes were allowed to cool to room temperature at 10°C/min. Finally, the uniform membranes were left at room temperature for 1h and then detached from FEP support. For scale-up, the same procedure was performed in a Hewlett Packard 5890 Series II Gas Chromatograph oven (Hewlett Packard, Palo Alto, USA).

The static contact angles of water drops on both membrane surfaces were measured by Dataphysics OCA 15EC (DataPhysics, Fildertstadt, Germany). The contact angle was measured immediately after placing the water drop (3 µL) on the membrane surface and the contact angle was calculated from a digital image by SCA software included in the apparatus; for each test reported, at least three drops of water were used.

Water uptake of membranes was calculated according to the Eq. (1) through immersing dry membranes into deionized water at room temperature for 72h. Membrane were weighed before and after immersing in water.

$$\text{Water uptake (\%)} = \frac{W_{\text{wet}} - W_{\text{dry}}}{W_{\text{dry}}} \times 100 \quad (1)$$

W_{wet} and W_{dry} refer to the weights of the wet and dry membranes respectively.

The AFM images were recorded with an Agilent 5500 Environmental Atomic Force Microscope (Agilent Technology, Santa Clara, USA) equipped with an extender electronics module, which enables phase imaging in a Tapping Mode. All images were recorded in a tapping mode using 75 Al-G Budget sensor (freq. 71 kHz) silicon cantilever (thickness = 3 µm) with a force constant at 3 N/m and a resonance frequency of 71 kHz. The scan rate was typically 0.7–2 Hz. All images (1 µm × 1 µm) were measured at room temperature, in unfiltered air. The microscope was placed on an active vibration isolation chamber (Agilent Technology), which was further placed on a large sturdy table to eliminate external vibration noise. The Nanotec WSxM 5.0 Develop 9.1 Image Browser Scanning Probe Microscopy²³ (Julio Gómez Herrero & José María Gómez Rodríguez) was used for the roughness analysis of the images [27]. RMS roughness and kurtosis were calculated out of the AFM images of five different regions for each sample.

Field Emission Scanning Electron Microscopy (FESEM) was performed by means of Scios2 microscope (Thermo Fisher Scientific, Waltham, USA). Electrons were accelerated at 5.00 kV, the working distance was comprised between 3 and 7 mm and ETD or T2- high resolution secondary electrons detectors were used. Membranes were previously cryofractured in liquid nitrogen in order to observe their cross sections.

The methanol permeability was measured using a permeability cell, which included two compartments (feed and stripping, respectively) that were connected through the membrane. The effective membrane area was 0.86 cm². The feed and the stripping volumes were 200 mL, which were filled up with 2 M methanol solution (feed compartment) and milli-Q water (stripping compartment), respectively. After 24, 48, 96 and 168 h, the methanol content was determined by means of a Hewlett Packard 6890 Series Gas Chromatograph (Hewlett Packard, Palo Alto, USA), J&W DB-624 GC Column, 25 m, 0.20 mm, 1.12 μm, 7 inch cage (Agilent Technology, Santa Clara, USA) and He as flowing gas. Results were interpolated from a standard curve obtained from previous experiments: $A_m/A_{iso} = 0.3458 C_m/C_{iso} + 0.033$ ($R^2 = 0.9992$), where A_m is the area corresponding to the methanol peak and A_{iso} is the area of the isopropanol peak which was used as an internal standard in 0.05 M concentration; C_m and C_{iso} are the methanol and the constant isopropanol molar concentrations, respectively. The calibration line was obtained by using 22 points with a methanol concentration ranging between 0.01 and 0.7 M. All samples were analysed in triplicate. The detection limit was calculated according to [28] and was found as 0.0879, which corresponds to a methanol concentration equal to 4.4×10^{-3} M.

Proton permeability was performed using a Teflon set-up that comprised two compartments, the feed and stripping solutions, separated by the tested membrane. Samples for these measurements were placed between two compartments giving a total membrane area equal to 0.66 cm². The solution volume in each compartment was 200 mL. The measurements were carried out in the ambient temperature (approx. 25 °C). The pH of the stripping solution was measured every 10 s by an Orion 4 Star PH/ISE Multimeter (Thermo Fisher Scientific, Waltham, MA, USA). For the proton transport experiments, the initial feed solution was 0.1 M HCl aqueous solution and the stripping solution 0.1 M aqueous solution of the corresponding salt: LiCl, NaCl or KCl. The calculations of the methanol and proton permeability were carried out in accordance with the following equations..

The permeability coefficient, p (cm s⁻¹), can be described by the equation [29]:

$$-\ln \frac{C_f}{C_0} = \frac{Ap}{V_f} t \quad (2)$$

where C_0 (mol l⁻¹) is the initial concentration of the feed solution and C_f (mol L⁻¹) is the feed concentration calculated from the stripping solution at time t (s):

$$C_f = C_0 - C_s \quad (3)$$

V_f is the feed volume (mL) and A is the actual membrane area (cm²).

Under steady-state conditions, proton flux was calculated by Fick's First Law:

$$J = \frac{P\Delta C}{l} \quad (4)$$

where l (cm) is the membrane thickness and ΔC is the difference in concentration between the initial feed solution and the final stripping solution. In our experimental conditions, C_0 was much greater than the final stripping concentration, so we considered $\Delta C \approx C_0$.

The permeability P ($\text{cm}^2 \text{s}^{-1}$) is defined as:

$$P = pl \quad (5)$$

The flux is then related to the permeability coefficient as:

$$J = pC_0 \quad (6)$$

In the case of proton, data were fitted according to Equation (1) in the time range 15–120 h.

Linear sweep voltammetry was performed according to [19] using Autolab PGstat204 in potentiostatic mode with current ranging from 100 mA to 100 μA , potential range from 0 V to 5 V, step 0.01 V and scan rate 0.0013 V s^{-1} . The experimental set-up for linear sweep voltammetry measurements is shown in Figure 3.S1. The distance between the membrane and reference electrodes (Ag/AgCl) was 1.13 cm. The sample was placed in a Teflon frame with a hole giving a total membrane area equal 0.5 cm^2 . The measurements were performed at the ambient temperature. The solution volume in each compartment was 200 mL. One series of measurements was applied to one membrane including HCl, LiCl, NaCl and KCl, respectively. An experiment for each specific cation includes five consecutive current-voltage measurements at different time frames: 5, 10, 20, 40 and 60 min.

3.3 Results

In this study, in order to elucidate how the Tap amount affects the final material characteristics, we focused our attention on the copolymers modified at 20% (CP20) and 40% (CP40), respectively. Their characteristics were compared with the unmodified copolymer CP0. Nafion 117 was also used as a reference for proton transport properties.

3.3.1 Morphological characterization, wettability and water uptake

In Part 1 of this paper [25], we showed that grafting of Poly(epichlorohydrin-coethylene oxide) with Tap group, induced crystallization of the copolymer main chain, and that this effect was more evident in the copolymer-based oriented membranes. Crystallinity calculated from DSC data lay around 30% in the

unoriented samples, whereas it increased to 38% in oriented CP20 and to 52% in oriented CP40. It has to be remembered that the orientation corresponds to the homeotropic alignment of the liquid crystalline columns to the membrane surface. Therefore, the microstructure of these materials can be expected quite complex, since crystalline, liquid crystalline, and amorphous regions coexist

Figure 3.2 shows the AFM topographic images of CP20 unoriented (a) and oriented (b), of CP40 unoriented (c) and oriented (d).

From the 3-dimensional topographic images, we can see that the surface of unoriented CP20 (Figure 3.2a) exhibits protruding bundles, with apparent diameter around 100 nm, surrounded by small flat areas; after orientation (Figure 3.2b), extreme flattening of the surface is observed. As for CP40, on the surface of the unoriented sample (Figure 3.2c), one can see more extended flat areas; after orientation (Figure 3.2d), the material clearly re-organizes and small grains appear. A small granular structure was found within and outside the dendritic regions of semi-crystalline PEO and amorphous polymethylmethacrylate (PMMA) phase-separated blends [30].

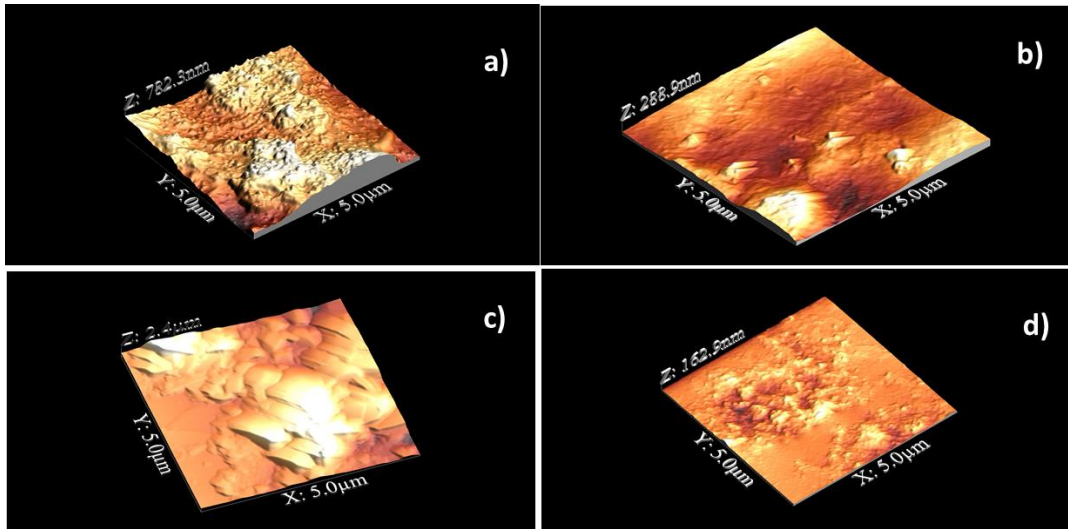


Figure 3.2 Topographic 3-D images of CP20 unoriented (a) and oriented (b), of CP40 unoriented (c) and oriented (d). Scanned area: $5 \mu\text{m} \times 5 \mu\text{m}$.

Table 3.1 shows RMS roughness and kurtosis for CP20 and CP40, as calculated from five AFM images for each sample.

Table 3.1 RMS roughness and kurtosis from AFM images for CP20 and CP40 samples.

Sample	RMS roughness (μm)	Kurtosis
CP20	128 ± 26	3.6 ± 1.3
CP20 oriented	44 ± 11	4.6 ± 1.6
CP40	0.44 ± 0.08	2.7 ± 0.1
CP40 oriented	16 ± 3	4.8 ± 1.1

As shown in Table 3.1, in the case of CP20, orientation determines a considerable decrease of RMS roughness, which is the standard deviation of height; the opposite is found for CP40, though the average RMS value of its oriented sample remains lower than oriented CP20. Kurtosis, which illustrates the sharpness of the surface height distribution, increases for both samples upon orientation i.e. peaks predominate over the valleys: this effect is more pronounced for CP40, where we pass from a mesokurtic surface (unoriented sample), to a leptokurtic one (oriented sample). Kurtosis values larger than 3.0 generally indicate a surface with almost quantized height values.

Membrane wettability was determined by water Contact Angle (CA) measurements. The experiments were performed on unoriented samples, as well as on membranes oriented by thermal treatment, as previously described. In addition, CA was determined both on the side in direct contact with the FEP support and on the air side. Results are depicted in Table 3.2.

Table 3.2 Water Contact angle values of unmodified Poly(epichlorohydrin-co-ethylene oxide) (CP0), CP20 and CP40 membranes.

Sample	Contact angle ($^{\circ}$)	
	Unoriented ^{a, b}	Oriented ^{a, b}
CP0	72 ± 1	-
CP20	87 ± 2 ^a , 89 ± 1 ^b	104.5 ± 0.9 ^a , 106.5 ± 0.4 ^b
CP40	96.3 ± 0.3 ^a , 97.0 ± 0.5 ^b	131.0 ± 0.8 ^a , 129.8 ± 0.3 ^b

^a Air side; ^b Teflon side

Unmodified CP0 showed hydrophilic behavior, as expected based on its chemical structure, which contains polar ether linkages. Unoriented CP20 exhibited higher CA values on both sides, though they were still lower than 90° , i.e. the presence of the dendron decreased somewhat the hydrophilic character of the copolymer; differently, unoriented CP40, with higher amount of Tap group, exhibited hydrophobic behavior on both sides. Upon orientation, both dendronized copolymers showed water CA higher than 90° , i.e., clearly had hydrophobic surfaces, and no substantial difference was found between the air and Teflon side. One has to consider that two effects contribute to wettability: the former is the chemical composition of the material, which can be more or less affine to water; the latter is the surface morphology, i.e. its roughness. Given the same chemical composition, the effect of a roughened surface is to magnify the

wetting properties of the membrane. Therefore, if one considers a water-repelling material, it will be more strongly so, the rougher the surface [31]. In our previous studies on dendronized copolymer-based membranes, we found that thermal orientation induced an increase in water CA, and we attributed this evidence to the dendron exposure on the membrane surface in the oriented material, since it constitutes the hydrophobic portion of the copolymer. This was considered as an indirect evidence of the fact that the dendron anchoring to the air surface drives the orientation [21]. In the case of CP40, apart from this effect, one should also take into account that there is a strong increase of roughness in the oriented sample, which, together with the higher number of dendrons possibly exposed to the surface, contributes to greatly enhance hydrophobicity.

The wettability change of CP20 and CP40 on orientation also reflects on the water uptake (WU) after 72 hours. The results of these measurements are shown in Table 3.3.

Table 3.3 Water uptake (%) after 72 hours, and methanol permeability after 168 hours, of unmodified Poly(epichlorohydrin-co-ethylene oxide) (CP0), CP20 and CP40 membranes.

Sample	WU (%), Unoriented	WU (%), Oriented	Methanol Permeability ($\text{cm}^2 \text{s}^{-1}$)
CP0	28	-	1.79×10^{-6}
CP20	10 ± 0.5	2.5 ± 0.5	Not Detected
CP40	7.5 ± 0.5	2.0 ± 0.5	Not Detected

As expected, the WU of CP0 after 72 hours has a considerable value (Table 3.3). Chemical modification with the Tap group remarkably decreases the WU of both CP20 and CP40, probably due to two factors, i.e. the presence of the hydrophobic, aromatic and aliphatic groups in the grafted moiety, as well as the induced crystallinity in the main chain. Actually, it has been demonstrated for many polymers that crystallinity hinders moisture sorption [32,33]. After orientation, water uptake is further reduced to very low values, which is in line with the wettability decrease (Table 3.2) and the increase of crystallinity. As for methanol permeability, in the case of CP0, methanol could be detected in the stripping compartment during the permeability experiment, and gave a permeability equal to $1.79 \times 10^{-6} \text{ cm}^2 \text{ s}^{-1}$. Nevertheless, in the case of oriented CP20 and CP40, even after 168 hours the methanol concentration in the stripping compartment was below the detection limit [28], i.e., it was lower than $4.4 \times 10^{-3} \text{ M}$. Therefore, the characteristics of dendronized CP20 and CP40 could also offer advantages as far as methanol crossover in Direct Methanol Fuel Cells (DMFCs) is concerned.

Water contact angle was also determined on oriented CP20 and CP40 membranes after water uptake and proton permeability tests, which results are reported in Table 3.S1. In general, no significant changes were observed (Table 3.S1), except for CP40, which water contact angle was slightly reduced after the proton permeability test; however remaining characteristic of a clearly hydrophobic surface.

We also attempted the characterization of CP0, CP20, and CP40 by FESEM. Unfortunately, in the case of CP0 and CP20, strong damage was provoked to the samples by the radiation under the applied conditions. Essentially, the acquisition of information on soft matter insulators, such as polymers, can be a difficult task, due to sample charging and radiation damage. This drawback has been traditionally overcome by coating the polymer with a thin conductive layer, but this strategy masks tiny surface details [34]. Therefore, in the case of CP0, CP20 unoriented and CP20 oriented, we could not reach magnification higher than 800 in the experimental conditions used. Figure 3.S2 shows the cross section images of CP0 (a), CP20 (b) and CP20 oriented (c). Operating in this conditions, just allowed to get a global image of the cross-section of CP0 and CP20. In the case of CP0, the cross-section appeared quite smooth and somewhat folded (Figure 3.S2a); however, much rougher and heterogenous cross-section could be distinguished in unoriented CP20 (Figure 3.S2b). Orientation of CP20 seemed to produce a more homogeneous cross-section (Figure 3.S2c).

On the other hand, intriguing results were obtained when FESEM analysis was performed on CP40 unoriented and oriented samples. In this case, the working distance could be lowered to about 3 mm and we could obtain magnification as high as 350k, thus revealing higher resistance of these samples to radiation damage.

Figure 3.3 depicts FESEM images of CP40 (a) and CP40 oriented (b) membrane cross-sections.

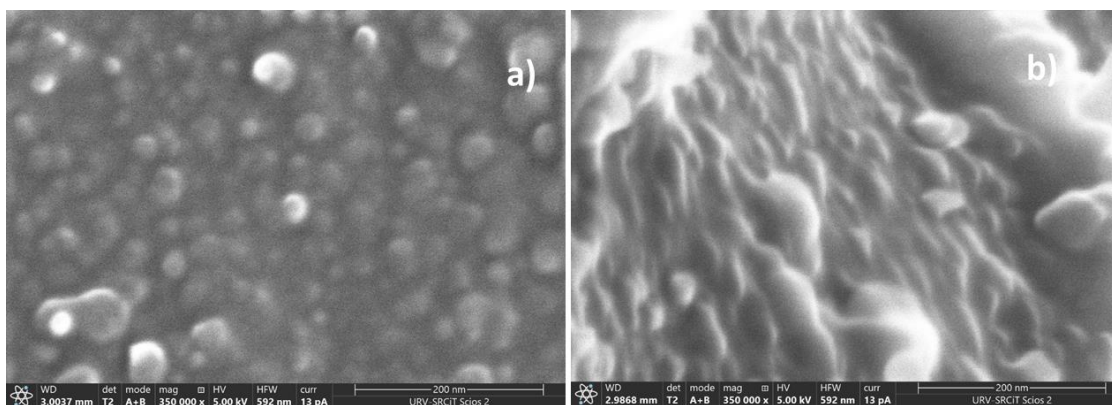


Figure 3.3 FESEM images of membrane cross-sections of: CP40 (a) and CP40 oriented (b).

The cross section of CP40 exhibits spherical particles, with diameters ranging between 20 and 50 nm (Figure 3.4). The particles look more elongated in the case of the oriented sample, resembling cylindrical aggregates with diameters comprised approximately between 7 and 40 nm. Particularly interesting is the image of the scratched surface of CP40 oriented membrane (Figure 3.4), where bundles with diameters ranging around 50 nm can be clearly seen.

These bundles can be related to the “ionic cables” formed by aggregates of oriented columns, and responsible for the ionic transport, which existence was suggested also by TEM observations performed on dendronized poly(epichlorohydrin) [21].

3.3.2 Transport properties

In general, ionic transport in membranes occurs through the system of channels and pores, which size depends on the nature of polymer and hydration degree. The transport of ions in the narrow channels is responsible for limiting ionic conductivity: therefore, narrow channels are usually called the “bottle neck” [35]. In a previous paper, we investigated the proton and sodium transport mechanism of oriented membranes based on P(ECH-co-EO), modified at 36% with the same dendron Tap, by in situ Raman spectroscopy coupled with amperometric experiment [36]. We found that the polyether backbone is mainly involved in both cation transport, in agreement with our previous hypotheses. Moreover, in the case of proton, conduction also occurs through an additional coordination site which lies on the lateral ester group that actively interacts with protons during their transport. The investigated membranes exhibited water uptake as low as $4\pm 1\%$; in addition, in Raman spectra, the range characteristic of OH stretching of water showed no significant changes. Therefore, we concluded that cation transport in these membranes is not significantly influenced by the presence of water.

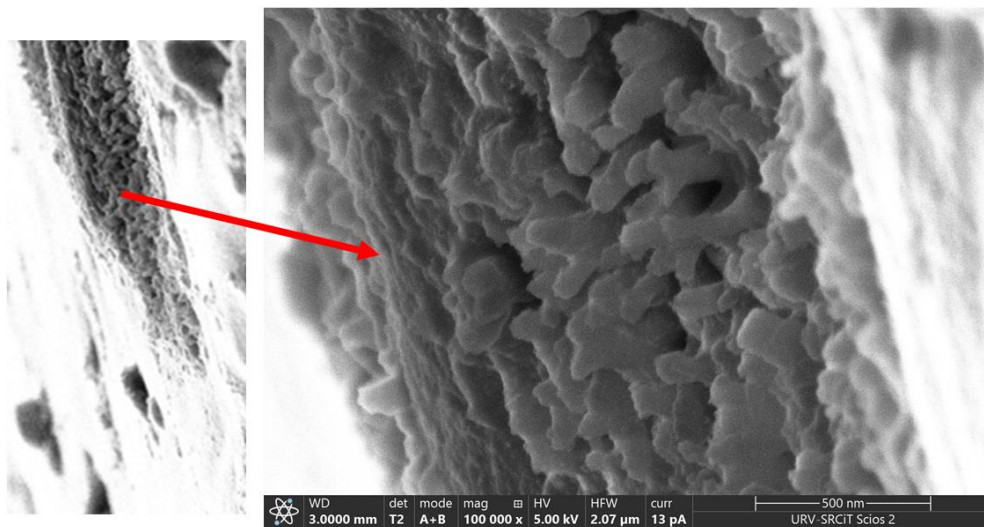


Figure 3.4 FESEM image of the scratched surface of CP40 oriented membrane. Left: membrane surface with scratched portion; Right: zoom of the scratched area.

Table 3.4 shows the proton permeability of CP0, CP20, and CP40 in the presence of different cations in the stripping compartment. For sake of comparison, proton permeability was also determined for Nafion 117 in the presence of NaCl in the stripping compartment.

Table 3.4 Proton permeabilities of CP0, CP20, and CP40 in the presence of different cations in the stripping compartment.

Sample	Proton Permeability (cm ² s ⁻¹)		
	Cation in stripping phase		
	Li ⁺	Na ⁺	K ⁺
CP0	$(2.7 \pm 0.2) \times 10^{-6}$	$(3.4 \pm 1.6) \times 10^{-6}$	$(2.2 \pm 0.1) \times 10^{-5}$
CP20	$(1.2 \pm 0.3) \times 10^{-8}$	$(3.1 \pm 0.5) \times 10^{-8}$	Not detected
CP40	$(1.4 \pm 0.2) \times 10^{-7}$	$(3.4 \pm 0.5) \times 10^{-7}$	Not detected
Nafion 117	-	$(7.7 \pm 0.2) \times 10^{-6}$	-

In our previous papers, we already made the hypothesis of a cation antiport mechanism [29] in the case of dendronized columnar copolymers, which seemed to be confirmed by the agreement between the proton concentration increase in the stripping solution and the simultaneous sodium concentration increase in the feed solution, when the permeability experiment was performed with this species in the stripping compartment [37]. The coupled Raman-LSV studies performed on CP modified at 36% [36] also gave an inside into the possibility of conducting cations via antiport mechanism. It was observed that only protons can be transported via both the main chain and the lateral ester groups, whereas sodium ions only by interaction with the main chain. Having those findings in mind, the antiport transport in similar system could take place even within a single channel where the proton would by-pass the bigger cation transported in opposite direction, through an ester lateral group. Additionally, proton transport in proton permeability experiments should be generally limited by the stripping cation permeability which, in the case of CP20 and CP40, is expected to depend on the size of the polyether ion channel. In addition, we have to take into account that CP20 and CP40 are partially crystalline [25], which also contributes to limit cation permeability. Differently, in the case of CP0 and Nafion 117, transport is expected to occur through the channels formed by hydration of the respective membranes: Actually, they exhibited comparable proton permeabilities, around 10^{-6} cm² s⁻¹, in the experiment where the stripping phase contained Na⁺. In the case of this experiment, considerably lower values were found for proton permeability of CP20 and CP40, which were comparable to the ones found for poly(epichlorohydrine) 72% modified with the same dendron [21].

No proton permeability at all could be detected for CP20 and CP40 when the stripping compartment contained KCl, suggesting that this cation is too big for the transport to occur through the oriented channels. On the other hand, in all cases, lower proton permeability values were calculated when Li⁺ was contained in the stripping phase, despite its lower crystallographic radius, which might seem anomalous. Essentially, one should remember that Li⁺ exhibit peculiar features with respect to other alkaline cations: Li⁺ possesses a very high hydration number, which determines the highest hydrated radius of the considered series and the weakest electrostatic interactions [38]. In addition, it was found that the diffusion coefficient of Li⁺ in

cation-exchange membranes strongly depends on the water content [39]. Therefore, limited Li^+ transport through CP20 and CP40 membranes could be due to a combination of the membrane low affinity to water as well as to the big size of the hydrated cation. Moreover, it has been generally found that in cation-exchange membranes, the cation diffusion coefficients and ionic conductivity increase in the sequence $\text{Li}^+ < \text{Na}^+$ [40]; in general, the cation diffusion coefficients increase the alkaline metal atomic mass, due to higher water mobility and lower effective radius of the hydrated cation.

When membranes containing hydrated non-specific channels are considered, the charge balance is assured by the parallel diffusion of cations and anions, though anions are characterized by smaller mobility. Nevertheless, it has been found that, in the case of electrolytes transferred to an acid filled compartment in a permeability experiment, the charge balance is reached mainly by a mutual diffusion of protons and alkali metal ions, though a parallel diffusion of cations and anions exist [41]. Given the higher diffusion of the cations, the contribution of anion diffusion can be neglected; therefore, proton permeability depends on the co-ion mobility. Additionally, we need to take into consideration the water swelling of the membrane and the hydrophilic nature of the used materials. These two factors can significantly affect the ionic transport giving a misguided impression of an actual ionic transport. As a result of the membrane swelling, undefined channels filled with absorbed water are formed, similarly to those in Nafion. In this scenario, cation flow is restricted in very small range only by the quantity of the absorbed water and the channel structure. This could justify the trend of proton permeabilities found for CP0, where no specific columnar ionic channels exist.

In order to characterize the ionic transport in terms of selectivity, linear sweep voltammetry (LSV) measurements were performed. Our previous studies [19,20,36] confirmed that the linear sweep voltammetry is a suitable tool to study transport through the nonionomeric membranes. Differently from the permeability test, the ionic transport measured in a setup for LSV allows cation transport in one direction. For the experiment, 0.1 M solutions of hydrochloric acid and different monovalent chlorides were used to establish the selectivity of used membranes. For most cases of CP-based membranes, the three-region division of the LSV curve was not evident and the I-V curves have a linear tendency. Only in the case of CP40 and 0.1M NaCl solution the ohmic, limiting current, and overlimiting regions were observed (see Figure 3.5). This fact confirms the permselective nature of CP20 and CP40, what was expected based on results obtained for CP copolymer modified in 36% [36]. Permselectivity of membranes indicates that ionic transport occurs only via cation flux.

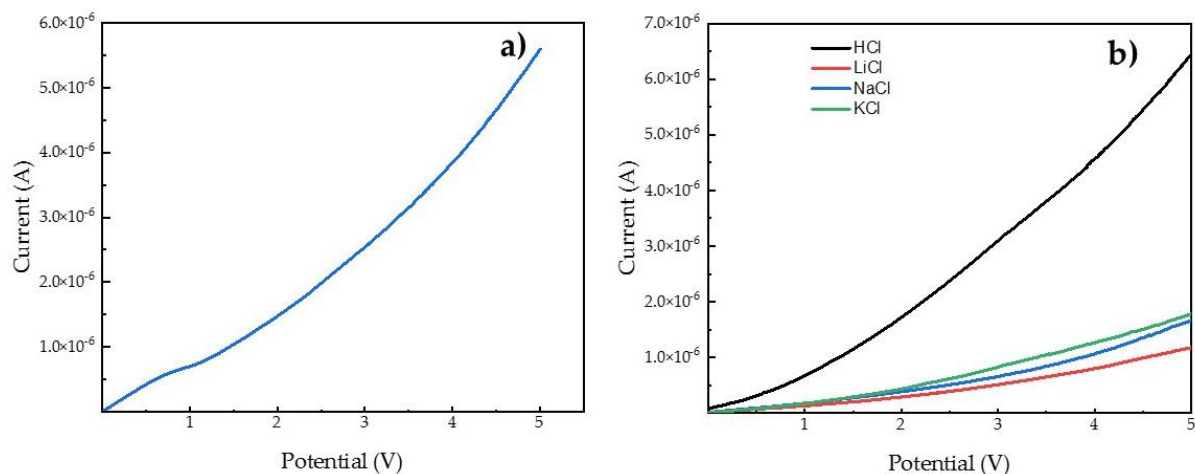


Figure 3.5 Linear sweep voltammetry curve of CP40 and 0.1M NaCl as electrolyte (a) and example of curves for different monovalent cations for CP20 (b).

Table 3.5 summarizes the data obtained from the LSV experiments. As can be seen from the resistance value per membrane's area, an increasing order was observed, giving a $CP0 < CP40 < CP20$ order for the different membranes. It aligns very well with the tendency observed in permeability test. This fact confirms that the one direction conductivity of cations depends on the effective cavity of the channel, also for the LSV experiments. In order to describe a selectivity of used membranes, a selectivity factor was calculated as the ratio between conductance (inverse resistance) for specific alkali cation and conductance of proton $\times 100$. Therefore, the higher the selectivity factor, the lower the selectivity of the membrane toward the proton, with respect to the considered cation. It was noticed that the order for the selectivity factor was as follows: $Na^+ > K^+ > Li^+$ for CP0 and CP20 and $K^+ > Na^+ > Li^+$ for CP40. The information coming from the selectivity order of cationic transport gives an idea of the channel size. It seems that the cavity of ionic channels for CP20 is more likely to fit the sodium cation than other tested cations, whereas in the case of CP40, the conduction of potassium was greater than for other alkali cations; this suggests that the greater modification degree of the copolymer causes the formation of channels with larger diameter. When compared with Nafion 117 membrane and to CP0, where the ionic transport is affected by the presence of water and the channel structure is not well defined, the selectivity between different cations depends on ionic forces in the case of ionomeric Nafion 117, or by hydration radius, as described in the section regarding the permeability test.

Table 3.5 A summary of data obtained from LSV experiments.

Sample name	Thickness (μm)	Electrolyte	Resistance ($\text{k}\Omega/\text{cm}^2$)	Selectivity (%)
Nafion	200	HCl	0.03	-
		LiCl	0.16	16.5
		NaCl	0.11	24.2
		KCl	0.08	31.0
CP0	360	HCl	863.9	-
		LiCl	1470.59	58,7
		NaCl	1108.65	77,8
		KCl	1175.78	73,5
CP20	150	HCl	3333.33	-
		LiCl	16260.16	20.5
		NaCl	12269.94	27.2
		KCl	12578.62	26.5
CP40	200	HCl	1492.54	-
		LiCl	8230.45	19.4
		NaCl	2597.40	51.3
		KCl	2564.10	57.4

3.4 Conclusions

Membranes derived from two side-chain liquid crystalline copolyethers, differing in the amount of Tap side-chain dendrons (20 and 40%, respectively) have been prepared and characterized in terms of morphology, wettability, water uptake, methanol permeability, and transport properties. Proper orientation of these membranes was achieved by means of a thermal treatment, and the morphological characterization was carried out on both the unoriented and oriented samples as well as on the unmodified copolyether. In general, AFM showed that orientation leads to a decrease in roughness for CP20 and an increase for CP40, the latter being much less rough in any case; in both samples, hydrophobicity increased with membrane orientation. Water uptake was considerably lower than found for the unmodified copolyether, being furtherly reduced on orientation; in both grafted copolymers, no methanol permeability was detected at all. FESEM analysis showed bundles with diameters ranging around 50 nm in the cross-section of the oriented CP40 sample; unfortunately, experiments with similar magnification could not be performed on CP20 nor CP0, because of sample charging and radiation damage. The permeability test for the oriented CP20 and CP40 demonstrated an evident tendency related to the presence of defined cationic channels not affected by water presence. The higher modified polymer CP40 showed better permeability results, probably as an effect of the better inner structure of channels across the entire structure, due to a greater number of Tap groups supporting the column. Linear sweep voltammetric studies confirmed the permselective nature of the new membranes, meaning the ionic transport occurs only via cation transport across the membrane. The

best cationic performance was observed in the case of proton and then for sodium/potassium and lithium cations.

3.5 References

1. Berardi, S.; Drouet, S.; Francàs, L.; Gimbert-Suriñach, C.; Guttentag, M.; Richmond, C.; Stoll, T.; Llobet, A. Molecular artificial photosynthesis. *Chemical Society Reviews* 2014, 43, 7501-7519, doi:10.1039/c3cs60405e.
2. Keijer, T.; Bouwens, T.; Hessels, J.; Reek, Joost N.H. Supramolecular strategies in artificial photosynthesis. *Chemical Science* 2021, 12, 50-70, doi:10.1039/d0sc03715j.
3. Cheng, Y.Y.; Fückel, B.; MacQueen, R.W.; Khoury, T.; Clady, R.G.; Schulze, T.F.; Ekins-Daukes, N.; Crossley, M.J.; Stannowski, B.; Lips, K. Improving the light-harvesting of amorphous silicon solar cells with photochemical upconversion. *Energy & Environmental Science* 2012, 5, 6953-6959.
4. Sazali, N.; Wan Salleh, W.N.; Jamaludin, A.S.; Mhd Razali, M.N. New Perspectives on Fuel Cell Technology: A Brief Review. *Membranes* 2020, 10, 99.
5. Zhang, H.; Sun, C. Cost-effective iron-based aqueous redox flow batteries for large-scale energy storage application: A review. *Journal of Power Sources* 2021, 493, 229445.
6. Shin, D.W.; Guiver, M.D.; Lee, Y.M. Hydrocarbon-Based Polymer Electrolyte Membranes: Importance of Morphology on Ion Transport and Membrane Stability. *Chem. Rev.* 2017, 117, 4759-4805, doi:10.1021/acs.chemrev.6b00586.
7. Sun, C.; Negro, E.; Nale, A.; Pagot, G.; Vezzù, K.; Zawodzinski, T.A.; Meda, L.; Gambaro, C.; Di Noto, V. An efficient barrier toward vanadium crossover in redox flow batteries: The bilayer [Nafion/(WO₃)_x] hybrid inorganic-organic membrane. *Electrochimica acta* 2021, 378, 138133, doi:10.1016/j.electacta.2021.138133.
8. Parthiban, V.; Akula, S.; Sahu, A.K. Surfactant templated nanoporous carbon-Nafion hybrid membranes for direct methanol fuel cells with reduced methanol crossover. *Journal of Membrane Science* 2017, 541, 127-136, doi:<https://doi.org/10.1016/j.memsci.2017.06.081>.
9. Shen, Y.X.; Saboe, P.O.; Sines, I.T.; Erbakan, M.; Kumar, M. Biomimetic membranes: A review. *Journal of Membrane Science*, 2014, 454, 359-381, doi:<https://doi.org/10.1016/j.memsci.2013.12.019>.
10. Percec, V.; Heck, J. Liquid crystalline polymers containing mesogenic units based on half-disc and rod-like moieties - 4. Side chain liquid crystalline polymethylsiloxanes containing hemiphasmidic

- mesogens based on 4-[3,4,5-tri-(alkan-1-yloxy)benzoate]biphenyl groups. *J. Polym. Sci. Part A Polym. Chem.* 1991, 29, 591-597, doi:doi:10.1002/pola.1991.080290416.
11. Sun, H.-J.; Zhang, S.; Percec, V. From structure to function via complex supramolecular dendrimer systems. *Chemical Society Reviews* 2015, 44, 3900-3923, doi:10.1039/c4cs00249k.
 12. Rosen, B.M.; ., C.J.W.; Wilson, D.A.; Peterca, M.; Imam, M.R.; Percec, V. Dendron-mediated self-assembly, disassembly, and self-organization of complex systems. *Chem. Rev.* 2009, 109, 6275-6540, doi:10.1021/cr900157q.
 13. Sherman, S.E.; Xiao, Q.; Percec, V. Mimicking complex biological membranes and their programmable glycan ligands with dendrimersomes and glycodendrimersomes. *Chem. Rev.* 2017, 117, 6538-6631, doi:10.1021/acs.chemrev.7b00097.
 14. Bhosale, S.V.; Rasool, M.A.; Reina, J.A.; Giamberini, M. New Liquid crystalline Columnar Poly(epichlorohydrin-co-ethylene oxide) Derivatives Leading to Biomimetic Ion Channels. *Polymer Engineering and Science* 2013, 53, 159-167.
 15. Montané, X.; Bhosale, S.V.; Reina, J.A.; Giamberini, M. Columnar Liquid Crystalline Polyglycidol Derivatives: A Novel Alternative for Proton-Conducting Membranes. *Polymer (Guildf)* 2015, 66, 100-109.
 16. Montané, X.; Bogdanowicz, K.A.; Colace, G.; Reina, J.A.; Cerruti, P.; Lederer, A.; Giamberini, M. Advances in the Design of Self-Supported Ion-Conducting Membranes-New Family of Columnar Liquid Crystalline Polyamines. Part 1: Copolymer Synthesis and Membrane Preparation. *Polymer (Guildf)* 2016, 105, 298-309.
 17. Šakalytė, A.; Reina, J.A.; Giamberini, M. Liquid Crystalline Polyamines Containing Side Dendrons: To-ward the Building of Ion Channels Based on Polyamines. *Polymer (Guildf)* 2013, 54, 5133-5140.
 18. Bogdanowicz, K.A.; Rapsilber, G.A.; Reina, J.A.; Giamberini, M. Liquid Crystalline Polymeric Wires for Selective Proton Transport, Part 1: Wires Preparation. *Polymer (Guildf)* 2016, 92, 50-57.
 19. Bogdanowicz, K.A.; Sístat, P.; Reina, J.A.; Giamberini, M. Liquid Crystalline Polymeric Wires for Selective Proton Transport, Part 2: Ion Transport in Solid-State. *Polymer (Guildf)* 2016, 92, 58-65.
 20. Montané, X.; Bogdanowicz, K.A.; Prats-Reig, J.; Colace, G.; Reina, J.A.; Giamberini, M. Advances in the Design of Self-Supported Ion-Conducting Membranes – New Family of Columnar Liquid Crystalline Polyamines. Part 2: Ion Transport Characterisation and Comparison to Hybrid Membranes. *Polymer (Guildf)* 2016, 105, 234-242.
 21. Bogdanowicz, K.A.; Bhosale, S.V.; Li, Y.; Vankelecom, I.F.J.; Garcia-Valls, R.; Reina, J.A.; Giamberini, M. Mimicking Nature: Biomimetic Ionic Channels. *J. Membr. Sci.* 2016, 509, 10-18.

22. Lee, W.J.; Kwac, L.K.; Kim, H.G.; Chang, J.-H. Thermotropic liquid crystalline copolyester fibers according to various heat treatment conditions. *Sci Rep* 2021, 11, 11654-11654, doi:10.1038/s41598-021-91212-4.
23. Teruel-Juanes, R.; Bogdanowicz, K.A.; Badía, J.D.; Sáenz de Juano-Arbona, V.; Graf, R.; Reina, J.A.; Giamberini, M.; Ribes-Greus, A. Molecular Mobility in Oriented and Unoriented Membranes Based on Poly[2-(Aziridin-1-yl)ethanol]. *Polymers* 2021, 13, 1060.
24. Teruel-Juanes, R.; Pascual-Jose, B.; Graf, R.; Reina, J.A.; Giamberini, M.; Ribes-Greus, A. Effect of Dendritic Side Groups on the Mobility of Modified Poly(epichlorohydrin) Copolymers. *Polymers* 2021, 13, 1961.
25. Zare, A.; Pascual-Jose, B.; Flor, S.D.I.; Ribes-Greus, A.; Montané, X.; Reina, J.A.; Giamberini, M. Membranes for cation transport based on dendronized Poly(epichlorohydrin-co-ethylene oxide). Part 1: the effect of the Dendron amount and column orientation on the copolymer mobility *Polymers* Submitted.
26. Prater, K.B. Polymer electrolyte fuel cells: a review of recent developments. *Journal of Power Sources* 1994, 51, 129-144, doi:[https://doi.org/10.1016/0378-7753\(94\)01934-7](https://doi.org/10.1016/0378-7753(94)01934-7).
27. Horcas, I.; Fernandez, R.; Gomez-Rodriguez, J.M.; Colchero, J.; Gomez-Herrero, J.; Baro, A.M. WSXM: A software for scanning probe microscopy and a tool for nanotechnology. *Rev. Sci. Instrum.* 2007, 78, 013705
28. Garcia-Valls, R. Nous materials en tècniques de separació d'elements lantànids: membranes polimètriques activades i materials inorgànics per a cromatografia. Departament de Química 1995, PhD thesis, <https://hdl.handle.net/10803/13267>.
29. Mulder, M. Basic principles of membrane technology. 2003.
30. Ferreiro, V.; Douglas, J.F.; Amis, E.J.; Karim, A. Phase Ordering in Blend Films of Semi-crystalline and Amorphous Polymers. *Macromol. Symp.* 2001, 167, 73-88.
31. Wenzel, R.N. Resistance of solid surfaces to wetting by water. *Ind. Eng. Chem.* 1936, 28, 988-994.
32. Scheirs, J.; Long, T.E. *Modern Polyesters: Chemistry and Technology of Polyesters and Copolyesters*, John Wiley & Sons Ltd., The Atrium, Southern Gate, Chichester. 2003.
33. Bascheka, G.; Hartwiga, G.; Zahradnikb, F. Effect of water absorption in polymers at low and high temperatures. *Polymer* 1999, 40, 3433-3441
34. Wandrol, P.; Slouf, M. Polymer imaging in SEM – charge, damage and coating free. *Microsc. Microanal.* 2017, 23, 1816-1817.
35. Yaroslavtsev, A.B.; Stenina, I.A.; ., D.V.G. Membrane materials for energy production and storage. *Pure Appl. Chem* 2020, 92, 1147-1157.

36. Bogdanowicz, K.A.; Pirone, D.; Prats-Reig, J.; Ambrogi, V.; Reina, J.A.; Giamberini, M. In Situ Raman Spectroscopy as a Tool for Structural Insight into Cation Non-Ionomeric Polymer Interactions during Ion Transport. *Polymers* 2018, 10, 416.
37. Tylkowski, B.; Castelao, N.; Giamberini, M.; Garcia-Valls, R.; Reina, J.A.; Gumí, T. The importance of orientation in proton transport of a polymer film based on an oriented self-organized columnar liquid-crystalline polyether. *Materials Science and Engineering C* 2012, 32, 105-111.
38. Cotton, F.A.; Wilkinson, G. *Advanced Inorganic Chemistry*, John Wiley & Sons, New York. 1980.
39. Garrido, L.; Pozuelo, J.; López-González, M.; Yan, G.; Fang, J.; Riande, E. Influence of the Water Content on the Diffusion Coefficients of Li⁺ and Water across Naphthalenic Based Copolyimide Cation-Exchange Membranes. *The Journal of Physical Chemistry B* 2012, 116, 11754-11766, doi:10.1021/jp3065322.
40. Volkov, V.I.; Chernyak, A.V.; Golubenko, D.V.; Tverskoy, V.A.; Lochin, G.A.; Odjigaeva, E.S.; Yaroslavtsev, A.B. Hydration and Diffusion of H, Li, Na, Cs Ions in Cation-Exchange Membranes Based on Polyethylene- and Sulfonated-Grafted Polystyrene Studied by NMR Technique and Ionic Conductivity Measurements. *Membranes* 2020, 10, 272, doi:10.3390/membranes10100272.
41. Stenina, I.A.; Sístat, P.; Rebrov, A.I.; Pourcelly, G.; Yaroslavtsev, A.B. Ion mobility in Nafion-117 membranes. *Desalination* 2004, 170, 49-57.



Chapter 4.

Polymer blends for improved CO₂ capture membranes

UNIVERSITAT ROVIRA I VIRGILI
NOVEL POLYMERIC MEMBRANES FOR ARTIFICIAL PHOTOSYNTHESIS
Alireza Zare

4.1 Introduction

Since the late nineteenth century, rapid economic growth has provoked a huge increase in energy production and consumption. Given that energy has largely depended on the use of fossil fuels, their abundant use has turned into a big concern due their adverse effects on environment, in particular, carbon dioxide emission. CO₂ emissions contributes 60% of global warming as well as the greenhouse (GHG) effect [1]. According to the Emission Database for Global Atmospheric Research, global emissions from carbon dioxide have been increasing, rising by approximately 50% in only two decades. In 2016, carbon dioxide concentration reached the record value of 402 ppm [2], which has led to an increase of global surface temperature of about 0.8°C. The intergovernmental Panel on Climate Change (IPCC) Fifth Assessment Report, issued in 2013, indicated that the temperature rise should be kept below 2°C relative to pre-industrial levels to prevent the worst effects of climate change; this inevitably encouraged a strict control of carbon dioxide emissions. To reduce CO₂ concentration in the environment, several approaches are possible: promoting energy conservation, increasing the use of low carbon fuels (hydrogen, natural gas, or nuclear power), deploying renewable energy (solar, wind, hydropower, and bio-energy), and eventually capturing and storing carbon dioxide itself. The last approach could allow the subsequent use of the captured gas as a carbon source; nevertheless, this implies that the carbon dioxide must be first captured at atmospheric pressure and storied efficiently. Current processes are based on physical or chemical solvents as well as membrane technology; recently, new hybrid processes have been developed, which combine advanced membrane techniques with an effective CO₂ absorption process in one device, called contactor [3-5]. In these compact systems, an advanced gas membrane, which helps the mass exchange process by increasing the surface area for phase contact, is present between the gas and an absorbing aqueous solution [3, 6]. This approach is inspired by natural photosynthesis, in which leaves, by means of stomata, are able to efficiently capture carbon dioxide. In the case of membrane contactors, pores act as stomata. This system offers additional advantages: it is not necessary to disperse one phase into another due to the large contact surface between the phases; it is a small modular system, which can be easily assembled and integrated in other devices. The system is not sensitive to flooding, channeling or back-mixing; it can also be operated in a wide range of flow rates.

Recently, We reported a biomimetic contactor designed as artificial stomata [7]. This device takes advantage of a polysulfone membrane in combination with a potassium hydroxide solution. Different membrane contactors, with morphologies ranging from spongy-like to open microvoids, were prepared by phase inversion precipitation and different membrane preparation parameters. The highest CO₂ absorption flux (i.e., 67.5 mmol/m²*s) was found in the case of a finge-rlike macrovoids membrane, in which CO₂ was

even higher than in natural stomata ($40 \mu\text{mol}/\text{m}^2\cdot\text{s}$). This is also the highest value reported for an artificial system.

Amines and aminic compounds have found wide application as CO_2 removing agents due to the reversible reaction between aminic groups (basic) and CO_2 (acidic). Amine carriers can be divided into unhindered and hindered. In the former case, CO_2 transport occurs *via* a zwitterion formation, which is subsequently quietly deprotonated by another amine group, producing a carbamate ion and a protonated amine. Under this mechanism, 0.5 mol carbon dioxide can be loaded per amine group [7, 8]. On the other hand, when hindered amines are considered, the presence of a bulky group directly linked to the amine determines carbamate instability. Therefore, carbon dioxide is carried as a carbonate group in the presence of water and the maximum loading in this case is one CO_2 molecule per amine group. Moreover, in the case of hindered amines, the overall reaction rate is higher [9]. For this reason, hindered amines are considered good carriers in carbon dioxide-facilitated transport membranes. Amine carriers have been reported both as mobile and fixed-site: the second option could be preferable since mobile carriers are not covalently linked to the polymeric membrane and can produce a leakage phenomenon in a relatively easy way [10]. Recently, nanocomposite membranes based on polyvinylamine (PVAm)/piperazine glycinate (PG) for CO_2 removal were reported [11], which showed high CO_2/N_2 selectivity and good CO_2 permeance. Zi Tong et al. [10] investigated several sterically hindered polyvinylamines with different degrees of steric hindrance and found significant improvement in CO_2 permeance and CO_2/N_2 selectivity in comparison with unhindered polyvinylamine.

In this paper, our aim is to increase the performance of the polysulfone membrane contactor by blending commercial PSf with a commercial, hyperbranched polyethylene imine, specifically, Lupasol G20. The presence of the basic nitrogen atoms should increase the membrane affinity for carbon dioxide, thus improving its capture and permeability with respect to PSf. On the other hand, Lupasol G20 is a water-soluble polymer; this could prevent membrane preparation from a water coagulation bath as previously described for neat PSf as well as membrane stability in contact with the storing aqueous solution. For this reason, before blending with PSf, Lupasol G20 was partially chemically modified by means of benzoyl chloride. Additionally, chemical modification of Lupasol G20 is expected to preferably occur on the the unhindered amines, converting them into hindered ones: therefore, the loading capability of the modified Lupasol is expected to improve as a consequence of this reaction. Subsequent blending of the modified Lupasol with PSf was performed in small amount (i.e. between 2 and 20 wt% with respect to PSf), and the characteristics of the blended membranes were compared to neat PSf membrane.

4.2 Materials and Methods

4.2.1 Materials

Polysulfone (PSf, MW 35000 Da) in transparent pellet form, benzoyl chloride (99% purity), 1-methyl-2-pyrrolidone (NMP, ACS) were purchased by Sigma-Aldrich and used without any further purification. Lupasol G20 Polyethylenimine (MW 1300 Da, charge cationic density 16 meq/g TS, N:C ratio= 1/2) was kindly provided by BASF. Its structure is reported in Figure 4.1. Distilled water was used as coagulation bath in membrane preparation. Hollytex non-woven made of polyester with density 34 g/m² was acquired in STEM and used as support in the CO₂ module. Extra pure potassium hydroxide in pellets (Scharlab) was dissolved in deionized water to prepare absorptive solutions.

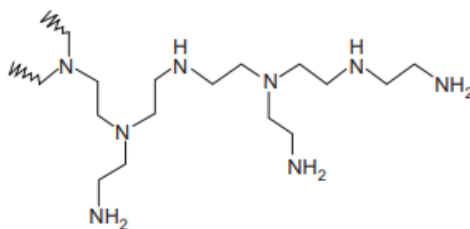
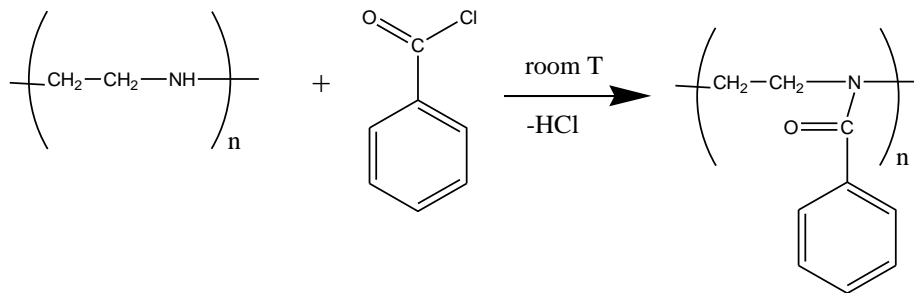


Figure 4.1 Chemical structure of Lupasol.

4.2.2 Additive preparation

Lupasol G20 was chemically modified, in order to reduce its water solubility, as schematized for the secondary amine groups in Scheme 4.1



Scheme 4.1 Reaction between Lupasol G20 and benzoyl chloride.

5.97 g (0.042 mol) of benzoyl chloride were added dropwise to 10 g of Lupasol G20 (ratio chloride/cationic groups = 0.25). The reaction was performed at 25°C under magnetic stirring for two hours; the reaction product was washed several times with distilled water under stirring and finally decanted,

yielding mG20, an oily product which was vacuum dried at room temperature for 24h. ^1H NMR (CD_3OD , TMS, δ , ppm): 6.8-7.9 (m, Ar), 2.2-4.2 (m, N- CH_2 - CH_2 -N).

4.2.3 Membrane preparation

As seen in Table 4.1, all membranes were prepared by phase inversion precipitation process in ambient conditions. Specific amount of polymer was dissolved in N-Methylpyrrolidone (NMP) to obtain 20 g of solution in which mass ratio between total polymer content and solution was maintained constant at 20 wt%. Resulting mixtures were stirred for 48 h and left overnight for degasification and sonicated for 30 min before the membrane preparation. Solutions were cast on a glass support by using casting knife (knife thickness= 250 μm), and immediately immersed into a coagulation bath containing a non-solvent, where the membranes precipitate as a result of the exchange between solvent (NMP) and non-solvent (water). Prepared flat sheet membranes were taken out from coagulation bath, washed with distilled water, and left overnight to dry in air.

4.2.4 Membranes characterization

^1H NMR spectra of mG20 in deuterated methanol (CD_3OD) were recorded at 400 MHz on a Varian Gemini 400 spectrometer (Varian Inc., Palo Alto, CA, USA). A pulse delay time of 5 s was used. The solvent peak was taken as the reference, and the chemical shifts were given in parts per million from TMS (Tetramethylsilane) with the appropriate shift conversions.

The membranes morphology was characterized by Environmental Scanning Electronic Microscopy using a FEI Quanta 600 (ThermoFisher Scientific, Waltham, MA, USA). The samples were cryofractured into liquid nitrogen and then fixed on the support suitable for the cross-section analysis. For detection of potassium carbonate, a back scattered electron detector (BSED) was employed.

Images obtained from ESEM were analyzed with ImageJ and IFME software [12] to obtain information about membrane thickness and pore size with 20-30 measurements per sample.

The overall membrane porosity (ε), defined as the volume of the pores divided by the total volume of the membrane, was determined from the bulk and the polymer density using a method based on the density measurements according to the following equation:

$$\varepsilon = \left(1 - \frac{\rho_m}{\rho_p}\right) 100\% \quad (1)$$

where ρ_p corresponds to the polymeric material density, which is a weighted average of polysulfone (1.24 g/cm³) and lupasol (1.08 g/cm³) density, and ρ_m to the membrane density. ρ_m is calculated by determining the relationship between mass and volume of 1 cm² of membrane.

The membrane surface morphology and roughness were determined by Atomic Force Microscopy (AFM) and images obtained were analyzed with WsxM software [13]. The membrane surface roughness parameters of the membranes were expressed in terms of root mean square of the Z (R_q).

Water contact angle of the membranes was determined by Dataphysics PCA 15EC. A 3 μ L droplet of Milli-q water was placed on the surface of the membrane and the contact angle was calculated from a digital image by SCA software (DataPhysics, Fildertstadt, Germany) included in the apparatus. Contact angle values were taken as the average of three measurements.

Water uptake tests were performed on previously dried membranes (size: 1.5 \times 3 cm²). The membranes were dried at 60 °C for 72 h, weighed, soaked in deionized water for 24 h at room temperature, and reweighed. The water uptake (WU) was calculated as:

$$WU(\%) = \frac{W_{wet} - W_{dry}}{W_{dry}} \times 100 \quad (2)$$

The glass transition temperature of neat PSf membrane and blended membranes was determined by Differential Scanning Calorimetry by means of a Mettler DSC-821e, calibrated using an in standard (heat flow calibration) and an In-Pb-Zn standard (T calibration). Samples of approximately 5 mg were tested in aluminium pans with a pierced lid in N₂ atmosphere with a gas flow of 50 mL/min. Tests were performed in dynamic mode at a heating or a cooling rate of 10 °C/minute in cycle: the first heating was from 0 °C to 200 °C, followed by cooling to 0 °C; the second heating to 200 °C. T_g was determined as the inflection point in the heat flow signal step from the second heating scan.

Gas permeation tests were carried out using a self-made stainless-steel, dead-end apparatus containing a membrane to measure the carbon dioxide permeance. The effective membrane area in the module was 12.6 cm². Figure 4.2 shows a schematic representation of the system used in the process. Pure CO₂ or N₂ was injected into the module. Permeated gas flow was measured at 1, 2, and 3 bar, respectively, using a precision gas mass flow controller (Alicat scientific MC-500SCCM-D, Tucson, AZ, USA).

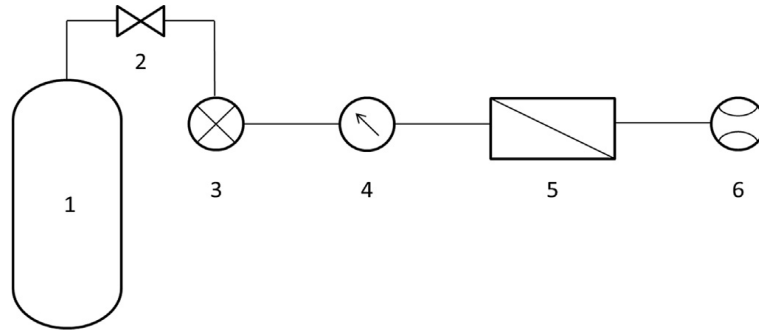


Figure 4.2 Permeability system: 1) CO₂ gas bottle, 2) valve, 3) pressure transducer, 4) manometer, 5) steel module containing membrane, 6) gas flow meter.

Finally, a mass transfer coefficient k [mol/s·m²·bar], was calculated following the equation:

$$k = \frac{n}{A \cdot \Delta P} \quad (3)$$

where n stays for mass transfer (mol/s), A is membrane area (m²), and ΔP driving force pressure gradient (bar).

The solubility of CO₂ into mG20 additive was studied by measurements of the pressure decay using the system described in Figure 4.2, with a small modification: the gas flow meter was removed, allowing the membrane-containing module to be closed tightly. Analyzed material was placed in the module and the valve 2 was open to introduce carbon dioxide into the system. When the pressure reached 200 kPa, the valve (2) was closed and pressure decrease was measured. The solubility was calculated according to equation (4):

$$n = \frac{(p_i - p_f)V}{RT} \quad (4)$$

where n is the adsorbed moles of CO₂, p_i and p_f are the initial and final pressures (Pa), respectively, V is gas volume of gas (m³), R is gas constant (8.314 J/K/mol), and T [K] is temperature. The solubility coefficient, S_{CO_2} , expressed in (m³ (STP)/m³ polymer atm) units, which are commonly used when referring to the solubility of gases, is calculated, respectively, by:

$$S_{CO_2} = \frac{V_{CO_2m}(STP)}{V_m p_{established}} \quad (5)$$

where V_{CO_2m} (STP)(m³) is the volume of CO₂ corresponding to n_{CO_2} at STP conditions (1.013 × 10⁵ Pa, 273.15 K), V_m is the analyzed material volume [m³] and $p_{established}$ (atm) is the pressure measured at equilibrium conditions. CO₂ absorption test was performed in which prepared membranes (9 cm²) were placed in a home-made module as reported in [7] and used for CO₂ absorption test conducted in a gas-liquid membrane contactor. A volume of 200 ml of 0.64 KOH solution was employed as liquid absorbent in

contact with the bottom surface of flat sheet membrane. The liquid absorbent was tested within a range of 35-228 ml/min and the experiments were performed for 1 h with continuous stirring. Bottom surface of the membrane was in contact with absorbent solution while the top surface was exposed to air by holes in the top side of the module. All experiments were carried out in room conditions (25 °C and 1.013×10^5 Pa), and each one was repeated three times to verify the reproducibility. After 1h, samples were collected and examined for CO₂ content.

To determine the absorbed CO₂ amount, carbon dioxide ion selective electrode (Thermo Scientific connected with Thermo Scientific Orion Dual Star pH/ISE Benchtop meter) was used. Diluted sample (1 ml sample + 45 Milli-q water) was mixed with CO₂ buffer (5 ml) to adjust the pH to the electrode working pH at 4.8-5.2. The apparatus was set to auto read mode and the CO₂ concentration in sample was measured. The stable value of CO₂ flux (mol/m²·s) in the membrane contactor was calculated according to the following:

$$J_{CO_2} = \frac{Q_i \cdot M_{CO_2}}{A} \cdot 1000 \quad (6)$$

where Q_i is the absorbent flow rate (m³/s), M_{CO_2} is CO₂ concentration in the absorbent (mol/L) obtained from the measurements, and A is the area of the flat sheet membrane (m²).

4.3 Results and Discussion

As previously stated, commercial Poly (ethylene imine) (PEI), Lupasol G-20, can be a suitable candidate for improving CO₂ sorption in PSf-based contactors when blended with Polysulfone, thanks to its high content of basic nitrogen. Nevertheless, it is highly soluble in water and this prevents its use as such in membrane preparation by phase inversion in DMF/water as well as in the final CO₂ capture device, which contains a basic aqueous solution in contact with the membrane. For this reason, Lupasol G-20 was chemically modified with benzoyl chloride as described in the experimental section to reduce water solubility. As a consequence of this reaction, the number of hindered amines should be increased, improving the carrier capability of this additive.

¹H NMR of modified Lupasol (mG20) in deuterated methanol, as seen in Figure 4.S1, showed two groups of broad, partially overlapped signals in the regions 6.8-7.9 (aromatic protons) and 2.2-4.2 (ethylenic protons adjacent to nitrogen atoms), which confirmed that reaction successfully occurred. According to Lupasol G20 initial composition, the ratio N:C is 1:2; therefore, each ethylene group approximately corresponds to one nitrogen atoms. From the integration of the aforementioned signals, we achieved a rough

estimation of the number of aromatic groups versus ethylene groups, that is, the aromatic groups/nitrogen atoms content, which resulted in 19%. The amount of benzoyl chloride for the reaction was 25% with respect to the cationic charge density of Lupasol G20; accordingly it can be concluded that chemical modification of Lupasol G20 occurred to a good extent. The achieved degree of modification was sufficient to reduce polymer solubility in water: mG20 was obtained after precipitation and washing in water.

Afterwards, mG20 was blended with PSf in different amounts, namely 2, 5, 10, and 20 wt%, as seen in Table 4.1), by dissolving both polymers in N-methylpyrrolidone (20 wt.% polymer/solvent) as described in the experimental section. Next, polymeric solutions were casted and immersed into a coagulation bath containing water, finally yielding flat sheet membranes (L2-L20), whose morphology was characterized by means of environmental scanning electron microscope (ESEM).

Table 4.1 Composition and morphological characteristics of the investigated membranes.

Membrane	mG20 content (wt. %)	Thickness (μm)	Porosity (%)
L0	0	123 \pm 4	74.3
L2	2	139 \pm 3	79.0
L5	5	151 \pm 6	81.8
L10	10	162 \pm 2	75.8
L20	20	196 \pm 3	69.2

Membrane thicknesses were determined by ESEM micrographs by means of ImageJ and IFME softwares, and are reported in Table 4.1. Porosity was calculated from the densities. Additionally, the pore size distribution was also determined by ESEM images and further analysis with the previously mentioned softwares; the obtained histograms are included in Figure 4.3. As can be seen in Figure 4.3a, in the case of L0, 90% of pores are homogeneously distributed at 3 and 11 μm , while in blended membranes, 80% of measured pores lie in the range 8-15 μm , i.e., the pore diameter increases when mG20 content is increased, though the number of pores decreases. For instance, while in case of L2 membrane, 70% of pores diameter gave a value of 5 μm , in L20 membrane 70% of pores ranges between 9 and 13 μm , and huge pores, with a diameter above 30 μm , was observed.

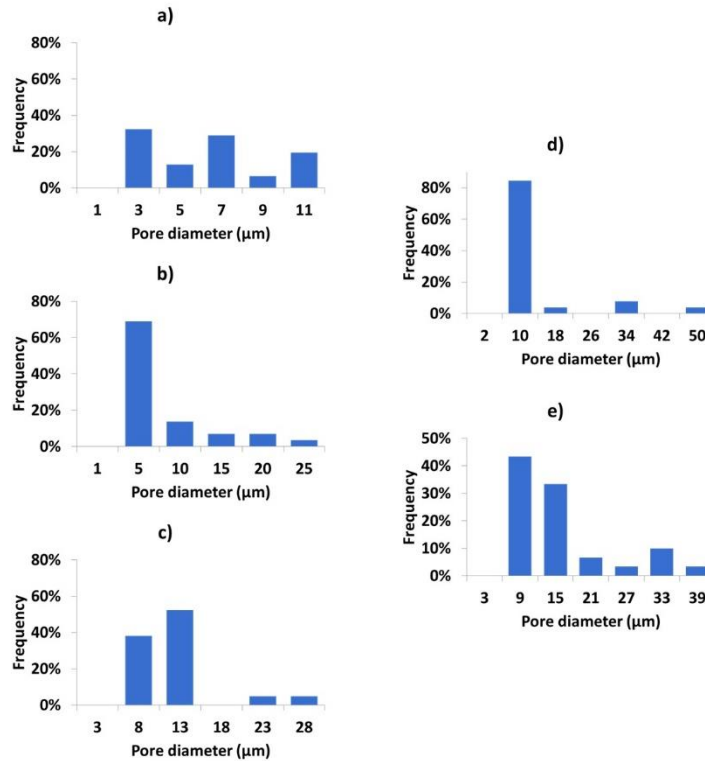


Figure 4.3 The pores size distribution histograms of membranes: (a) L0; (b) L2; (c) L5; (d) L10; (e) L20.

Figure 4.4b-e show the cross-section images of L2, L5, L10 and L20 membranes. For sake of comparison, the image of pure PSf membrane (L0) is also reported, as seen in Figure 4.4a.

Figure 4.4a shows that neat PSf membrane (L0) exhibits a finger-like structure on top of a spongy bulk matrix. A very similar morphology can be found for L2. On the other hand, when mG20 additive amount was increased, membrane morphology progressively changed: as seen in Figure 4.4c, in L5, finger-like pores decreased but a considerable amount of voids remained evident; L10 shows an evident spongy layer with a much denser layer, as seen in Figure 4.4d. In the case of L20, morphology is definitely denser, with some residual porosity on the top side, as seen in Figure 4.4e. This change is also shown by the trend observed for porosity values, which are related to the voids content, as explained in the experimental part. They initially increased with increasing mG20 content, reaching the highest value for L5; subsequently, they decreased, with a minimum for L20. This confirms that membrane morphology becomes denser at higher mG20 contents. Membrane morphology is predominantly affected by the precipitation rate during the phase inversion process. Fast precipitation is determined by fast penetration of the non-solvent into the polymeric solution and leads to highly asymmetric structures, with finger-like macrovoids; slower coagulant penetration, and consequently slower precipitation, produce sponge-like and more symmetrical structures.. Thus, the more affine polymer and the coagulant are, the slower precipitation will be, and the

more symmetrical structures can be expected. In our case, mG20 additive is a relatively hydrophilic, polar polymer; when blended with PSf, it contributes to a decrease in the precipitation rate of the polymeric solution. This effect is more evident in L20, which contains the highest mG20 amount and exhibits the densest structure and the lowest porosity of the whole series. At low mG20 content, the effect of this component seems to be a very limited change of the solution thermodynamic stability, with consequent similar precipitation rates, and final membrane morphologies which strongly resemble the one of pure PSf; on the other hand, when mG20 amount increases, then the solution thermodynamic stability seems to be enhanced, leading to slower precipitation rates and resulting in final morphologies remarkably different with respect to neat PSf. In addition, it should be taken into account that the presence of an additive not only modifies the thermodynamic stability of the polymeric solution but can also alter its viscosity, which can determine a change in the phase inversion process.

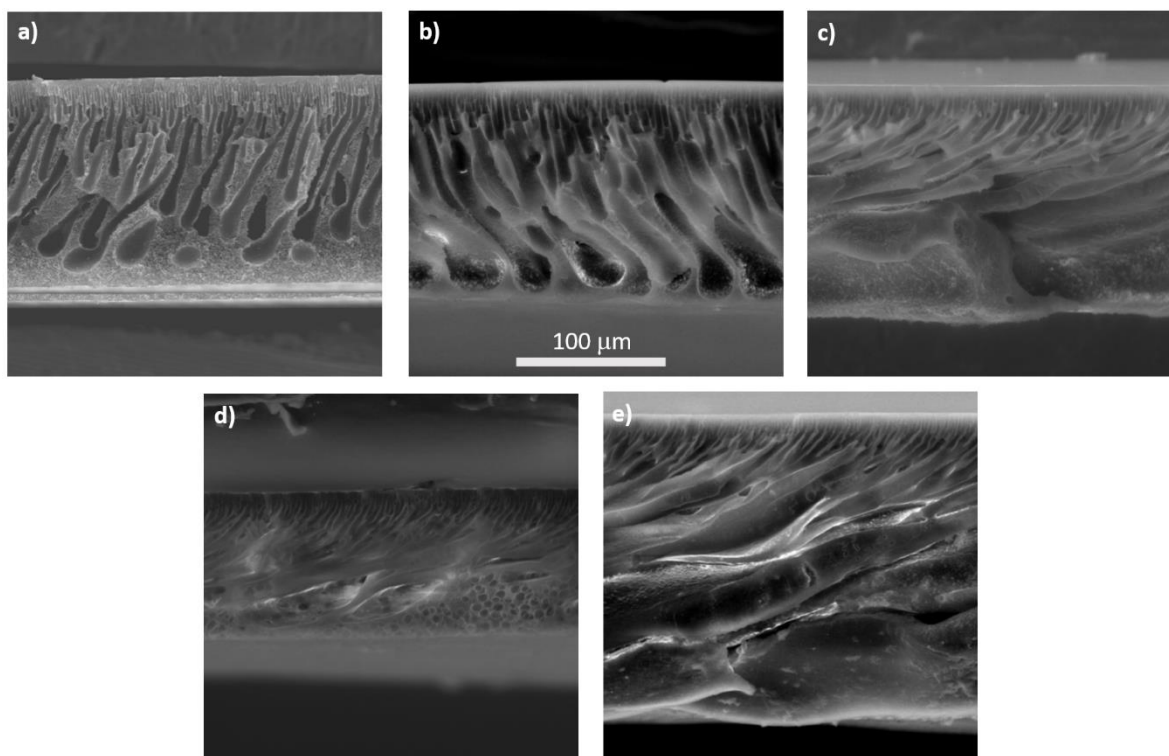


Figure 4.4 ESEM micrographs of the cross-section of PSf-mG20 membranes: (a) L0; (b) L2; (c) L5; (d) L10; (e) L20.

The obtained membranes are to be used in a device wherein the bottom surface is in direct contact with an aqueous absorbent solution. Therefore, PSf-mG20 membranes were characterized in terms of surface morphology, water contact angle, and water uptake to establish whether blending with mG20 could eventually affect their wettability with respect to neat PSf. Figure 4.5a-e report the AFM topographic image

pattern of bottom side of L0-L20 membranes; Table 4.2 reports their RMS roughness as well as the values of the water contact angle and water uptake.

As seen in Table 4.2, blending with mG20 determines an increase of RMS roughness of bottom side, i.e., the higher mG20 amount, the rougher the bottom membrane surface. As for membrane wettability, water contact angle decreases with an increase mG20 content, as can be expected based on its higher hydrophilicity with respect to PSf; moreover, this effect is more evident on the bottom of the membrane, which suggests that mG20 could be more concentrated on this side.

Table 4.2 RMS roughness of bottom side, water contact angle (CA) and Water Uptake (WU) of PSf-mG20 membranes.

Membrane	RMS roughness (nm)	Top CA (°)	Bottom CA (°)	WU (%)
L0	7.5	87±3	86±4	0.40 ± 0.05
L2	6.1	83±1	72±4	6.0 ± 0.6
L5	8.2	79±2	73±3	45 ± 5
L10	10.5	77± 2	70±1	142 ± 20
L20	15.8	77±1	65±1	274 ± 17

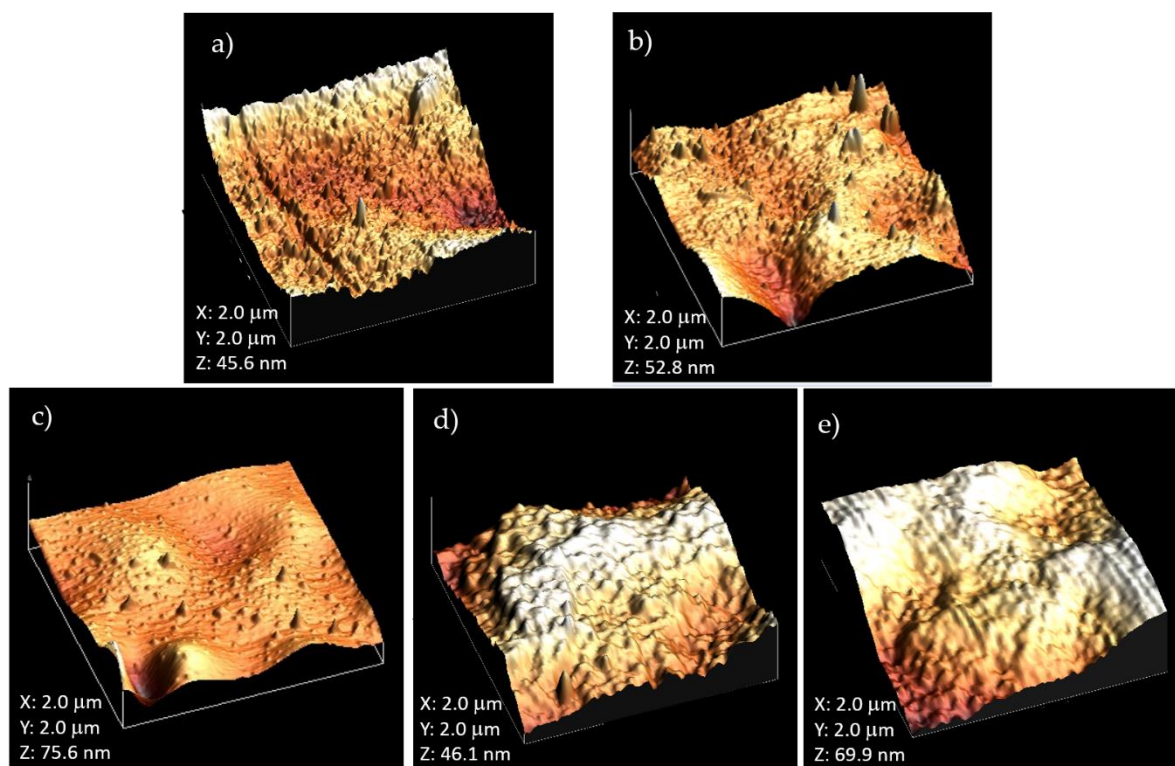


Figure 4.5 Atomic Force Microscopy (AFM) topographic images of bottom side of PSf-mG20 membranes: (a) L0; (b) L2; (c) L5; (d) L10; (e) L20.

To determine the distribution of mG20 additive in PSf membrane, we checked Raman absorption across their section between 200 and 2500 cm^{-1} , at different depths, starting from the top side moving towards the bottom side. Figure 4.6 shows Raman spectra of recorded on the top of L20 membrane, of neat mG20 additive and L0 (neat PSf) membrane, respectively. The only band which can be attributed exclusively to the additive and it is not overlapped with other PSf bands is that at 1030 cm^{-1} , as seen in Figure 4.6a, attributed to the C-N stretching of secondary and tertiary aliphatic amines [14]. This band can be guessed as a shoulder also in the Raman spectra of L20 membrane, as seen in Figure 4.6b, which contains the highest amount of additive. As seen in Figure 4.S2, mG20 seems to be present throughout the whole membrane cross-section, since the shoulder at 1030 cm^{-1} can be observed in the spectra of top, center and bottom of the membrane. Unfortunately, when the Raman spectra of L10 membrane were observed, as seen in Figure 4.3, this band was not visible, probably due the lower amount of mG20 in this sample; as expected, the same was also found in the case of L2 and L5 membranes. Therefore, we could not check the actual distribution of mG20 in L2-L10 membranes.

We also studied water uptake (WU) of L0-L20 membranes. As shown in Table 4.2, the presence of mG20 additive remarkably increases water uptake of these systems with respect to neat PSf; however, only 2 wt.% additive determines 6% WU in comparison with 0.4% of neat PSf (L0). Finally, L20 membrane, with the highest mG20 content, exhibits two orders of magnitude higher WU than L0. This effect can be attributed to high hydrophilicity of mG20 additive and could compromise the dimensional stability and performance of the membranes, thus representing a drawback in the use of these composite membranes in the final CO_2 capture device. Penetration of the liquid into the membrane pores negatively affects absorption flux since, in this case, gas diffusivity in the liquid phase is far lower than in gaseous phase.

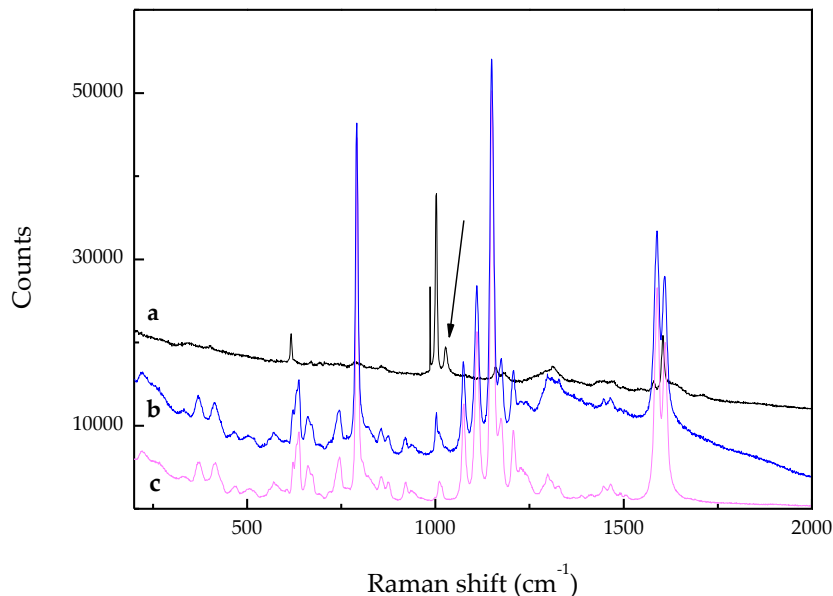


Figure 4.6 Raman spectra between 200 and 2500 cm^{-1} of: (a) mG20; (b) Top surface of L20; (c) L0. The arrow indicates the band at 1030 cm^{-1} .

Absorption performance of composite membranes was evaluated for potassium hydroxide solution in a flat sheet membrane contactor (FSMC) in cross flow module at different liquid flow rates. Results are shown in Figure 4.7 as carbon dioxide flux versus absorbent flow rate.

Results show that, at the lowest absorbent flow rate (35 mL/min), performances of membranes are very similar as regards CO_2 flux, as seen in Figure 4.7. In the mass transfer process between gaseous and liquid streams through a porous membrane, resistance can be split into three terms: liquid side, gas side and membrane mass transfer resistances [15]. The effect of gas side resistance can be neglected because we used ambient air as the CO_2 source, thus gas concentration was constant in all our experiments. At low liquid flow rate, the resistance term related to the liquid side mainly affects the total mass transfer resistance. This determines very similar gas absorption flux at low liquid absorbent flow rate, as shown in Figure 4.7. Nevertheless, on increasing absorbent flow rate (120-228 mL/min), remarkable differences can be found, which can be attributed to the different mG20 additive content; in particular, the behavior of the membranes with lower additive amount (L2 and L5) was more efficient than neat PSf, L5 having far the best performance. On the other hand, the presence of higher amounts of mG20, namely 10 and 20 wt.%, seems to be detrimental to CO_2 capture when compared with neat PSf.

With an increase in the liquid flow rate, the liquid side mass transfer resistance is reduced and eventually, above a certain flow rate, the mass flux is predominantly influenced by the membrane

resistance. When this occurs, the plot of absorption flux versus liquid flow rate levels off. In our case, this situation is clearly shown by L5 and L20 membranes; however, we will try to explain the behavior of the whole series in terms of membrane mass transfer resistance. L0-L20 membranes differ as far as chemical composition and morphology are concerned: therefore, different factors should be taken into account. First, the presence of mG20 additive determines a remarkable increase of CO₂ solubility into the polymeric membrane. CO₂ solubility into neat PSf membrane was determined as 4.79±0.01 m³ STP/m³ atm [7]; in contrast, this value rose to 21.3 m³ STP/m³ atm for neat mG20 additive. On the other hand, the presence of the additive strongly affects membrane morphology, reducing porosity, and void contents, and is thus detrimental to CO₂ diffusivity. Another factor, previously mentioned, is the strong increase in wettability and water uptake deriving from mG20 addition, which, in turn can help the penetration of the liquid phase into the membrane, provoking membrane clogging, and negatively affecting gas diffusivity. Another point that could have some influence on membrane performance is the plasticizing effect of mG20 on PSf; for neat PSf (L0) membrane, a glass transition temperature of 184°C was found, while this value reduced to 173°C for L20 membrane. Glass transition is strictly related to the polymer free volume, which also has a role in gas transport through polymeric membranes [16, 17].

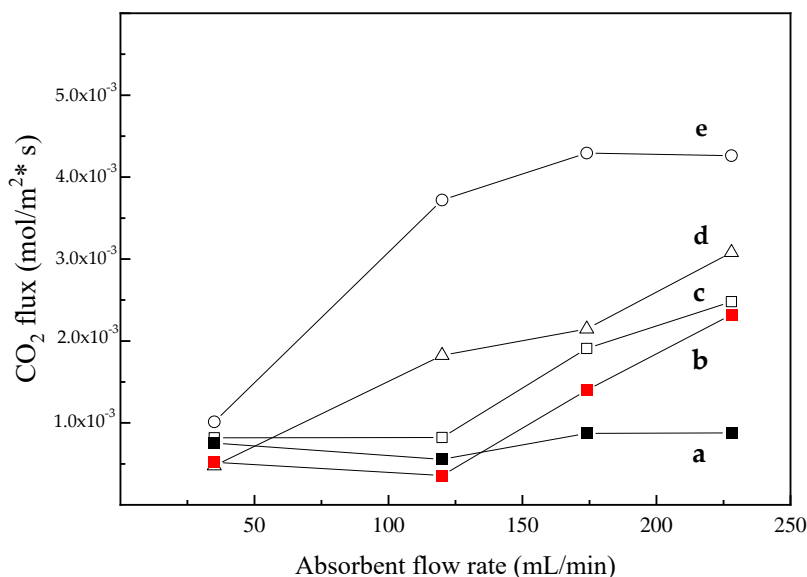


Figure 4.7 CO₂ absorption flux into L0-L20 membranes as a function of liquid absorbent flow rate. (a) L20; (b) L10; (c) L0; (d) L2; (e) L5.

Permeation in glassy polymers has been modeled in terms of diffusion-solution. The dual mode sorption model [18, 19] assumes that a polymer consists of a continuous chain matrix and microvoids, frozen in the matrix. These voids are caused by the unrelaxed volume of polymers in the glassy state. Therefore, the dual mode sorption model makes reference to two terms: the former based on Henry's law

of solubility, i.e., dissolution of the permeant in the continuous chain matrix; the latter is a Langmuir-type term related to permeant sorption in microvoids. Therefore, in our case, it is reasonable to suppose that the addition of mG20 determines two contrasting effects. On the one hand, increased amounts of the additive enhance CO_2 solubility into the polymeric matrix; nevertheless, this also provokes a decrease in microvoids content, as shown by ESEM analysis. Importantly, mG20 greatly increases water uptake and therefore KOH solution penetration from the bottom side of the contactor, with consequent membrane pores clogging. L5 membrane shows the best performance in the whole series, suggesting that this additive amount (5 wt %) represents the best compromise between these two opposite effects. It was reported that total pore volume and specific surface of nanoporous shale decreased after CO_2 adsorption, and that this phenomenon can be interpreted in terms of physisorption, associative chemisorption, and dissociative chemisorption [20]. The first is related to the adsorption of carbon dioxide molecules in the organic pores that produces a variation in the shale surface energy, which, in turn, produces a swelling phenomenon; as a consequence, the pore volume decreases, pores are blocked and CO_2 is trapped inside the structure. This phenomenon has been modelled and was found to be relevant in the case of pressure higher than 0.5 MPa [21]; however, in our case, experiments were performed at CO_2 atmospheric pressure. An interesting parallel experiment could be performed with associative chemisorption of carbon dioxide at shale mineral surfaces or pores: in conditions of high pressure and temperature, CO_2 and H_2O can react with minerals, thus generating new products, such as carbonates, which can cover the pore walls and cause geochemical and morphological changes to the shale. Consequently, the pore may be blocked and the pore volume decreases. In our case, penetration of absorber KOH solution into the blended membrane was expected to induce the precipitation of K_2CO_3 that could block membrane pores in a similar way. As a matter of example, Figure 4.8a,b show the bottom surface and cross-section ESEM micrographs taken with BSED of L2 membrane, respectively, after 4 experiments in the flat sheet membrane contactor., in contrast, Figure 4.8c shows the results of energy dispersive X-ray analysis (EDX) of the white spots observed in the shown micrographs.

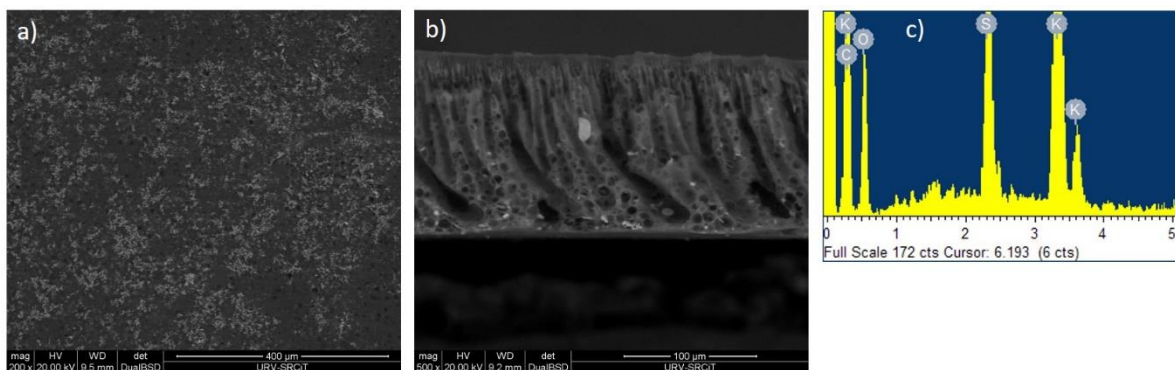


Figure 4.8 ESEM micrographs with BSED of L2 membrane after 4 experiments in a flat sheet membrane contactor:

(a) bottom surface; (b) cross-section; (c) X-ray analysis (EDX) analysis of the white spots seen in the micrographs.

Figure 4.8a,b demonstrate the presence of white crystals both on the bottom surface of the membrane in direct contact with KOH solution and on the bottom side of the membrane cross section. As seen in Figure 4.8c, EDX analysis revealed that these crystals could be formed by potassium carbonate. Therefore, these results suggest that, even in the case of L2 membrane, the penetration of KOH solution from the contactor into the membrane can induce K_2CO_3 precipitation that may eventually block the pores. This effect is expected to be more pronounced in blended membranes with much higher water uptake and, consequently, more efficient penetration of KOH solution, i.e., L10 and L20, and could drastically reduce the membrane performances.

Permeability tests were performed to calculate the mass transfer coefficients, k , for the L0-L20 membranes series. K was calculated from CO_2 as well as from N_2 permeation to verify the role of chemical composition in the gas permeability of these membranes.

Figure 4.9 reports the mass transfer coefficient k calculated from CO_2 and N_2 permeation through L0-L20 membranes

Figure 4.9 shows that k has an increasing trend with increasing amount of mG20: the addition of just 2 wt% mG20, determines an order of magnitude higher mass transfer coefficient for both CO_2 and N_2 permeation, despite the similar morphology of L0 and L2 membranes. Nevertheless, the effect of mG20 is much more pronounced for carbon dioxide than for nitrogen, when the full composition range is examined. In addition, the N_2 mass transfer coefficient is always lower than CO_2 mass transfer coefficient for L2-L20 systems, despite having practically the same value in L0 which contains no additive. This suggests that the permeation of these gases does not only depend on the ratio between the pores of the membranes and molecular size of gases, but also on the chemical composition, that is, it is not exclusively governed by physical parameters. Results suggest that carbon dioxide permeation was enhanced thanks to its favorable interaction with the amines contained in mG20, provided that, for instance, the Van der Waals radius of nitrogen is 1.95 Å, while that of carbon dioxide is 5.331 Å in the direction of the oxygen atoms and 3.033 Å in the normal direction [21, 22].

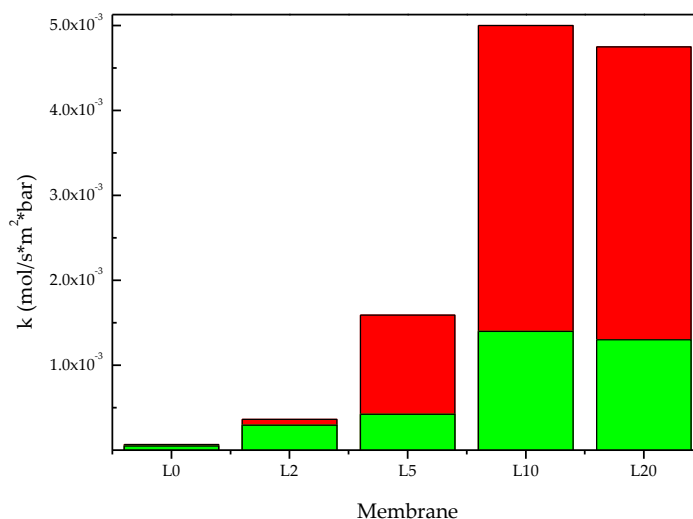


Figure 4.9 Mass transfer coefficient of L0-L20 membranes relative to: N₂ (green bar); CO₂ (red bar).

Therefore, the addition to PSf membranes of relatively low amounts of a high molecular weight additive such as mG20, which contains a big amount of basic amine groups, is effective in improving CO₂ permeability in the gas phase.

4.4 Conclusions

We tested the use of a high molecular weight additive, mG20, obtained by chemical modification of a commercial Polyethylenimine, to improve the performance of PSf membranes in membrane contactors for CO₂ capture due to the presence of basic nitrogen atoms. The amount of blended mG20 was in the range of 2–20%. We found that the presence of the polymeric additive determined a change in the membrane morphology: porosity was increased up to 5 wt % mG20, but decreased upon further mG20 addition, giving denser membranes. Blending with the hydrophilic additive produced membranes with rougher surfaces, higher water contact angles and water uptake, as expected. The presence of mG20 also improved the mass transfer coefficient for both N₂ and CO₂, but the effect was much more marked for the latter, revealing an increase in carbon dioxide permeability as a consequence of blending with the additive. On the other hand, when the application of these membranes in the final CO₂ capture device is considered, we found that, when mG20 amount was higher than 5 wt %, increased water uptake and eventual K₂CO₃ precipitation provoked membrane pores clogging and negatively affected CO₂ permeability. This effect was more evident when higher liquid flow rates were used in the contactor.

In conclusion, the performance of PSf membranes in carbon dioxide capture device can be greatly improved by blending with mG20 amount as low as 5 wt % since this composition represents the best compromise between higher membrane affinity for CO₂, induced by the presence of basic nitrogen atoms and the changes in morphology, wettability, and water uptake, which are detrimental at higher additive amounts. The study of durability and consequent performance variation of these composite membranes is currently under study and will be the subject of a forthcoming paper.

4.5 References

1. Leung, D. Y. C.; Caramanna, G.; Meccredes Maroto-Valer, M., An overview of current status of carbon dioxide capture and storage technologies. *Renewable and Sustainable Energy Reviews* 2014, 39, 426-443
2. Stocker, T. F.; Qin, D.; Plattner, G.-K., IPCC, Climate change 2013: the physical science basis, in Contribution of Working Group I to the Fifth Assessment Report of the Intergovernmental Panel on Climate Change.; NY, USA 2013;
3. Metz, O. D.; Coninck, H. C. d.; Loos, M.; Meyer, L. A., IPCC Special Report on Carbon Dioxide Capture and Storage. Working Group III of the Intergovernmental Panel on Climate Change., in; IPCC, Cambridge, United Kingdom and New York, NY, USA. 2005;
4. Hao, P.; Wijmans, J. G.; Kniep, J.; Baker, R. W., Gas/gas membrane contactors – An emerging membrane unit operation. *J. Membr. Sci.* 2014, 462, 131-138
5. Zhao, S.; Feron, P. H. M.; Deng, L.; Favre, E.; Chabanon, E.; Yan, S.; Hou, J.; Chen, V.; Qi, H., Status and progress of membrane contactors in post-combustion carbon capture: A state-of-the-art review of new developments. *J. Membr. Sci.* 2016, 511, 180-206
6. Witek-Krowiak, A.; Dawiec, A.; Modelski, S.; Podstawczyk, D., Carbon Dioxide Removal in a Membrane Contactor – Selection of Absorptive Liquid/Membrane System. *International Journal of Chemical Engineering and Applications* 2012, 3, 391-395
7. Nogalska, A.; Ammendola, M.; Tylkowski, B.; Ambrogi, V.; Garcia-Valls, R., Ambient CO₂ adsorption via membrane contactor - Value of assimilation from air as nature stomata. *J. Membr. Sci.* 2018, 546, 41-49
8. Danckwerts, P. V., The reaction of CO₂ with ethanolamines. *Chem. Eng. Sci.* 1979, 34, 443-446
9. Alper, E., Reaction mechanism and kinetics of aqueous solution of 2-amino-2-methyl-1-propanol and carbon dioxide. *Ind. Eng. Chem. Res.* 1990, 29, 1725-1728

10. Zi TongHo, W. S. H., New sterically hindered polyvinylamine membranes for CO₂ separation and capture. *J. Membr. Sci.* 2017, 543, 202-211
11. Vakharia, V.; Salim, W.; Wu, D.; Han, Y.; Chen, Y.; Zhao, L.Ho, W. S. W., Scale-up of amine-containing thin-film composite membranes for CO₂ capture from flue gas. *J. Membr. Sci.* 2018, 555, 379-387
12. Torras, C.Garcia-Valls, R., Quantification of membrane morphology by interpretation of scanning electron microscopy images. *J. Membr. Sci.* 2004, 233, 119-127
13. Horcas, I.; Fernandez, R.; Gomez-Rodriguez, J. M.; Colchero, J.; Gomez-Herrero, J.Baro, A. M., WSXM: a software for scanning probe microscopy and a tool for nanotechnology. *Rev. Sci. Instrum.* 2007, 78, 013705
14. Socrates, G., *Infrared and Raman Characteristic Group Frequencies: Tables and Charts*, 3rd Edition, John Wiley & Sons, Ltd: John Wiley & Sons, Ltd Location, Country, 2004,
15. Bakeri, G.; Ismail, A. F.; DashtArzhandi, M. R.Matsuura, T., Porous PES and PEI hollow fiber membranes in gas-liquid contacting process - A comparative study. . *J. of Membr. Sci.* 2015, 475, 57-64
16. Stern, S. A.; Fang, S. M.Frisch, H. L., Effect of pressure on gas permeability coefficients. New application of "free volume" theory. *J. Polym. Sci. A-2, Polym. Phys.* 1972, 10, 201-219
17. Tant, M. R.Wilkes, G. L., An overview of the non equilibrium behavior of polymer glasses. *Polym. Eng. Sci.* 1981, 21, 874-895
18. Barrer, R. M., Diffusivities in glassy polymers for the dual mode sorption model. . *J. Membr. Sci.* 1984, 18, 25-35
19. Paul, D. R., Dual Mode Sorption Model., in *Encyclopedia of Membranes.*; Drioli, E.; Springer-Verlag, Berlin Heidelberg 2014;
20. Huang, X.; Zhao, Y.-P.; Wang, X.Pan, L., Adsorption-induced pore blocking and its mechanisms in nanoporous shale due to interactions with supercritical CO₂. *J. Petrol. Sci. Eng.* 2019, 178, 74-81
21. Brochard, L.; Vandamme, M.; Pellenq, R. J.-M.Fen-Chong, T., Adsorption-induced deformation of microporous materials: coal swelling induced by CO₂-CH₄ competitive adsorption. *Langmuir* 2012, 28, 2659-2670
22. Batsanov, S. S., Van der Waals radii of elements. *Inorganic Materials* 2001, 37, 871-885

UNIVERSITAT ROVIRA I VIRGILI
NOVEL POLYMERIC MEMBRANES FOR ARTIFICIAL PHOTOSYNTHESIS
Alireza Zare



Chapter 5.

Facilitated direct air capture of CO₂ in polysulfone membrane contactors by improving stability and hydrophobicity of amine additives

UNIVERSITAT ROVIRA I VIRGILI
NOVEL POLYMERIC MEMBRANES FOR ARTIFICIAL PHOTOSYNTHESIS
Alireza Zare

5.1 Introduction

Fossil fuel is the most important source of energy with almost no alternatives. Power plants burn fossil fuels to produce electricity and energy. Therefore, post-combustion gases released are considered the main factor for emission increase. The energy industries based on fossil fuel, such as petroleum, coal, natural carbon dioxide gas and metal processing, are not only the centerpiece of economic development but also the main body of CO₂ emissions. Atmospheric CO₂ concentration has become a subject of worldwide concern because it seriously contributed to global warming and climate change, which resulted in serious environmental problems [1,2]. In 2007, reports of the International Panel on Climate Change (IPCC) indicated that the global CO₂ emissions must be cut by 50–80% by 2050. Otherwise, human beings could face the most damaging effects emerging from climate change [3,4]. The International Energy Agency (IEA) has pointed out that the global electricity demand would be expected to increase by 70% between 2010 and 2035 [4]. Even with the rapid development of renewable energies, most of electricity would still come from fossil fuel for the next few decades, which makes the CO₂ emission reduction a major challenge. Hence, it is necessary to explore low energy-consumption, cost-effective, available and efficient technologies for the capture and separation of CO₂ produced by the industrial sources.

Several methods have been identified for the removal and capture of CO₂ based on physical and chemical processes: absorption, adsorption, conversion, cryogenic separation, and membrane techniques [5-7]. Absorption via amine-based solvents is the most notable process in large scaled industries. However, membrane technology holds great promises for CO₂ capture by gas-liquid absorption. It has several attractive advantages compared to other CO₂ capture methods: high energy efficiency, cost effective method, compact and portable systems that are simply operated [8]. Recently, new hybrid processes have been studied, they take advantage from advanced membrane technologies and CO₂ absorption methods in a single device. In these devices, the membrane plays the role of a physical barrier that separates the two phases; this system is called a contactor [6,7]. In membrane contactors, CO₂ absorption occurs when a gas stream enters the system through the membrane pores and gets in contact with the aqueous absorbing solution that flows in the opposite side of the membrane [8,9]. Therefore, the surface area for phase contact increases, which facilitates the mass exchange process [10]. On the other hand, membrane pores should be filled with gas to prevent any membrane wetting. Consequently, membrane mass transfer resistance decreases while CO₂ flux increases [9,11,12].

The common materials for CO₂ removal membranes are organic polymers. Polysulfone is widely employed as an asymmetric porous membrane in different gas separation and absorption processes [13,14]. For this reason, it has been extensively considered for CO₂ capture with relatively high selectivity and

permeability. Furthermore, polysulfone has excellent mechanical strength, high thermal and chemical stability but also good hydrophobicity and low mass transfer resistance for CO₂ [15]. All these properties above make this polymer a good choice for membrane gas absorption processes [16].

Amines are currently the most efficient and cost-effective materials for CO₂ capture [17,18]. It is often mentioned that primary amines are more reactive towards CO₂. However, in order to fully investigate the effects of amines on CO₂, the electronic and steric effects of all substituents attached to the nitrogen atoms should be considered. Furthermore, the basicity of amines is the most critical factor that affects CO₂ capture performance due to the acid/base reaction between CO₂ and amines. The reaction between CO₂ and a primary or secondary amine that are sterically unhindered forms a stable carbamate. Only half mole of CO₂ is absorbed per mole of amine group (Scheme 5.1.a). However, it was shown that the formation of some hydrogen carbonate could increase this sorption ratio (Scheme 5.1.b). Since the carbamate is fairly stable, the absorbent regeneration is difficult due to the high amount of heat energy needed to break the bonds [19]. In contrast, tertiary and hindered amines form an unstable carbamate and, due to a hydrolysis reaction, lead to the formation of hydrogen carbonate ions, which results in a loading capacity of one mole CO₂ per mole of amine group (Scheme 5.1.c) [20]. Aqueous amine solutions, such as mono-(MEA) and diethanolamine (DEA), have been used to capture CO₂ and generate food-grade carbon dioxide in the natural gas industry since decades [21].



Scheme 5.1 Equations of: (a) Carbamate formation; (b) Hydrogen carbonate formation; (c) Carbamate reversion to hydrogen carbonate.

Aqueous amine absorption is practical to capture CO₂ from gas streams with a low partial pressure of CO₂. However, amine solutions are limited to be used with low concentrations for different processes in CO₂ recovery plants, due to equipment corrosion and amine solvent degradation caused by oxygen present in aqueous solution [22]; however, the biggest issue is the high heat capacity of the amine solution that occurs in the aqueous phase for CO₂ capture, which causes a high energy consumption. Moreover, technical scalability limits its application to CO₂ capture from flue gas emissions of electricity power plants that burn coal or natural gas. For that reason, CO₂ capture by using solid adsorbents, such as polyamines, is considered as a promising alternative to avoid all problems related to aqueous amine absorbents. Polyamines, are being intensively investigated by loading and blending them with other support materials, such as membranes. Therefore, polyethyleneimine (PEI) is the most investigated because it is relatively

cheap, easily synthesized and more thermostable compared with other amine-based adsorbents or amine oligomers [23]. Since PEI was introduced for CO₂ capture in space shuttle applications by Satyapal et al.[24], many researchers have studied PEI as an adsorbent for CO₂ capture by loading it on many support materials. Nogalska et al. reported a biomimetic contactor, designed as artificial stomata, based on a polysulfone membrane and a potassium hydroxide solution used as an absorbent, which is in direct contact with the bottom side on the membrane. For this system, CO₂ absorption was found even higher than in the natural stomata (40 μmol/m²*s) [25]. In a previous paper, we tried to improve the performance of polysulfone (PSf) membranes used for CO₂ capture from ambient air, by blending them with a commercial hyperbranched polyethylene imine, namely Lupasol G20, chemically modified with benzoyl chloride at partial extent (aromatic groups/nitrogen atoms content around 19%), to give mG20 additive [26]. The partial chemical modification of Lupasol G20 was carried out in order to decrease its water-solubility; in this way, the blended PSf membranes could be prepared by phase inversion precipitation in a water coagulation bath. We found that the presence of the polymeric additive determined an increase in carbon dioxide permeability; on the other hand, when these blended membranes were applied in the CO₂ capture device, increased water uptake and eventual K₂CO₃ formation and pore clogging was evidenced when the additive amount was higher than 5 wt%. This determined worse performances in terms of CO₂ permeability in those cases. On the other hand, it must be also pointed out that the chemical modification reaction took place on primary and secondary amines of the Lupasol G20 structure, consequently forming hydrochloric acid (HCl) as a byproduct that could be trapped on the membrane matrix and affect membrane stability.

For this reason, in the present paper we investigated a different approach for Lupasol G20 chemical modification to increase both, its hydrophobicity and stability of the final blended membrane. Before blending with polysulfone, Lupasol G20 was therefore partially modified by phenyl isocyanate, giving UG20 additive, to decrease its water-solubility. Consequently, this converted the sterically unhindered nitrogen atoms into sterically hindered ones by forming urea groups; moreover, these groups are more basic compared to the amide formed in the previous modification by benzoyl chloride. Additionally, the stability of the membrane is expected to increase as well, since the reaction performed produces no side product that could be trapped in the polymer. PSf-based membranes with different amounts of the modified Lupasol G20 were studied (specifically 2, 5 and 10wt% with respect to PSf) and compared to neat PSf membrane.

5.2 Materials and Methods

5.2.1 Materials

Polysulfone (PSf, MW 35000 Da) in transparent pellet form, phenyl isocyanate (98%) and 1-methyl-2-pyrrolidone (NMP, ACS) were purchased from Sigma-Aldrich (Sigma Aldrich Química, Madrid, Spain) and used as received. Polyethyleneimine (PEI) (Lupasol G20, 1300g/mol) was kindly provided by BASF (Tarragona, Spain) and used as received. Its structure is reported in Figure 5.1.

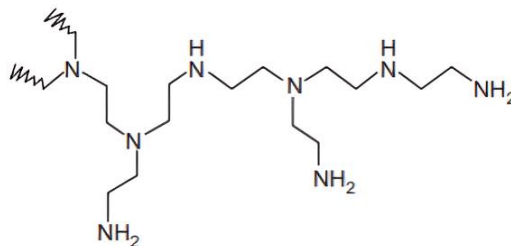
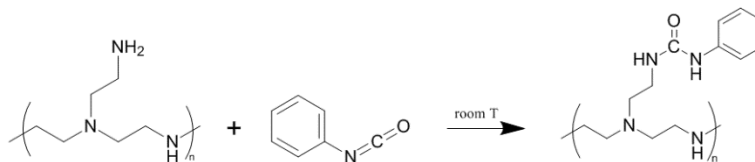


Figure 5.1 Chemical structure of Lupasol.

MilliQ water was used as coagulation bath in membrane preparation. Extra pure potassium hydroxide in pellets (Scharlab, Barcelona, Spain) was dissolved in deionized water to prepare solutions for membrane swelling tests .

5.2.2 Additive preparation

Lupasol G20 was chemically modified to reduce its water solubility, as seen for primary amines in Scheme 5.2. The modification of PEI was performed with 25% of stoichiometric amount of phenyl isocyanate with respect to the cationic charge density of Lupasol G20 (17 meq/g) by adding 5.1 g drop-wise directly to 10 g of Lupasol G20 magnetically stirred for two hours at room temperature. The reaction was then left overnight. The resultant product was washed three times by distilled water under stirring, which resulted in UG20, an oily product that was left to dry for 24h. The modified Lupasol G20 was finally analyzed by ^1H NMR, as can be seen in Figure 5.S1. The final modification degree was found to be around 17%.



Scheme 5.2 Reaction between Lupasol G20 and phenyl isocyanate.

5.2.3 Membrane preparation

All polysulfone-based membranes were prepared by phase inversion process in ambient conditions. N-Methylpyrrolidone (NMP) was used to dissolve 20 g of PSf/UG20 blending so that the total polymer concentration would be fixed at 20 wt.% with respect to total polymeric solution weight. Polymer blends were stirred for 48 h, then left for degasification. Subsequently, polymer solutions were cast on a glass using a 250 μm casting knife, and instantly put into a MilliQ water coagulation bath. The membranes precipitated due to the solvent and non-solvent exchange between NMP and water, respectively. Resulting flat sheet membranes were removed from bath, washed for 24 hours in milliQ water and left to dry on air after the precipitation process. M0 should be referring for neat PSf membrane, whereas M2, M5 and M10 should be referring for membranes with 2, 5 and 10 wt.% of added UG20, respectively.

5.2.4 Characterizations

^1H NMR spectra of UG20 in deuterated methanol (CD_3OD) were recorded at 400 MHz on a Varian Gemini 400 spectrometer. A pulse delay time of 5 s was used. The solvent peak was taken as the reference, and the chemical shifts were given in parts per million from TMS (Tetramethylsilane) with the appropriate shift conversions.

The polysulfone membranes were characterized by ^1H NMR spectroscopy on a Varian Gemini 400 spectrometer (400 MHz). Membrane samples (10-20 mg) were dissolved in dimethylformamide (DMF) together with a known amount of potassium hydrogenphthalate (5-10 mg) as the internal standard for the quantification of residual N-methylpyrrolidone (NMP). Dimethyl sulfoxide- d_6 (dms- d_6), in a sealed co-axial capillary tube, was used as the deuterium reference external standard. The amounts of NMP were determined from the ratio of the NMP and potassium hydrogenphthalate signals (δ : 1.93 and 7.49 ppm, respectively) after baseline correction. For the determination of UG20 in M10 samples, a similar procedure was followed, but simply dissolving the membrane samples in dimethylformamide- d_6 (dmf- d_6).

The membrane surface morphology and roughness parameters were determined by Atomic Force Microscopy (AFM) – Molecular imaging model Pico SPM II (Pico+). The membrane surfaces were images in a scan size of 2 μm \times 2 μm . Roughness values were obtained from roughness analysis of 3D membrane images by means of WsxM software.

The glass transition temperatures of M0-M10 membranes was determined by Differential Scanning Calorimetry (DSC) by means of Mettler DSC-821e, calibrated using an In standard (heat flow calibration) and an In-Pb-Zn standard (T calibration). Samples of approximately 5 mg were tested in aluminium pans with a pierced lid in N_2 atmosphere with a gas flow of 50 mL/min. Tests were performed in dynamic mode

at a heating of 10°C/minute from 0°C to 200°C; T_g was determined as the inflection point in the heat flow signal step.

Dielectric thermal analysis (DETA) was used to provide information on the molecular structure of the membranes and molecular mobility. Impedance measurements were conducted using a Novocontrol Broadband Dielectric Impedance Spectrometer (BDIS), connected to a Novocontrol Alfa-A Frequency Response Analyzer. The measurements were obtained under isothermal conditions in the frequency range of 10⁻² to 10⁷ Hz, increasing the temperature in steps of 10 °C.

Raman spectra of the blended membranes were recorded by means of inVia™ confocal Raman microscope Renishaw (Agilent, Santa Clara, CA, USA). Raman spectra of UG20 additive, neat PSf and M10 membrane were obtained by a 785 nm excitation laser (10% Power) and a diffraction grating 1200 l/mm. The exposure time was 50 s and the objective x50 was used. The analysis was performed at different depth layers for each sample, i.e. top surface, center (50 and 100 μm deep) and bottom surface.

Fourier transform infrared spectroscopy (FTIR) analysis was performed using VERTEX 70 (Bruker, Billerica, Massachusetts, USA) in frequency ranging from 500 to 4000 cm⁻¹ for 32 scans. FTIR was employed to study the chemical composition as well as the possible hydrolysis of urea groups in our membranes. Each membrane (M0-M10) was analyzed as prepared without any previous treatment. Furthermore, we soaked membranes in KOH solution (0.64 M) for 24 h, and then analyzed them again to obtain spectra of aged membranes. Spectra were acquired with software OPUS 7.0 (Bruker Optics Inc., Ettlingen, Germany). Subsequently, we studied the effect of UG20 content increase on the chemical composition of the membrane in both, treated and untreated cases.

Specific surface areas and pore volumes were measured by N₂ physisorption at -196 °C by QUADRASORB SI surface analyzer, Quantchrome Instruments, equipped with FloVac Degasser, FloVac™. Samples were previously degassed in situ at 80°C overnight under vacuum. Surface areas were calculated using the Brunauer-Emmet-Teller (BET) methods over a P/P⁰ range where a linear relationship was maintained. Pore size distribution was predicted from the desorption wing of the isotherm by applying the BJH method. The membranes cross-sections obtained by cryofracture were examined by ESEM before and after degassing, in order to verify that degassification did not alter their inner structure.

A self-made, stainless-steel module, dead-end apparatus with an embedded membrane was used to measure the carbon dioxide permeance. The schematic of the gas permeation system is shown in Figure 5.2. Pure CO₂ and N₂ were injected into the module containing the membranes with an effective area of 16 cm². Gas permeation tests were conducted at 1, 2, and 3 bar, respectively, and measured by a precision gas

pressure sensor (stork solutions model: UPS-HSR-B02P5G). A mass transfer coefficient k (mol/s.m².bar) was calculated following the equation (1):

$$K = n/(A \cdot \Delta P) \quad (1)$$

Here, n stays for mass transfer (mol/s), A is membrane area (m²), and ΔP driving force pressure gradient (bar).

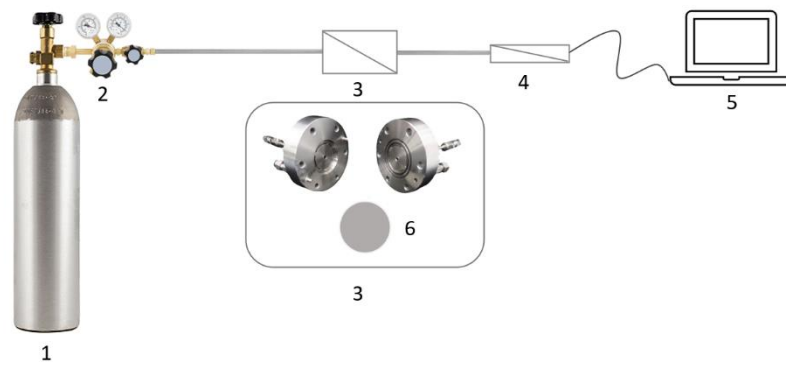


Figure 5.2. Permeability system: (1) N₂ or CO₂ gas tank, (2) Valve, (3) Steel module containing membrane, (4) Digital gas pressure sensor, (5) Computer, (6) Membrane.

The solubility of CO₂ in the blended membranes was investigated using the pressure depression method shown in Figure 5.2. The analyzed materials were placed in the module; carbon dioxide was injected into the system to reach 2 bar. When the pressure reached 2 bar, the valve was closed, and the pressure decrease was measured by a digital pressure sensor. The solubility of materials was calculated following the equation (2):

$$n = \frac{(p_i - p_f)V}{RT} \quad (2)$$

where n is the adsorbed moles of CO₂, p_i and p_f are the initial and final pressures (Pa), respectively, V is the gas volume of gas (m³), R is gas constant (8.314 J/K·mol), and T (K) is temperature. The solubility coefficient, S_{CO_2} (m³ (STP)/m³·atm), which are used to indicate the solubility of gases, is calculated according to equation (3):

$$S_{CO_2} = \frac{V_{CO_2m}(STP)}{V_m P_{established}} \quad (3)$$

where $V_{CO_2m}(STP)(m^3)$ is the volume of CO_2 relating to n_{CO_2} at STP conditions (1.013×10^5 Pa, 273.15 K), V_m is the analyzed material volume (m^3), and $P_{established}$ (atm) is the pressure measured at equilibrium conditions.

The direct air capture CO_2 absorption test was carried out in a gas-liquid membrane contactor, with home-made module as described in Figure 5.3 and [25]. The prepared membranes (9 cm^2) were placed in a module, where the top surface was exposed to ambient air by holes in the side of the module and the bottom surface of the flat sheet membrane is in contact with 100 mL of 0.64 KOH solution as a liquid absorbent in a different range of flow rate from 40 to 340 mL/min in room conditions ($25\text{ }^\circ\text{C}$ and 1.013×10^5 Pa). The experiments were conducted for 1h with continuous stirring, and each one was repeated three times to verify the reproducibility. After 1h, samples were collected, and the absorbed CO_2 amount was determined by means of a carbon dioxide ion-selective electrode (Hanna HI4105 connected with Thermo Scientific Orion Dual Star pH/ISE Benchtop meter, Thermo Scientific, Waltham, Massachusetts, USA).

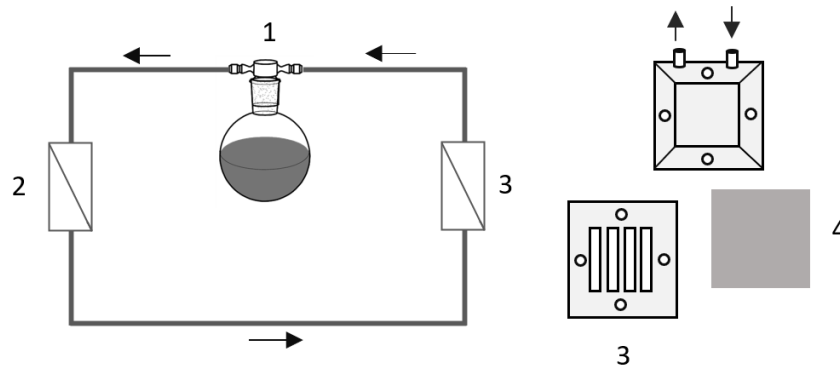


Figure 5.3 Direct air capture system for CO_2 absorption: (1) KOH solution tank, (2) Pump, (3) Module containing membrane, (4) Membrane.

Diluted sample (1 mL sample, 43 Milli-q water, 1mL standard (0.1 $NaHCO_3$)) was mixed with CO_2 buffer (5 mL) to adjust the pH to the electrode working pH at 4.8–5.2. The apparatus was set to auto-read mode, and the CO_2 concentration in the sample was measured. Results were interpolated from a standard curve obtained by Milli-q water, Standard (0.1M $NaHCO_3$), and Buffer). The stable value of CO_2 flux ($mol/m^2 \cdot s$), J_{CO_2} , was calculated following equation (4):

$$J_{CO_2} = \frac{Q_i \cdot M_{CO_2}}{A} \times 1000 \quad (4)$$

where Q_i is the absorbent flow rate (m^3/s), M_{CO_2} is the CO_2 concentration in the absorbent (mol/L) obtained from the measurements by the electrode, and A is the area of the flat sheet membrane (m^2).

Mechanical properties of all samples were analyzed using stress-strain measurement. Tensile measurements were performed via an Instron-5564 (Instron, MA, USA) instrument with a sample dimension of 10×50 mm, and a gauge length of 28 mm, at ambient atmosphere ($25^\circ C$, ~40% relative humidity), and a deformation rate of 5 mm/min.

Aging of the membranes was performed by soaking them in KOH 0.64 M solution under stirring for 24 h. After 24 h in KOH solution, the membranes were washed in distilled water under stirring for 30 minutes and dried at room temperature for 72h.

5.3 Results

5.3.1 Additive synthesis and blended membrane preparation and morphological characterization

Polyethylene imine, commercially named Lupasol G20, was previously mentioned to exhibit affinity with carbon dioxide due to the presence of highly basic nitrogen atoms. This can improve the performance of PSf-based membrane contactors to capture CO_2 . However, Lupasol G20 is a highly hydrophilic polymer, which represents a drawback when preparing the blended membrane in water coagulation bath. In addition, membrane stability could be affected when membranes are used in contactors with KOH solution. The bottom side of the membrane is in direct contact with an aqueous absorbent solution and some additive leakage can be expected due to Lupasol G20 hydrophilicity. Accordingly, we chemically modified Lupasol G20 with phenyl isocyanate to help decrease its water solubility and the same improve the membrane stability and selectivity. Moreover, the carrier capability is also improved as the chemical reaction with phenyl isocyanate converts some of the unhindered nitrogen atoms into sterically hindered by forming urea groups. The resulting reaction product was characterized by means of 1H NMR. The corresponding spectrum in deuterated methanol (CD_3OD) is reported in Figure 5.S1.

1H NMR of modified Lupasol (UG20) in deuterated methanol (Figure 5.S1) exhibited two groups of broad, partially overlapped signals, in the regions 6.5-7.8 (aromatic protons), 2.2-3.8 (ethylene protons adjacent to nitrogen atoms), thus showing that the chemical modification with phenyl isocyanate was successful [27]. According to Lupasol G20 structure, the ratio N:C corresponds to 1:2: therefore, each ethylene group approximately corresponds to one nitrogen atom. So, we could roughly estimate the ratio of

bonded aromatic groups (i.e. reacted phenyl isocyanate) vs. ethylene groups, i.e. aromatic groups/nitrogen atoms content, based on the integration of the aforementioned signals. This is directly related to the achieved modification degree, which resulted around 17%. Taking into account that the phenyl isocyanate amount used in the reaction corresponded to 25% of the cationic charge density of Lupasol G20, one can conclude that the chemical modification of the hyperbranched PEI occurred at good extent. Actually, this degree of modification reduced Lupasol G20 solubility in water sufficiently so to allow blended membrane preparation by phase inversion precipitation in water as desired. In our previous paper [26], Lupasol G20 turned out to be modified by benzoyl chloride at around 19%, yielding mG20 additive: therefore, UG20 and mG20 can be considered comparable in terms of grafting amounts.

Afterwards, UG20 was blended with PSf in different amounts, namely 2, 5, and 10 wt. % (Table 5.1), by dissolving both polymers in N-methylpyrrolidone (20 wt.% poly-mer/solvent) as described in the experimental part. Then, polymeric solutions were casted and immersed into a coagulation bath containing MilliQ water and subsequently washed in water for 24 hours, finally yielding flat sheet membranes (M2-M10), whose morphology was characterized by means of ESEM. The importance of carefully washing the membranes after their precipitation should be also underlined. When membranes were washed with water just for 30 minutes, 7-8 wt.% of residual NMP could be detected by ^1H NMR. Figure 5.S2 shows the ^1H NMR spectrum of M0 membrane washed for 30 minutes as a matter of example. In this spectrum, the peaks relative to residual NMP can be clearly distinguished and allowed the quantification of residual NMP after washing, by means of potassium hydrogen phthalate as internal standard. NMP acts as a plasticizer: actually, if one compares the glass transition temperatures of the membranes after 30 minutes and 24 hours washing, lower values were found in the former case (Table 5.3). Careful ^1H NMR analyses of washed samples assured that 24 hours were a sufficient time to completely remove NMP from the prepared membranes.

The composition and morphological characteristics of the membranes under study are shown in Table 5.1.

Table 5.1 Composition and morphological characteristics of studied membranes.

Membrane	UG20/PSf (wt. %)	Thickness (μm)	Surface Area (m^2/g)
M0	0	142 ± 1	27.4
M2	2	146 ± 5	28.2
M5	5	137 ± 4	12.5
M10	10	150 ± 4	6.3

Environmental scanning electron microscope (ESEM) was used to characterize the membrane morphology, in which membrane thicknesses were determined by ESEM micrographs by means of ImageJ software. Thickness values were taken as the average of three measurements and are reported in Table 5.1.

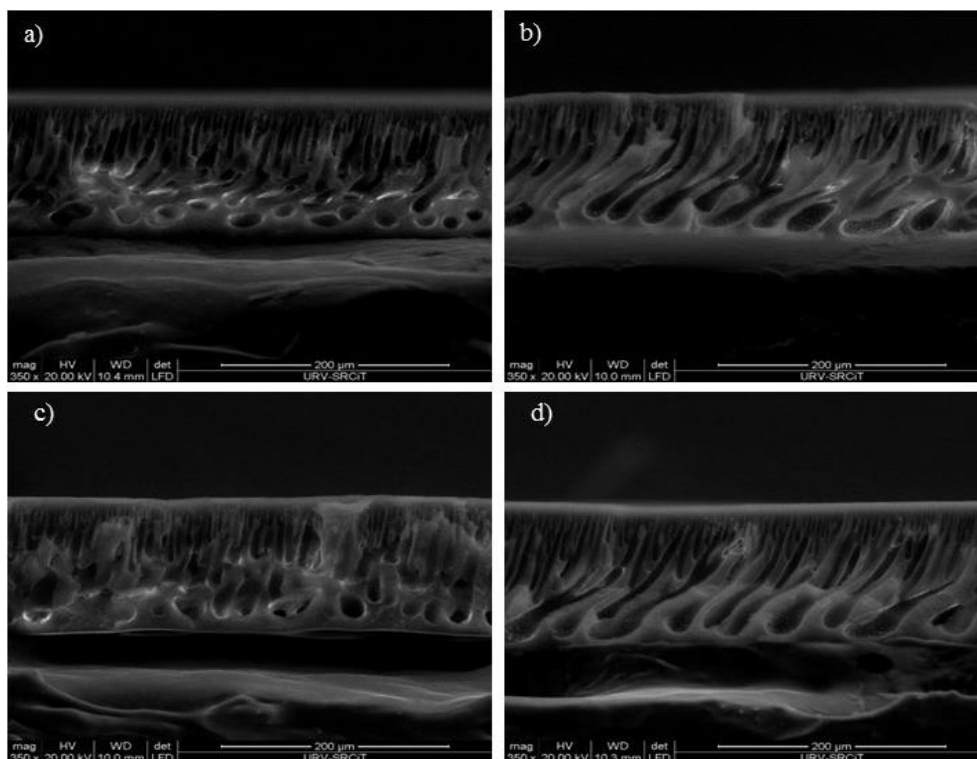


Figure 5.4 Environmental scanning electron microscope (ESEM) images of the cross-section of studied membranes: (a) M0; (b) M2; (c) M5; (d) M10.

Thickness values range around 140-150 μm . Figure 5.4a-d show the cross-sectional images of M0, M2, M5 and M10 membranes. ESEM could not clearly evidence porosity changes when UG20 additive content increases, i.e. a similar morphology can be noticed, which reveals the same finger-like structure for pores with a spongy and denser layer on the bottom. The amount of macrovoids looks the same as we increased UG20 content. Macrovoids can be explained as a consequence of the instantaneous demixing that occurs when the casting solution and the coagulant get in contact and they are associated with instantaneous precipitation and lower viscosity of the polymeric solution [28]. This leads to a fast penetration of water, as a non-solvent, into the polymeric solution. This phenomenon determines highly asymmetric structures, with finger-like macrovoids; on the other hand, slower coagulant penetration induces slower precipitation and finally forms sponge-like, more symmetric structures [29]. Furthermore, it has been also shown that the evolution from a spongy-like to a macrovoid morphology also depends on the membrane thickness; a full development of a finger-like structure can be observed when thickness is higher than a critical value, which varies according to the whole system composition [30]. In our case, membrane thicknesses all lie within

140 and 150 μm approximately (Table 5.1), which should lead to finger-like morphologies. On the other hand, since UG20 is a hydrophilic polymer, it should contribute to slower the precipitation of PSf-based membranes, and therefore should lead to a less porous structure. Also, one should remember that the solution viscosity also plays a role in the phase inversion process, since it may alter the precipitation rate and, consequently, membrane morphology. Therefore, the higher the additive content, the higher the difference in the solution viscosity, which could slow down the miscibility of polymeric solution and water. In our previous paper [26], when the used additive was Lupasol G20 modified with benzoyl chloride at similar extent (mG20), we could find a remarkable effect of the additive content on membrane morphology just in the case of 20 wt.% additive amount; nevertheless, some evidence of a growing dense layer were already shown by the sample containing 10 wt.% additive. However, for that system, in the absence of a more exhaustive analysis of porosity, a change in morphology with additive increase could not be ruled out.

Therefore, in order to get further insight into membrane porosity of M0-M10 systems, nitrogen adsorption and desorption isotherms were determined and analyzed. Table 5.1 shows acquired cumulative BET surface area, while Figure 5.5 depicts cumulative pore volume for M0-M10 membranes.

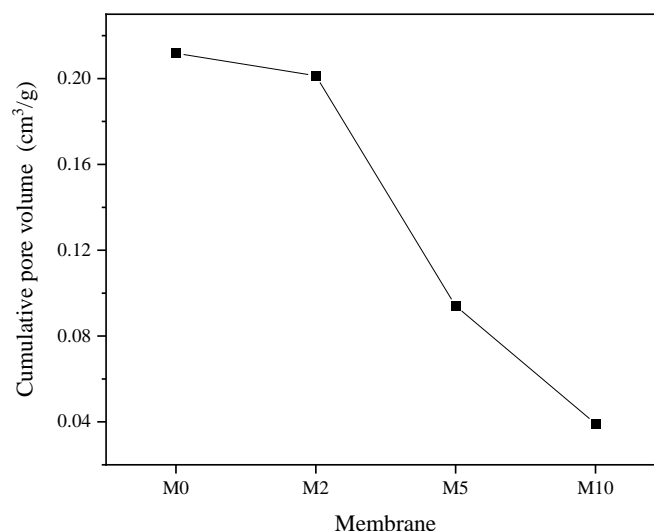


Figure 5.5 Cumulative pore volume of M0-M10 membranes.

The adsorption isotherms of these samples were mainly of type II corresponding to non-porous materials, with some hysteresis loop, which also envisages some macro- or mesoporosity [31]. Therefore, a wide range of size and shapes can be expected. As a matter of example, Figure 5.S3 shows the adsorption isotherms of M0 and M10.

As expected from ESEM images, a wide range of pore size could be evidenced, ranging between 15 and 4000 \AA approximately. From Table 5.1 and Figure 5.5, it can be noticed that the addition of 2%

UG20 (M2 sample), does not significantly alter neither the total pore volume and nor the surface area with respect to M0. On the other hand, as a general trend, the presence of increasing amounts of additive (M5 and M10 samples) determines a general decrease of porosity and porous surface area. As for the pore volume distribution in the final membranes, Figure 5.S4 shows the full range for the whole set of membranes, while Figure 5.6 reports the zoom corresponding to pore radii between 0 and 150 Å, i.e. covering micro- and mesoporosity ranges, for M0, M5 and M10 samples.

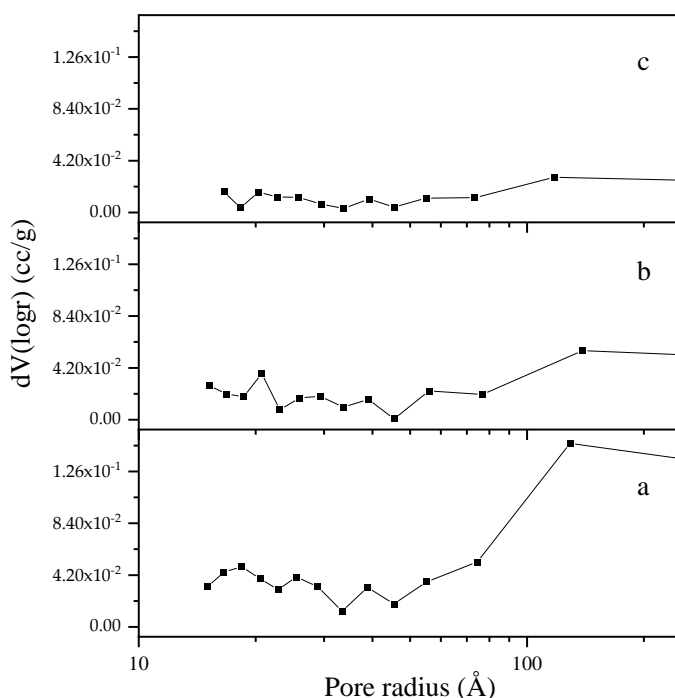


Figure 5.6 Pore volume distribution zoomed between 0 and 250 Å of: (a) M0; (b) M5; (c) M10.

In general, one can see that increasing addition of UG20 (M5 and M10 samples), displaces the distribution of pore size towards lower values (Figure 5.6 and Figure 5.S4). This can be attributed to a progressive delayed demixing which occurs when the concentration of UG20 increases, probably as a consequence of different affinity for the coagulant and increased viscosity of the blended polymeric solution.

PSf-based membranes were characterized in terms of surface morphology and stability tests. Both water contact angle and swelling tests were performed in order to investigate the effect of UG20 content on the wettability of blended membranes compared to neat PSf. RMS roughness was investigated on the bottom side of membranes, since in membrane contactors, the bottom side of membranes is in direct contact with the absorbent aqueous solution. The RMS roughness parameters of bottom side of M0-M10 membranes were determined from three-dimensional topographic images seen in Figure 5.S5a-d. Table 5.2

reports the bottom side RMS roughness, water contact angle values and water and KOH (0.64 M solution) uptake of the membranes.

Table 5.2 RMS roughness of bottom side, water contact angle, Water uptake (WU) and KOH (0.64 M solution) uptake of the studied membranes.

Membrane	Bottom RMS roughness (nm)	Top CA (°)	Bottom CA (°)	WU (%)	KOH uptake (%)
M0	10.8	76±3	69±3	0.6±0.2	1.5±0.1
M2	10.6	67±2	72±1	2.3±0.3	2.3±0.2
M5	11.4	68±3	67±2	7.4±0.2	4.4±0.6
M10	15.6	64±2	67±2	10.4±0.6	9.4±0.4

Membrane wettability was investigated by means of water contact angle measurements. When UG20 is present in the blended membranes (samples M2-M10), within the experimental error, the contact angle values slightly decrease on the top of the membrane with respect to neat PSf (sample M0), while they keep practically constant on the bottom side of the membrane. Initially, this could suggest that UG20 is more prominent on the top side of the membrane due to more hydrophilic character of the additive with respect to PSf. As for surface morphology, we determined the RMS roughness from AFM topographic images, shown in Figure 5.S5, of the membranes' bottom side, which is directly in contact with the alkaline solution in the CO₂ capture device. A slight increase in RMS roughness was observed for the membranes containing higher amounts of UG20, i.e. M5 and M10; nevertheless, it does not seem to affect significantly the CA values of the corresponding samples.

As shown in Table 5.2, when UG20 content increases, both water uptake (WU) and KOH uptake of blended membranes tend to increase as well, as expected due to the more hydrophilic character of UG20 additive. Higher WU and KOH uptake can be intrinsically related to a lower absorption flux. Indeed, penetration of liquid into the membrane can negatively affect gas diffusivity and provoke pore clogging. This effect is visible when working in membrane contacting system with KOH solution as absorbent. Nevertheless, WU and KOH uptake of M2-M10 samples are much lower compared to PSf membrane additivated with mG20 additive previously reported [26], which suggests better performances.

5.3.2 Additive distribution and membranes' chemical stability

In order to get insight into the distribution of UG20 additive in PSf membranes, first we checked their Raman spectra, obtained by a 785 nm excitation laser, across the section between 200 and 2000 cm⁻¹. Figure 5.S6 shows the Raman spectra registered on top surface of M10 membrane, pure UG20 additive and

neat PSf membrane (M0). Different bands can be attributed to the additive, without overlapping those of neat PSf membrane. The 1030 cm^{-1} band in Figure 5.S6(a) can be attributed to the C-N stretch for secondary and tertiary aliphatic amines that is suggested to be a shoulder in the M10 Raman spectrum [32,33]. On the other hand, the shoulder at 1651 cm^{-1} is typical for urea compounds, and it is related to C=O stretching in urea (Amide-I region). Unfortunately, this shoulder found in UG20 spectrum (as seen in Figure 5.S6(a)) is not visible in M10 spectrum (Figure 5.S6(b)), that is the membrane with the highest additive content. This is probably due to the low content of UG20 in the membrane and detection limits. Similarly, no differences could be detected when M10 membrane was studied at different depth layers, namely top surface, center (50 and $100\text{ }\mu\text{m}$) and bottom surface. Figure 5.S7 in shows the Raman spectra of different layers (Top, center and bottom) in M10 membrane; all the peaks can be overlapped. Therefore, we could not determine the exact distribution of UG20 throughout the blended membranes.

Since the additivated membranes were prepared to be used in contact with 0.64 M KOH solution in the direct air capture device, it is convenient to study their stability to the alkaline environment. PSf is well known for its excellent chemical stability in alkaline environment [34]: therefore, the chemical stability and good performance of M2-M10 membranes are essentially determined by the stability of the contained UG20 additive.

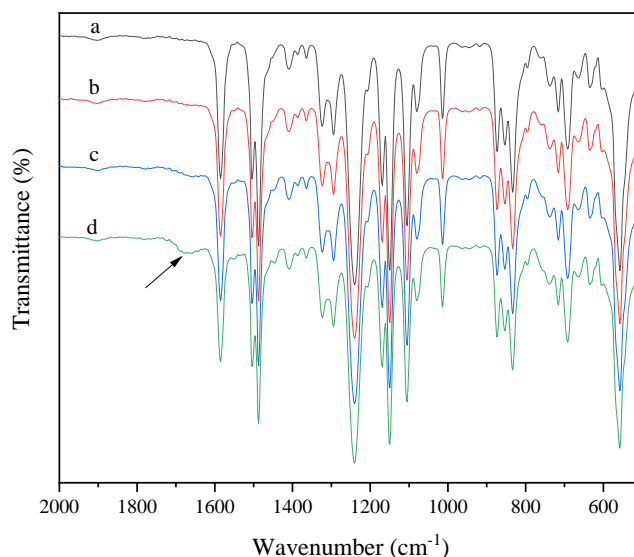


Figure 5.7 Infrared spectra between 500 and 2000 cm^{-1} of: (a) M0; (b) M2; (c) M5; (d) M10. The band around 1660 cm^{-1} is highlighted.

Figure 5.7 shows the FTIR spectra between 500 and 200 cm^{-1} of M0-M10 membranes. The broad band highlighted by an arrow around 1660 cm^{-1} in Figure 5.7d can be attributed to the C=O stretching in

urea. This band is more visible and prominent as UG20 additive content increases, i.e. in M10 which is the membrane with the highest UG20 content. Therefore, the study of stability was focused on M10 sample.

Figure 5.8 depicts the FTIR spectra between 1000 and 2000 cm^{-1} of (a) fresh M10, (b) M10 after soaking 24 hours in 0.64 M KOH and (c) UG20 additive.

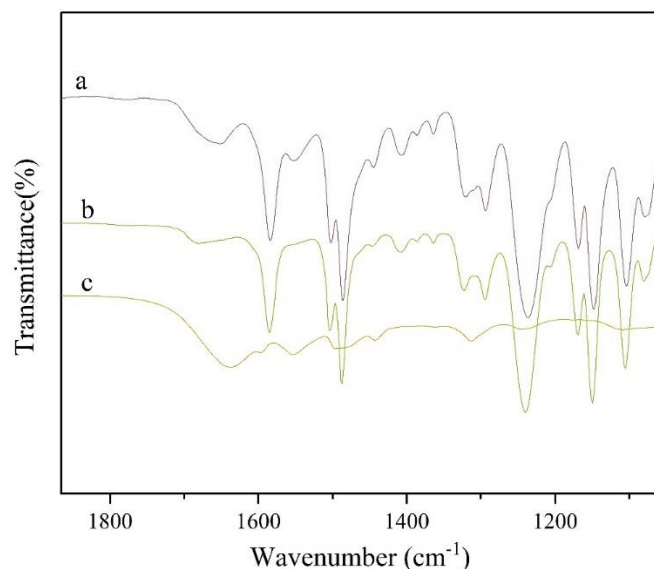


Figure 5.8 FTIR spectra between 1000 and 2000 cm^{-1} of (a) fresh M10, (b) M10 after soaking 24 hours in 0.64 M KOH and (c) neat UG20 additive.

If we focus our attention on the broad band around 1660 cm^{-1} , characteristic of C=O stretching of urea in neat UG20 (c), and compare the M10 before (a) and after soaking in KOH solution (b), we cannot find a great difference, though one could guess a slight displacement of this band towards higher wavenumbers for the sample submitted to the alkaline environment. This could be indicative of some hydrolysis of urea bond in this strong alkaline conditions. However, no clear conclusions could be drawn from this experiment. For this reason, we decided to check the stability of additivated M10 by ¹H NMR.

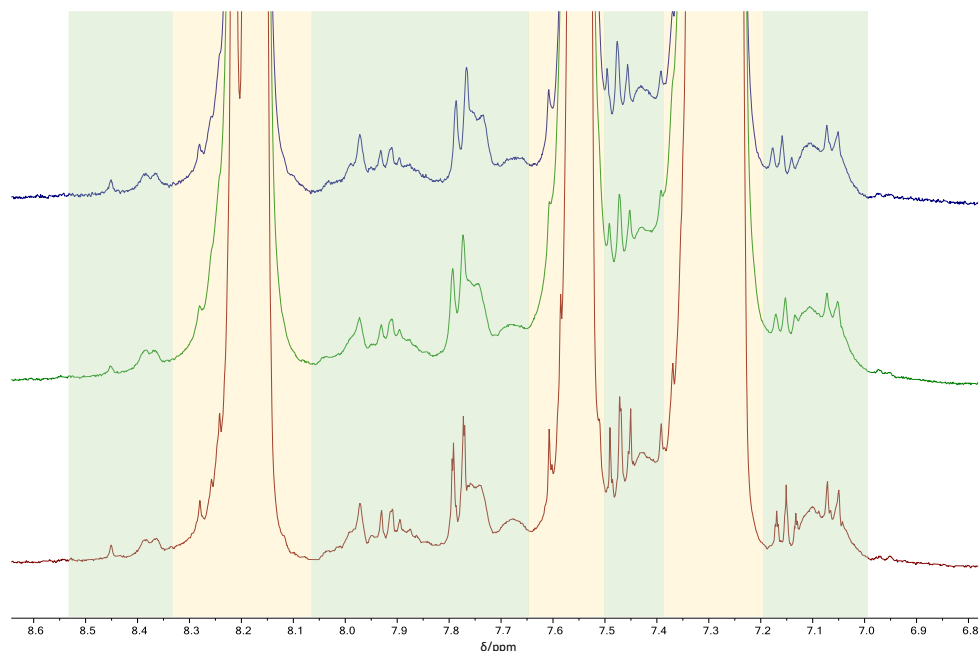


Figure 5.9 Stacked ¹H NMR spectra (in dmf-d₆, 400 MHz) between 6.8 and 8.7 ppm of M10 samples: as-prepared (red trace), after treatment 24 hours in 0.64 M KOH solution and following washing (green trace) and after treatment in water (blue trace). Green- and yellow-shaded areas indicate the regions of additive and polysulfone signals, respectively.

Figure 5.9 shows the ¹H NMR spectra of M10 samples, as-prepared (red trace), after treatment in 0.64 M KOH solution followed by washing in water (green trace), and after treatment in water for 24 hours (blue trace). In more detail, the region between 6.8 and 8.6 ppm, corresponding to the aromatic protons, is shown. Thanks to the comparison with the ¹H NMR spectra of UG20 additive alone and M0 sample, we could assign the regions 7.2-7.4, 7.5-7.65 and 8.05-8.35 to the signals from PSf protons, while the other ones were attributed to UG20 protons. No apparent changes in the additive signals could be evidenced after soaking in 0.64 M KOH for 24 hours, which qualitatively suggested UG20 stability under this treatment conditions. Indeed, upon hydrolysis of urea and subsequent membrane washing, the originally grafted groups as well as the hydrolyzed UG20 should be washed out of the membrane and the amount of UG20 protons versus PSf protons should decrease in the ¹H NMR spectrum. In the three samples, quantification of the additive signals was performed by comparing the integration of the additive signals between 8.06-7.82 ppm with the integral of the singlet at 1.88 ppm, characteristic of PSf methyl group (Figure 5.S8). The ratio between the additive and the reference PSf areas gave the same value in all cases, within the experimental sensitivity: thus, no additive hydrolysis could be detected in the membrane under the tested conditions. In addition, one should take into account that stability was tested in such harsh conditions as completely soaking M10 in the capture solution while, in the CO₂ capture device, only the membrane

bottom surface is in contact with it. Therefore, we could reasonably conclude that the membranes containing the additive are expected to exhibit good stability in service.

5.3.3 Mechanical characterization

Table 5.3 shows the tensile modulus, strain at break and ultimate strength of M0-M10 membranes; their glass transition temperatures after 24 hours ($T_{g,d}$) and 30 minutes ($T_{g,NMP}$) washing and subsequent drying are also reported.

Table 5.3 Mechanical properties and glass transition temperatures of M0-M10 membranes.

Membrane	E (MPa)	Ultimate strength (MPa)	Strain at break (%)	$T_{g,d}^1$ (°C)	$T_{g,NMP}^2$ (°C)
M0	372±64	3.0±0.7	5.0±1.3	178±1	112±2
M2	304±30	2.8±1.4	5.8±2.0	171±1	105±1
M5	261±27	2.0±0.5	5.8±1.2	139±2	116±1
M10	221±31	1.7±0.3	6.4± 1.4	133±2	120±3

¹ After 24 hours washing in water and drying; ² after 30 minutes washing in water and drying.

Table 5.3 shows that the presence of the additive determined a plasticizing effect, as demonstrated by the decrease of tensile modulus and tensile strength; moreover, the strain at break increased with UG20 content, thus indicating a more plastic deformation. This suggested increased mobility of polymeric chains, which could be favorable to gas permeation. On the other hand, one should observe that the differences in porosity do not seem to affect the mechanical behavior, despite macrovoids and pores could act as weak points under an applied force [35]. Conversely, in our case the plasticizing effect of the additive seems to predominate over the porosity decrease going from M0 to M10.

As previously discussed Section 5.3.1, the comparison between Tgs of the membranes after washing in water for 30 minutes ($T_{g,NMP}$) and for 24 hours ($T_{g,d}$), suggested that prolonged washing is necessary in order to completely remove residual NMP after phase inversion precipitation.

Figure 5.10 displays the dielectric relaxation spectra of M0, M2 and M10 samples in terms of the loss factor (ϵ'') at 1 Hz of frequency in the temperature interval of -150°C to 250°C.

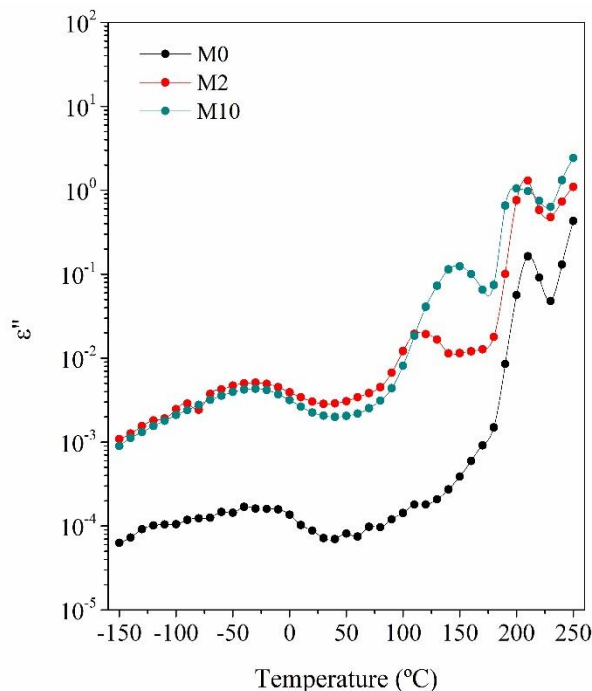


Figure 5.10 Loss factor (ϵ'') versus temperature at 1 Hz of frequency for M0, M2 and M10 membranes.

Three complex relaxation zones γ , β and α , with increasing temperature order are observed, corresponding to molecular motions of both polysulfone and the modified hyperbranched polyethylene imine UG20. The loss factor is higher for the M2 and M10 membranes than M0, which would indicate a greater mobility of the molecular chains of the mixed membranes. This suggests that the additive imposes fewer restrictions on molecular movement by increasing the number of chains that can move, therefore facilitating the ability of the membrane to diffuse CO_2 . The relaxation zone γ appears at low temperatures between -150°C and 50°C , and the loss factor is independent of the additive concentration. At higher temperatures, between 120°C and 250°C , the most prominent relaxations are αPEI , αPSU , in increasing order of temperature: they arise from the motion of the main chains of PSU and PEI, respectively. The temperature of αPSU relaxation peak around 210°C slightly decreases with the concentration of additive, whereas the most significant differences are observed in the αPEI relaxation. The temperature of this relaxation increases with the concentration of additive, being equal to 120°C and 150°C for M2 and M10, respectively. These first results confirm the plasticizing effect of UG20 as determined by mechanical tests and DSC. However, a more detailed analysis of the dielectric spectra of these membranes has been performed and it is the object of a forthcoming paper.

5.3.4 CO₂ capture performance

Figure 5.11 shows the solubility of CO₂ in M0-M10 membranes. As expected, CO₂ solubility increases with UG20 content, according to the high affinity of the additive to carbon dioxide due to the presence of basic nitrogen atoms which can favorably interact with this molecule. The grafting reaction performed on Lupasol G20 partially reduces the amount of amine nitrogen atoms available for carbon dioxide capture. Nevertheless, UG20 additive is expected to exhibit higher CO₂ solubility with respect to the previously reported mG20 additive [26]: indeed, the reaction between Lupasol G20 and phenyl isocyanate (Scheme 5.2) leads to the formation of urea groups, while amides are formed in the case of reaction with benzoyl chloride (mG20). This means that, as regards the grafted groups, UG20 contains double amount of nitrogen atoms than mG20; in addition, urea nitrogen atoms are expected to have more affinity to CO₂ than the amide ones. Therefore, higher carbon dioxide solubility can be expected in the UG20 containing membranes when comparable amounts of additive are considered.

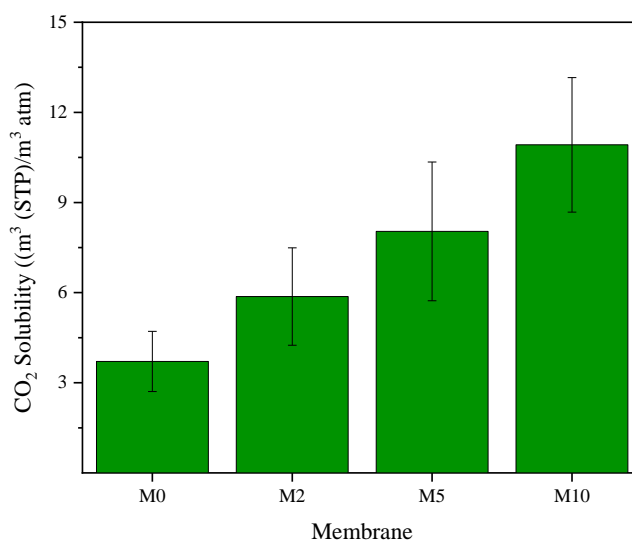


Figure 5.11 CO₂ solubility in M0-M10 membranes determined by the pressure decay method at 2 bar.

We performed permeability tests to calculate the mass transfer coefficients, k , for the M0-M10 membranes series. The role of chemical composition in the gas permeability of these membranes was checked by determining k from CO₂ as well as from N₂ permeation. The results are shown in Figure 5.12. The inset in Figure 5.12 depicts carbon dioxide selectivity over nitrogen, calculated as the ratio of their respective mass transfer coefficients.

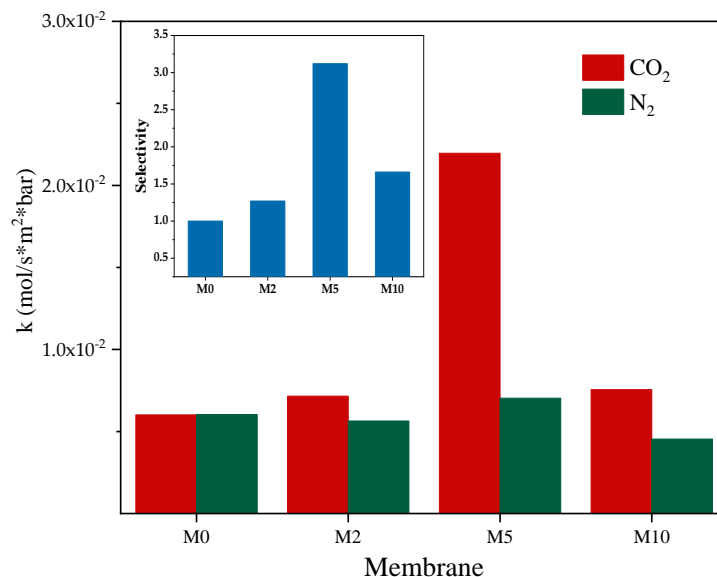


Figure 5.12 Mass transfer coefficient k as calculated from CO_2 (red bar) and N_2 (green bar) permeation through M0-M10 membranes. In the inset the corresponding selectivities calculated as $k_{\text{CO}_2}/k_{\text{N}_2}$ are shown.

As shown in Figure 5.12, when the full composition range is examined, in general k for carbon dioxide increases with increasing amount of UG20, while no clear trend can be found in the case of nitrogen. Selectivity to carbon dioxide versus nitrogen (Inset of Figure 5.12) is approximately 1 in the case of M0, while it turns higher than unit on UG20 addition. This suggests that the permeation of these gases does not only depend on the ratio between membrane pores and molecular size of gases, but also on the chemical composition, that is, it is not exclusively ruled by physical parameters. In particular, it must be noticed that the mass transfer coefficient for CO_2 reaches a maximum in correspondence to M5 sample and then considerably decreases for M10, though, it still exhibits a higher value than M2. Correspondingly, CO_2 selectivity exhibits the highest value for M5 sample and afterwards decreases. In order to explain this behaviour, we should consider that different factors are involved in the gas transport of these systems.

In general, polymeric membranes are non-porous materials and gas permeation through them can be described by the solution-diffusion mechanism [36]. On the other hand, the membranes under investigation are asymmetric and present several ranges of pore size (Figure 5.6 and Figure 5.S4), lying in macro-, meso- and microporosity range. Selectivity will be therefore determined mainly by the denser layer, whose thickness, in the case of M0-M10 membranes, could not be clearly determined. The selectivity can be split into a solubility selectivity and a diffusivity selectivity: therefore, it can be ascribed to a difference in both properties [37]. When we consider these two factors, the former depends on the gas affinity to the membrane material and its condensability, while the latter can be ascribed the free volume and random motion of the polymeric chains. Typically, diffusivity increases with decreasing the gaseous molecule

kinetic diameter and increasing the polymer free volume. Since the CO₂ and N₂ kinetic diameters are 0.330 nm and 0.364 nm, respectively, the former is favored as regards diffusivity selectivity; moreover, gas condensability increases with its critical temperature, which is 304.1 K in the case of CO₂ and 126.2 K for N₂ [38]. Summing up, in general permeability of CO₂ is favored over N₂. On the other hand, we found that the mass transfer coefficient of CO₂ increases considerably upon addition of UG20 as expected, since CO₂ solubility increases (Figure 5.11); nevertheless, it reaches a maximum in correspondence to M5 and then decreases. This trend suggests that two factors, acting in opposite directions, contribute to CO₂ permeation and reach the best balance in M5 sample. As for solubility, it increases with UG20 amount: so, it should contribute to increasing permeability of M10 over M5. This suggests that the explanation of the observed experimental trend of the mass transfer coefficients needs to be sought in the diffusivity factor. Dielectric analysis shown in Figure 5.10 demonstrated that the dielectric loss factor is higher for the M2 and M10 membranes than M0, which would indicate a greater mobility of the molecular chains of the additivated membranes; indeed, their T_{gs} decrease on increasing UG20 amount (Table 5.3). This, in turn, is expected to improve diffusivity. Nevertheless, BET analysis showed that porosity is strongly reduced on UG20 addition and exhibits the lowest value in the case of M10. As a final remark, we should also take into account that, given the strong asymmetry of these membranes, the thickness of the dense layer could not be exactly determined and could be much higher in the case of M10, thus improving membrane resistance to permeant diffusion.

Absorption performance of M0-M10 was evaluated for potassium hydroxide solution in a flat sheet membrane contactor (FSMC) in cross flow module at different liquid flow rates. Figure 5.13 shows the results in terms of carbon dioxide flux versus absorbent flow rate.

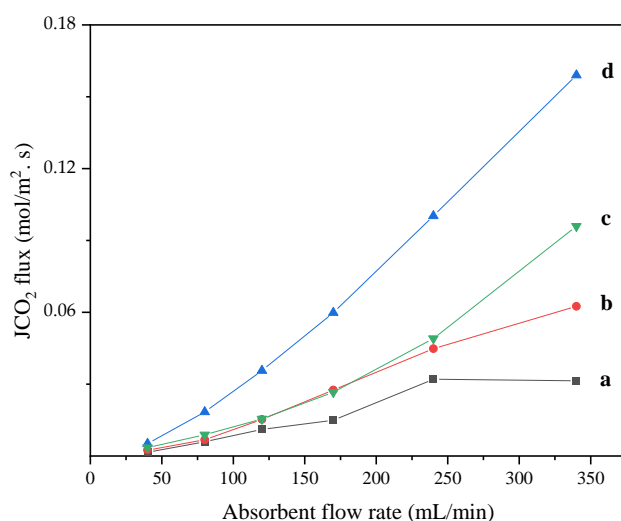


Figure 5.13 CO₂ absorption flux into M0–M10 membranes in direct air capture tests as a function of liquid absorbent (0.64 M KOH) flow rate: (a) M0; (b) M2; (c) M10; (d) M5.

From Figure 5.13, one can see that CO₂ absorption from ambient air exhibits similar values for all the membranes under investigation at the lowest absorbent flow rate (35 mL/min). In the mass transfer process between gaseous and liquid streams through a porous membrane, the resistance can be expressed as three terms: liquid side, gas side and membrane mass transfer resistances [39]. In our case, the effect of gas side resistance can be neglected, since we used ambient air as CO₂ source: as a consequence, gas concentration was constant in all our experiments. So, the total mass transfer resistance at low liquid flow rate is mainly affected by the resistance term related to the liquid side. This can explain very similar gas absorption flux at low liquid absorbent flow rate for M0-M10 membranes, as shown in Figure 5.13. However, when the absorbent flow rate was increased (120-340 mL/min), we found remarkable differences that can be explained in terms of the different UG20 additive content; in more detail, the behavior of the membrane with 5% additive amount (M5) is the most efficient while the membrane containing 2 and 10% additive, respectively, behave similarly: that is, UG20 amount higher than 5% does not improve the membrane performance any more, though it gives better CO₂ capture than neat PSf (M0). In general, on increasing the liquid flow rate, the liquid side mass transfer resistance decreases and eventually, above a certain flow rate, the mass flux is mainly influenced by the membrane resistance. At this point, absorption flux versus liquid flow rate reaches a plateau. In our case this situation is clearly shown just by M0. As for the additivated membranes, the trend of CO₂ absorption flux is the same as the one we found for mass transfer coefficient, i.e. M5 exhibits the best performance, outperforming the results of previous membranes with less stable amide-functionalized additives such as mG20 [26].

On the other hand, we should also consider the increase in membranes' wettability and water uptake as a consequence of UG20 addition, which can favor the penetration of KOH solution into the membrane, thus provoking membrane clogging and negatively affecting gas diffusivity. At the bottom side of the membranes in the contactor, where CO₂ as a permeant gets in touch with the aqueous solution of KOH, the absorption reaction produces an aqueous solution of K₂CO₃; on the other hand, when CO₂ is in excess, the undesired production of more insoluble KHCO₃ can occur. Consequently, pores may be clogged and the pore volume decreases. Indeed, Figure 5.14a shows the ESEM image of bottom surface of M10 after CO₂ absorption test, which puts into evidence very nice hexagonal crystals layered onto the polymeric surface. By means of EDX and XRD analyses, these crystals could be identified as KHCO₃.

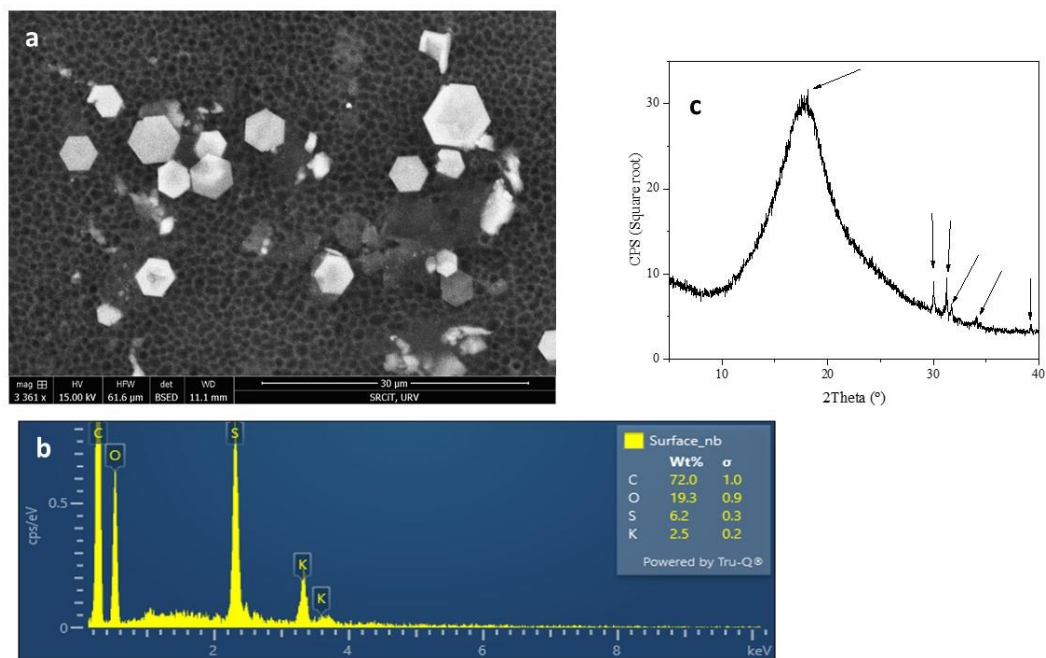


Figure 5.14 (a) ESEM image of M10 bottom surface; (b) EDX analysis of bottom surface observed by ESEM; (c) XRD pattern of M10 bottom surface; the arrows evidence the crystalline peaks which overlap with the pattern of crystalline KHCO_3 .

On comparing the performance of M2-M10 membranes in the contactor, with the analogous ones additivated with mG20 [26], in general higher values of the flux were found. The optimum CO_2 absorption flux achieved with M5 was above $150 \text{ mmol}(\text{CO}_2)/\text{m}^2\cdot\text{s}$, largely surpassing previous results for mG20, and almost four times higher than the rate of CO_2 uptake by natural stomata in plant leaves [25]. This can be ascribed to the higher values of CO_2 permeability, in combination with lower water and KOH uptake, which can determine lower pore clogging. The enhancement in hydrophobicity and chemical stability of the urea-modified additive UG20 as compared to the amide-functionalized analogue mG20, are key for the high direct air capture efficiency and robustness observed.

5.4 Conclusions

We investigated the behavior of asymmetric Polysulfone membranes prepared via phase-inversion precipitation with the addition of UG20 additive, based on hyperbranched Lupasol G20 grafted with phenyl isocyanate. Membranes were prepared by blending PSf with UG20 amount between 2 and 10 wt.10%, with the aim to increase their ability for carbon dioxide capture at ambient pressure. In all cases the resulting morphology showed finger-like macropores together with meso- and micropores as well as a dense layer.

However, porosity decreased on increasing the additive content, probably as a consequence of delayed demixing during phase inversion precipitation. The presence of the additive determined an increase of water and KOH uptake with respect to neat PSf. However, no degradation upon 24 hours soaking in KOH solution could be detected neither by FTIR nor ^1H NMR. Mechanical, thermal and dielectric analysis showed a plasticizing effect of the additive, which could favor gas permeation. On the other hand, CO_2 solubility was remarkably increased as a consequence of UG20 addition. Nevertheless, the CO_2 mass transfer coefficient improved up to 5% additive, while was reduced in 10% UG20 sample, probably due to the porosity decrease which acted in reverse to the increased solubility. Finally, when we evaluated the performance of these membranes in the CO_2 capture device, we found a remarkable improvement in comparison with neat PSf; the capture behavior showed the same trend as the mass transfer coefficient, i.e. the best performance was obtained in the case of 5% UG20. In general, the use of UG20 as an additive determined better characteristics in terms of CO_2 permeability and capture when compared with the additive mG20 previously reported.

5.5 References

1. Herzog, H.; Eliasson, B.; Kaarstad, O. Capturing greenhouse gases. *Scientific American* 2000, 182, 72-79.
2. Kharseh, M.; Altorkmany, L. How global warming and building envelope will change buildings energy use in central Europe. *Appl Energy* 2012, 97, 999-1004.
3. G.A. Meehl, T.F.S., W.D. Collins, P. Friedlingstein, A.T. Gaye, J.M. Gregory, A. Kitoh, R. Knutti, J.M. Murphy, A. Noda, S.C.B. Raper, I.G. Watterson, A.J. Weaver and Z.-C. Zhao Global Climate Projections. In: *Climate Change 2007: The Physical Science Basis. Contribution of Working Group I to the Fourth Assessment Report of the Intergovernmental Panel on Climate Change*. 2007.
4. Salazar Duarte, G.; Schürer, B.; Voss, C.; Bathen, D. Adsorptive Separation of CO_2 from Flue Gas by Temperature Swing Adsorption Processes. *ChemBioEng Reviews* 2017, 4, 277-288, doi:<https://doi.org/10.1002/cben.201600029>.
5. Bazhenov, S.D.; Bilyukevich, A.V.; Volkov, A.V. Gas-Liquid Hollow Fiber Membrane Contactors for Different Applications. *Fibers* 2018, 6, 76.
6. Zhao, S.; Feron, P.H.M.; Deng, L.; Favre, E.; Chabanon, E.; Yan, S.; Hou, J.; Chen, V.; Qi, H. Status and progress of membrane contactors in post-combustion carbon capture: A state-of-the-art review of new developments. *Journal of Membrane Science* 2016, 511, 180-206, doi:<https://doi.org/10.1016/j.memsci.2016.03.051>.

7. Rao, A.B.; Rubin, E.S. A Technical, Economic, and Environmental Assessment of Amine-Based CO₂ Capture Technology for Power Plant Greenhouse Gas Control. *Environmental Science & Technology* 2002, 36, 4467-4475.
8. Rahbari-Sisakht, M.; Ismail, A.F.; Rana, D.; Matsuura, T.; Emadzadeh, D. Carbon dioxide stripping from water through porous polysulfone hollow fiber membrane contactor. *Separation and Purification Technology* 2013, 108, 119-123.
9. Rahbari-Sisakht, M.; Ismail, A.F.; Rana, D.; Matsuura, T. Effect of novel surface modifying macromolecules on morphology and performance of polysulfone hollow fiber membrane contactor for CO₂ absorption. *Separation and Purification Technology* 2012, 99, 61-68.
10. Witek-Krowiak, A.; Dawiec, A.; Modelski, S.; Podstawczyk, D. Carbon Dioxide Removal in a Membrane Contactor-Selection of Absorptive Liquid/Membrane System. *Int. J. Chem. Eng. Appl.* 2012, 3, 391-395.
11. Hafeez, S.; Safdar, T.; Pallari, E.; Manos, G.; Aristodemou, E.; Zhang, Z.; Al-Salem, S.M.; Constantinou, A. CO₂ capture using membrane contactors: a systematic literature review. *Frontiers of Chemical Science and Engineering* 2021, 15, 720-754, doi:10.1007/s11705-020-1992-z.
12. Scholes, C.A.; Chen, G.Q.; Stevens, G.W.; Kentish, S.E. Journal of Membrane Science: Plasticization of ultra-thin polysulfone membranes by carbon dioxide. *Cellular Polymers* 2010, 29, 71.
13. Afsari, M.; Kheyrieh, S.; Asghari, M. Application and modification of polysulfone membranes in wastewater treatment - A review. *Reviews in Chemical Engineering* 2017.
14. Sanders, D.F.; Smith, Z.P.; Guo, R.; Robeson, L.M.; McGrath, J.E.; Paul, D.R.; Freeman, B.D. Energy-efficient polymeric gas separation membranes for a sustainable future: A review. *Polymer* 2013, 54, 4729-4761, doi:<https://doi.org/10.1016/j.polymer.2013.05.075>.
15. Kheyrieh, S.; Asghari, M.; Afsari, M. Application and modification of polysulfone membranes. *Reviews in Chemical Engineering* 2018, 34, 657-693, doi:doi:10.1515/revce-2017-0011.
16. Kianfar, E. Experimental Study on Chemical Carbon Dioxide Absorption Using Porous Polysulfone Gas-Liquid Hollow Fiber Membrane Contactor System. *American Journal of Oil and Chemical Technologies* 2015, 3, 1-12.
17. Bernhardsen, I.M.; Knuutila, H.K. A review of potential amine solvents for CO₂ absorption process: Absorption capacity, cyclic capacity and pKa. *International Journal of Greenhouse Gas Control* 2017, 61, 27-48, doi:<https://doi.org/10.1016/j.ijggc.2017.03.021>.
18. Yamada, H. Amine-based capture of CO₂ for utilization and storage. *Polymer Journal* 2021, 53, 93-102, doi:10.1038/s41428-020-00400-y.

19. Chowdhury, F.A.; Okabe, H.; Yamada, H.; Onoda, M.; Fujioka, Y. Synthesis and selection of hindered new amine absorbents for CO₂ capture. *Energy Procedia* 2011, 4, 201-208, doi:<https://doi.org/10.1016/j.egypro.2011.01.042>.
20. Bougie, F.; Iliuta, M.C. Sterically Hindered Amine-Based Absorbents for the Removal of CO₂ from Gas Streams. *Journal of Chemical & Engineering Data* 2012, 57, 635-669, doi:10.1021/jc200731v.
21. Yang, H.; Xu, Z.; Fan, M.; Gupta, R.; Slimane, R.B.; Bland, A.E.; Wright, I. Progress in carbon dioxide separation and capture: a review. *J Environ Sci (China)* 2008, 20, 14-27.
22. Spigarelli, B.P.; Kawatra, S.K. Opportunities and challenges in carbon dioxide capture. *Journal of CO₂ Utilization* 2013, 1, 69-87, doi:<https://doi.org/10.1016/j.jcou.2013.03.002>.
23. Shen, X.; Du, H.; Mullins, R.H.; Kommalapati, R.R. Polyethylenimine Applications in Carbon Dioxide Capture and Separation: From Theoretical Study to Experimental Work. *Energy Technology* 2017, 5, 822-833, doi:<https://doi.org/10.1002/ente.201600694>.
24. Satyapal, S.; Filburn, T.; Trela, J.; Strange, J. Performance and Properties of a Solid Amine Sorbent for Carbon Dioxide Removal in Space Life Support Applications. *Energy & Fuels* 2001, 15, 250-255, doi:10.1021/ef0002391.
25. Nogalska, A.; Ammendola, M.; Tylkowski, B.; Ambrogi, V.; Garcia-Valls, R. Ambient CO₂ adsorption via membrane contactors - Value of assimilation from air as nature stomata. *Journal of Membrane Science* 2018, 546, 41-49.
26. Zare, A.; Perna, L.; Nogalska, A.; Ambrogi, V.; Cerruti, P.; Tylkowski, B.; García-Valls, R.; Giamberini, M. Polymer Blends for Improved CO₂ Capture Membranes. *Polymers* 2019, 11, 1662, doi:10.3390/polym11101662.
27. Morancho, J.M.; Fernández-Francos, X.; Acebo, C.; Ramis, X.; Salla, J.M.; Serra, À. Thermal curing of an epoxy-anhydride system modified with hyperbranched poly(ethylene imine)s with different terminal groups. *Journal of Thermal Analysis and Calorimetry* 2017, 127, 645-654, doi:10.1007/s10973-016-5376-z.
28. van de Witte, P.; Dijkstra, P.J.; van den Berg, J.W.A.; Feijen, J. Phase separation processes in polymer solutions in relation to membrane formation. *Journal of Membrane Science* 1996, 117, 1-31, doi:[https://doi.org/10.1016/0376-7388\(96\)00088-9](https://doi.org/10.1016/0376-7388(96)00088-9).
29. Machado, P.S.T.; Habert, A.C.; Borges, C.P. Membrane formation mechanism based on precipitation kinetics and membrane morphology: flat and hollow fiber polysulfone membranes. *Journal of Membrane Science* 1999, 155, 171-183, doi:[https://doi.org/10.1016/S0376-7388\(98\)00266-X](https://doi.org/10.1016/S0376-7388(98)00266-X).

30. Li, D.; Chung, T.-S.; Ren, J.; Wang, R. Thickness Dependence of Macrovoid Evolution in Wet Phase-Inversion Asymmetric Membranes. *Industrial & Engineering Chemistry Research* 2004, 43, 1553-1556, doi:10.1021/ie034264g.
31. Webb, P.A.; Orr, C. *Analytical Methods in Fine Particle Technology*. 1997, Micromeritics Instrument.
32. Feng, C.Y.; Khulbe, K.C.; Matsuura, T.; Ismail, A.F. Recent progresses in polymeric hollow fiber membrane preparation, characterization and applications. *Separation and Purification Technology* 2013, 111, 43-71, doi:<https://doi.org/10.1016/j.seppur.2013.03.017>.
33. Vaughan, P.; Donohue, J. The structure of urea. Interatomic distances and resonance in urea and related compounds. *Acta Crystallographica* 1952, 5, 530.
34. Campo, E.A. 1 - Polymeric Materials and Properties. In *Selection of Polymeric Materials*, Campo, E.A., Ed.; William Andrew Publishing: Norwich, NY, 2008; pp. 1-39.
35. Tsai, H.-A.; Huang, D.-H.; Ruaan, R.-C.; Lai, J.-Y. Mechanical Properties of Asymmetric Polysulfone Membranes Containing Surfactant as Additives. *Industrial & Engineering Chemistry Research* 2001, 40, 5917-5922, doi:10.1021/ie010026e.
36. Paul, D.; Yampol'skii, Y. *Polymeric gas separation membranes*; CRC Press: Baton rouge, 1994.
37. Wijmans, J.; Baker, R. The solution-diffusion model: A review. *J. Membr. Sci.* 1995, 107, 1-21.
38. Scholes, C.A.; Kentish, S.E.; Stevens, G.W. Carbon Dioxide Separation through Polymeric Membrane Systems for Flue Gas Applications. *Recent Patents on Chemical Engineering* 2008, 1, 52-66.
39. Bakeri, G.; Ismail, A.F.; DashtArzhandi, M.R.; Matsuura, T. Porous PES and PEI hollow fiber membranes in gas-liquid contacting process - A comparative study. *J. of Membr. Sci.* 2015, 475, 57-64.



Chapter 6.

General Conclusions

UNIVERSITAT ROVIRA I VIRGILI
NOVEL POLYMERIC MEMBRANES FOR ARTIFICIAL PHOTOSYNTHESIS
Alireza Zare

General conclusions

- The chemical modification of linear copolymer (Poly (epichlorohydrin-co-ethylene oxide) (PECH-co-EO)) with the dendron 3,4,5-tris[4-(n-dodecan-1-yloxy)benzyloxy] benzoate (Tap) was carried out to fabricate copolymers with two different degrees of modification, i.e. 20% (CP20) and 40% (CP40). Both modified copolymers showed a liquid crystalline columnar mesophase. According to the results, the presence of dendrons induces a main chain partial crystallization of the polyether chain, which also increases the copolymer glass transition temperature (T_g). In oriented membranes, this effect is more evident. Satisfactory orientation of the columnar channels, which should be perpendicular to the surface of the membrane, was achieved by means of thermal treatment. This technique was optimized, and the results showed that the cooling rate at which the material cooled and the temperature at which the material was annealed were two critical parameters in achieving the maximum homeotropic orientation.
- Dynamic mechanical thermal analysis (DMTA) and dielectric thermal analysis (DETA) were used to study the mobility of copolymers in both unoriented and oriented membranes. According to mechanical test results, modification with the dendron strongly hindered copolymer motions. Mechanical tests proved that the main chain required more thermal energy to become mobile and dissipate energy as the modification degree increased. DETA analysis exhibited four molecular relaxations in unmodified and modified copolymers, while some of them had different origin. DMTA and DETA showed no significant changes between unoriented and oriented membranes regardless of the degree of modification; however, due to restrictions imposed by the orientation process, the same molecular mobility and slight shifts towards higher temperatures were detected as projected.
- Membranes were characterized in terms of morphology, wettability, water uptake, methanol permeability, and transport properties. According to the findings of Atomic Force Microscopy (AFM), membrane orientation results in a significant reduction in roughness for CP20 and an increase for CP40. For both samples hydrophobicity increased with membrane orientation. Water uptake was significantly less than seen for the unmodified copolymer, being furtherly reduced on orientation. No methanol permeability was detected for both samples. The cross-section of the oriented CP40 sample was analyzed by Field emission scanning electron microscopy (FESEM) and

exhibited bundles with diameters of about 50 nm. The permeability test for oriented CP20 and CP40 revealed an evident tendency related to the present of defined cationic channels unaffected by water presence. The higher modified copolymer CP40 showed better permeability, probably due to a larger number of Tap groups supporting the column, which improved the inner structure of channels throughout the structure. The linear sweep voltammetry (LSV) technique proved proton transport through membranes. Proton had the highest cationic performance, followed by sodium/potassium and lithium cations. Besides, the higher modified copolymer CP40 demonstrated better proton transport properties. Therefore, membranes based on (PECH-co-EO) grafted with Tap, homeotropically oriented, can be employed in proton transfer devices such as artificial photosynthesis.

- In order to improve the performance of asymmetric polysulfone membrane in membrane contactors for direct air CO₂ capture, two different chemical modifications of a commercial Polyethylenimine Lupasol G20 were carried out with benzoyl chloride (mG20) and phenyl isocyanate (UG20). Modified additives (mG20 and UG20) were added in neat polysulfone (PSf) with different contents to improve direct air CO₂ capture at ambient pressure. Membranes were prepared via phase-inversion precipitation. Incorporating the modified polymeric additives into neat polysulfone determined a change in water uptake, KOH uptake, contact angle (CA), porosity, roughness, morphology, solubility, permeability, and CO₂ absorption flux. Finger-like macropores, meso- and micropores, and a thin dense layer were observed in all samples. Water uptake and KOH uptake increased in the presence of hydrophilic additives for all samples, as expected.
- The membranes prepared by blending PSf with UG20 showed no degradation upon 24 hours of soaking in KOH solution, as confirmed by FTIR and ¹H NMR. Mechanical, thermal, and dielectric analyses showed the plasticizing effect of additive, which could facilitate gas permeability. Porosity decreased as the additive content increased, whereas CO₂ solubility was improved as a result of the presence of UG20.
- Due to the presence of amine groups in the structure of the additives, the addition of additives (mG20 and UG20) into neat PSf demonstrated enhanced features in terms of mass transfer coefficient and CO₂ absorption depending on the amount and structure of the additives; however, a reverse impact was observed when higher additive amounts (more than 5%) were used. In conclusion, the performance of blend membranes in terms of CO₂ permeability and absorption was improved by both additives, while UG20 demonstrates better performance compared to mG20.

- The introduction of urea linkages in the modified Polyethylenimine Lupasol G20 is shown to be a successful strategy for the design of additives for facilitated CO₂ direct air capture using polymeric membranes

UNIVERSITAT ROVIRA I VIRGILI
NOVEL POLYMERIC MEMBRANES FOR ARTIFICIAL PHOTOSYNTHESIS
Alireza Zare



Appendices

UNIVERSITAT ROVIRA I VIRGILI
NOVEL POLYMERIC MEMBRANES FOR ARTIFICIAL PHOTOSYNTHESIS
Alireza Zare

7.1 List of publications

Directly related to the thesis:

- 1) A Zare, L. Perna, A. Nogalska, V. Ambrogi, P. Cerruti, B. Tylkowski, R. Garcia-Valls, M. Giamberini *, Polymer blends for improved CO₂ capture membranes, *Polymers*, 11, 1662 (2019).
- 2) A. Zare, B. Pascual-Jose, S. De la Flor, A. Ribes-Greus, X. Montané*, J.A. Reina, M. Giamberini*, Membranes for Cation Transport Based on Dendronized Poly(epichlorohydrin-co-ethylene oxide). Part 1: The Effect of Dendron Amount and Column Orientation on Copolymer Mobility, *Polymers*, 13, 3532 (2021).
- 3) A. Zare, X. Montané*, J.A. Reina, M. Giamberini*, Membranes for Cation Transport Based on Dendronized Poly(epichlorohydrin-co-ethylene oxide). Part 2: Membrane characterization and transport properties., *Polymers*, 13, 3915 (2021).
- 4) J. Guardià, A. Zare, J. Eleeza, M. Giamberini, J.A. Reina & X. Montané*, Synthesis and characterization of dendritic compounds containing nitrogen: monomer precursors in the construction of biomimetic membranes, *Scientific reports*, 12(1), 1725 (2022).
- 5) B. Pascual-Jose, A. Zare, S. De la Flor, J.A. Reina, M. Giamberini, A. Ribes-Greus *, Dielectric Properties in Oriented and Unoriented Membranes based on Poly(Epichlorohydrin-co-Ethylene Oxide) Copolymers: Part III, *Polymers* 14, 1369, (2022).
- 6) A. Zare, A.K. Boukalfa, A. Nogalska, A. Puga, P. Cerruti, B. Pascual-Jose, A. Ribes-Greus, M. Giamberini*, Facilitated direct air capture of CO₂ in polysulfone membrane contactors by improving stability and hydrophobicity of amine additives, *Journal of Membrane Science*, submitted.

7) A. Zare, X. Montané, J.A. Reina, M. Giamberini, Applications of membranes in sustainable energy systems: energy production and storage. Book chapter in Polymer Engineering, 2nd Edition, Edited by: Bartosz Tylkowski, Karolina Wieszczycka, Renata Jastrzab and Xavier Montane. Walter de Gruyter GmbH, Berlin/Boston, ISBN: 9783110738445, in press (available for purchase from 11/10/2022)

7.2 Meeting contributions

Congress Name: *GEP-SLAP2022*, Donostia-San Sebastián, Spain, May 2022. Poster Presentation.

Title: Synthesis and characterization of novel dendronized poly(2-oxazoline)s: precursors in the construction of biomimetic membranes.

Authors: Jordi Guardiola; Alireza Zare; Marta Giamberini; Jose Antonio Reina; Xavier Montané.

Congress Name: *GEP-SLAP2022*, Donostia-San Sebastián, Spain, May 2022. Poster Presentation.

Title: Analysis of the Dielectric Properties of Modified Polysulfone Membranes for CO₂ Capture.

Authors: Borja Pascual-José; Alireza Zare; Marta Giamberini; José Antonio Reina; Amparo Ribes-Greus.

Congress Name: *Membrane materials - modification and separation (M3-S) Conference*. Toruń, Poland, September 2021. Oral presentation.

Title: Columnar Liquid Crystalline Polymer as ion Conductive Membrane for Direct Methanol Fuel Cell.

Authors: Alireza Zare; José Antonio Reina; Marta Giamberini.

Congress Name: 14th Mediterranean Congress of Chemical Engineering (MeCCE-14), Barcelona, Spain, November 2020. Poster Presentation.

Title: Self-assembled Liquid-Crystalline Membranes for Direct Methanol Fuel Cell application.

Authors: Alireza Zare; José Antonio Reina; Marta Giamberini.

7.3 Abroad research stay

Organization: Institute for Polymers, Composites and Biomaterials (IPCB-CNR)

Supervisor: Prof. Luigi Ambrosio

City: Pozzuoli (NA) **Country:** Italy

Length: 3 months (September 2021-December 2021)

7.4 Supplementary Materials

7.4.1 Chapter 2

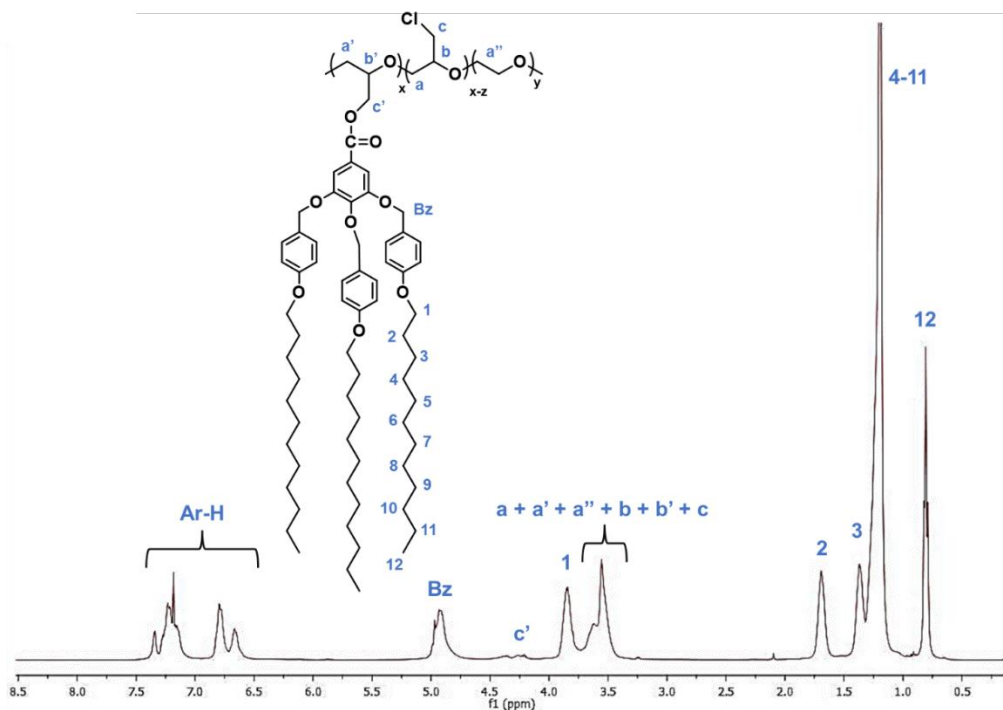


Figure 2.S1 ¹H NMR spectrum in CDCl₃ of CP40 at room temperature.

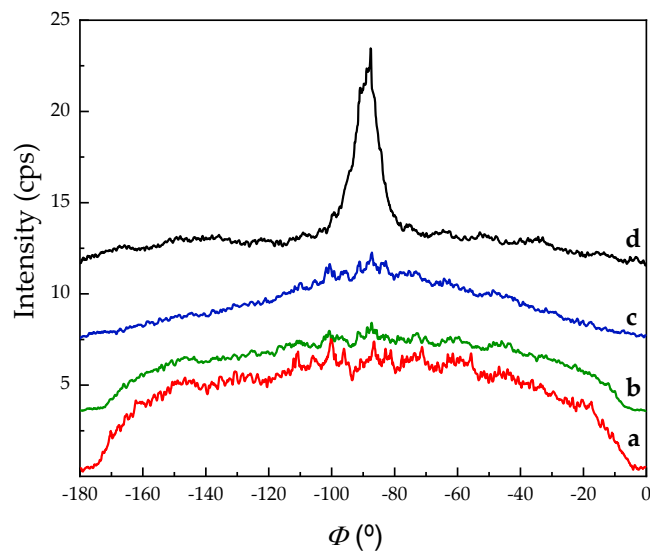


Figure 2.S2 Phi diffractograms from azimuthal scan on the reflection at $2\theta = 2.2^\circ$ of CP40 (samples (a) – (d)) after the thermal treatment with different conditions.

7.4.2 Chapter 3

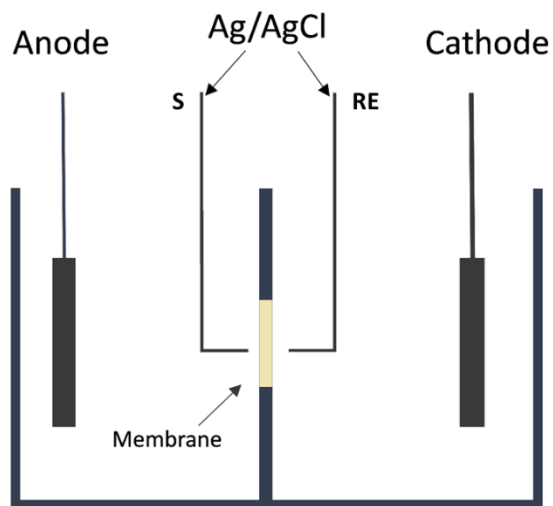


Figure 3.S1 The experimental set-up for linear sweep voltammetry measurements. Anode (+) is working electrode (WE), Cathode (-) is counter electrode (CE), S is sensitive electrode and RE is reference electrode.

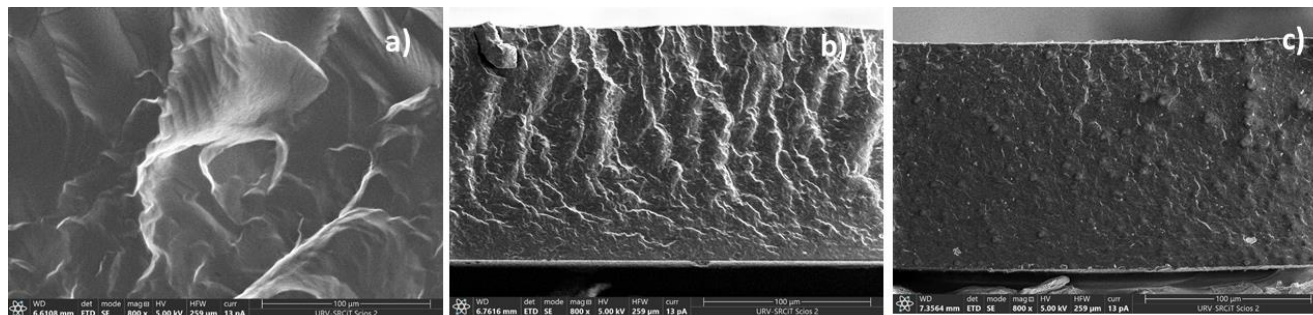


Figure 3.S2 FESEM images of the membrane cross-sections: CP0 (a); CP20 (b); CP20 oriented (c).

Table 3.S1 Water Contact angle as determined on oriented CP20 and CP40 membranes after Proton Permeability experiment (PP) and Water Uptake test (WU).

Sample	Modification (%)	Contact angle (°)	
		Oriented membrane after PP	Oriented membrane after WU
CP20	20%	106 ± 2 ^a , 107 ± 1 ^b	106 ± 2 ^a , 108 ± 3 ^b
CP40	40%	124 ± 2 ^a , 122 ± 2 ^b	130 ± 3 ^a , 130 ± 2 ^b

^a Air side; ^b Teflon side

7.4.3 Chapter 4

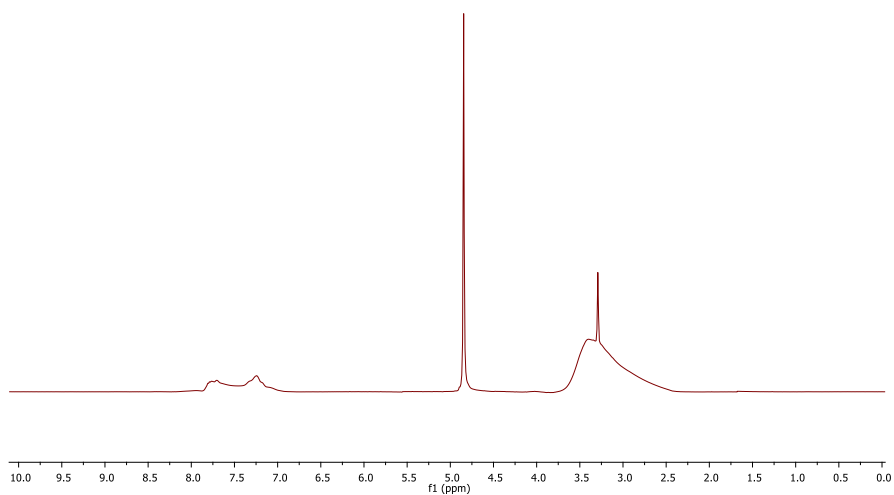


Figure 4.S1 ¹H NMR spectrum in CD₃OD of mG20

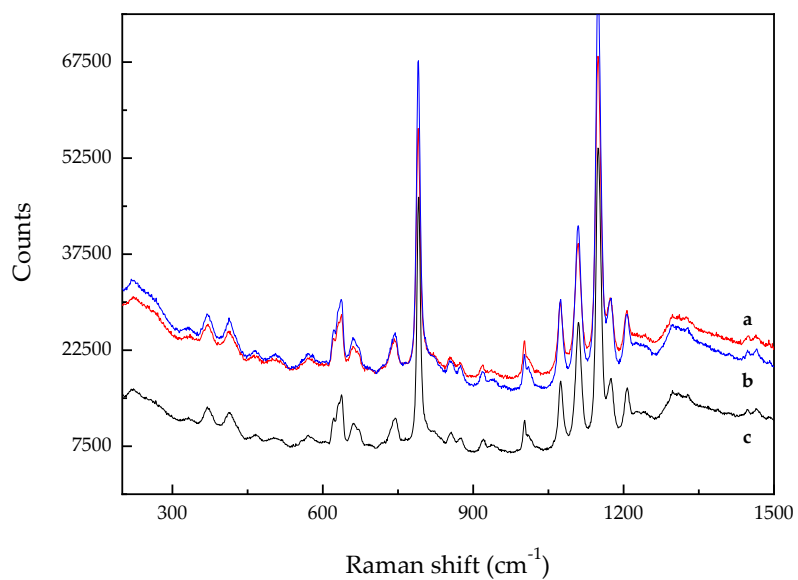


Figure 4.S2 Raman spectra between 200 and 1500 cm⁻¹ performed across the section of L20 : (a) top; (b) center; (c) bottom surface.

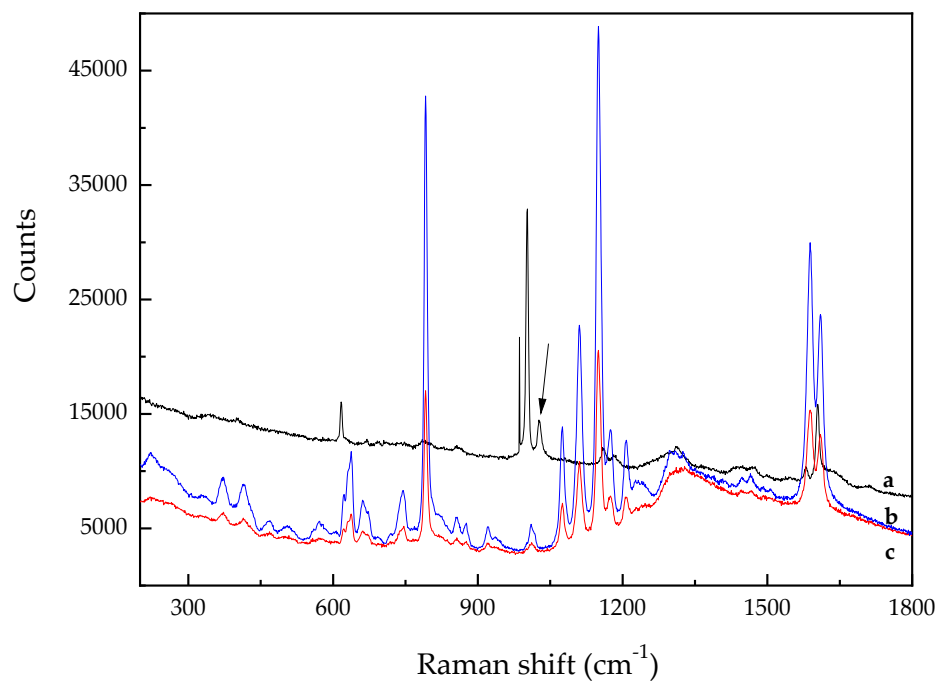


Figure 4.S3 Raman spectra between 200 and 1800 cm⁻¹ of: (a) neat mG20; (b) L10, top surface; (c) L10, bottom surface. The band at 1030 cm⁻¹ is highlighted.

7.4.4 Chapter 5

The polysulfone membranes were characterized by ^1H NMR spectroscopy on a Varian Gemini 400 spectrometer (400 MHz). Membrane samples (10-20 mg) were dissolved in dimethylformamide (DMF) together with a known amount of potassium hydrogenphthalate (5-10 mg) as the internal standard for the quantification of residual *N*-methylpyrrolidone (NMP). Dimethyl sulfoxide- d_6 (dms d_6), in a sealed co-axial capillary tube, was used as the deuterium reference external standard. The amounts of NMP were determined from the ratio of the NMP and potassium hydrogenphthalate signals (δ : 1.93 and 7.49 ppm, respectively) after baseline correction. For the determination of additive (modified Lupasol), a similar procedure was followed, but simply dissolving the membrane samples in dimethylformamide- d_6 (dmf- d_6).

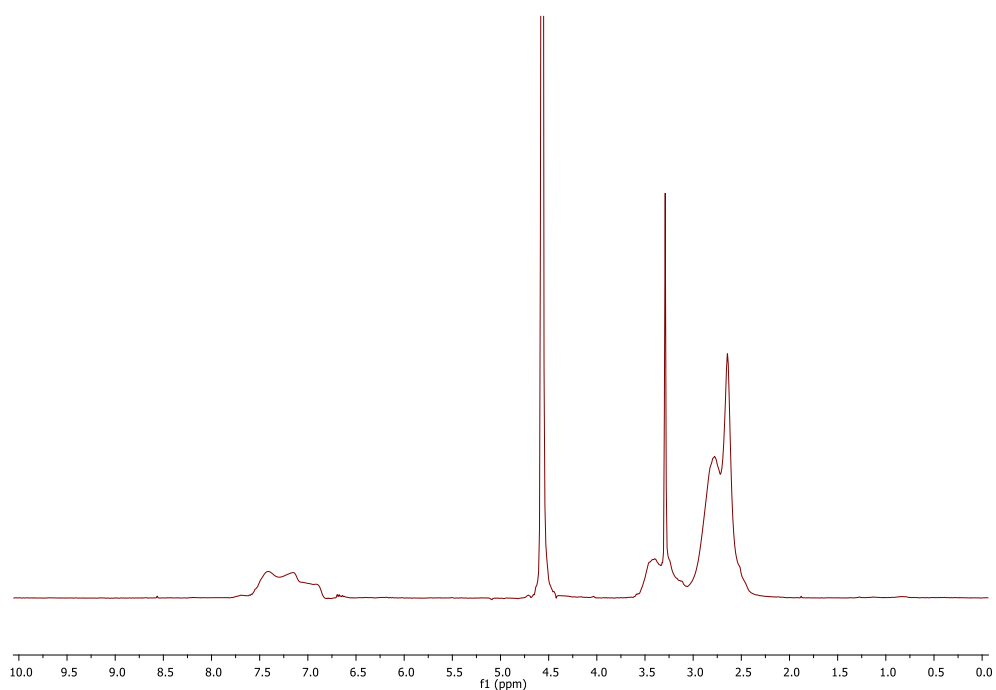


Figure 5.S1 ^1H NMR spectrum in CD_3OD of UG20.

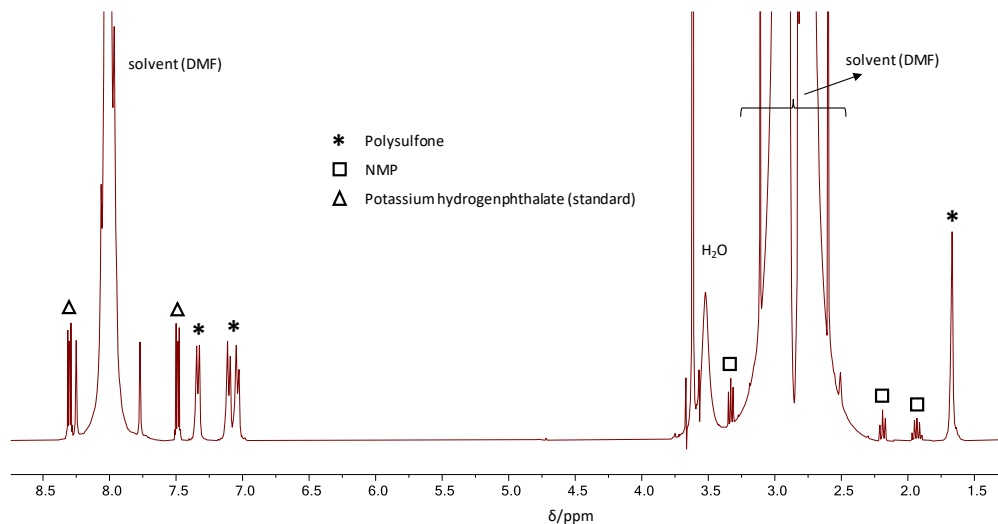


Figure 5.S2 A typical ^1H NMR spectrum (in DMF, potassium hydrogen phthalate as internal standard, $\text{dms}\text{-d}_6$ as external standard, 400 MHz) of M0 membrane sample. The amount of residual NMP was determined as 7.4% by mass relative to PSf.

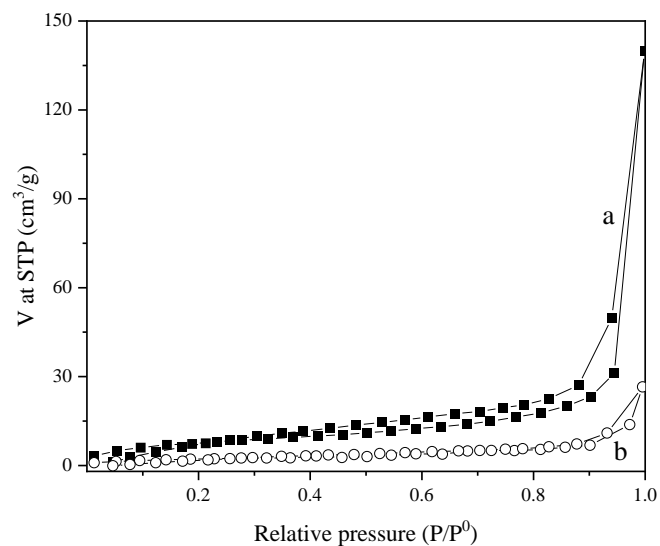


Figure 5.S3 Adsorption isotherms of (a) M0 and (b) M10.

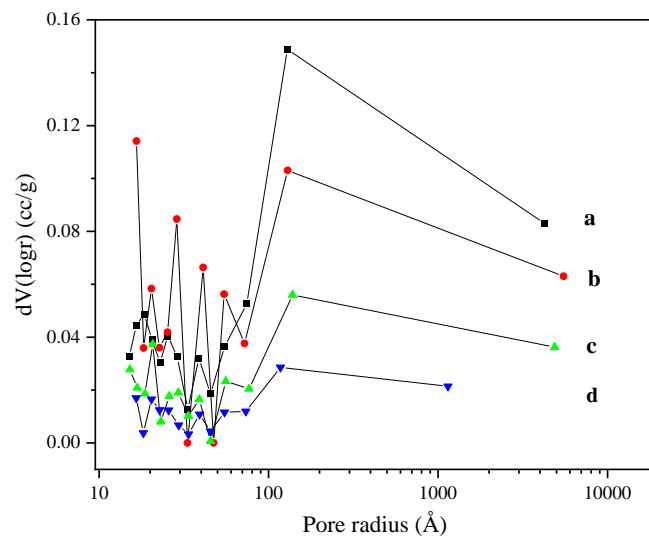


Figure 5.S4 Pore volume distribution of: (a) M0; (b) M2; (c) M5; (d) M10.

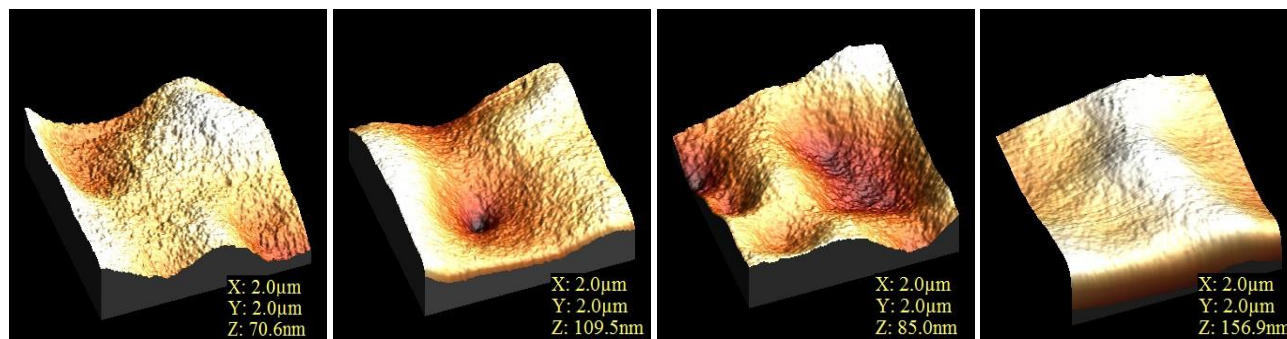


Figure 4.S5 Atomic Force Microscopy (AFM) 3-Dimensional topographical images of bottom side of studied membranes: (a) M0; (b) M2; (c) M5; (d) M10.

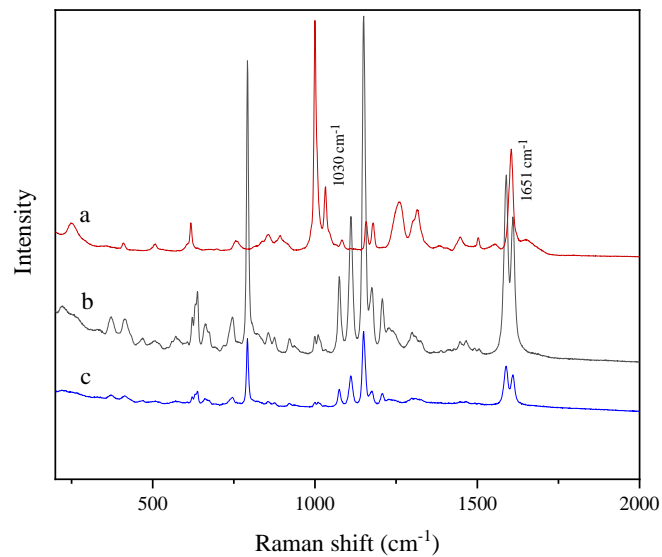


Figure 5.S6 Raman spectra between 200 and 2000 cm⁻¹ of: (a) pure UG20; (b) top surface of M10; (c) neat PSf M0. Bands are highlighted by their values.

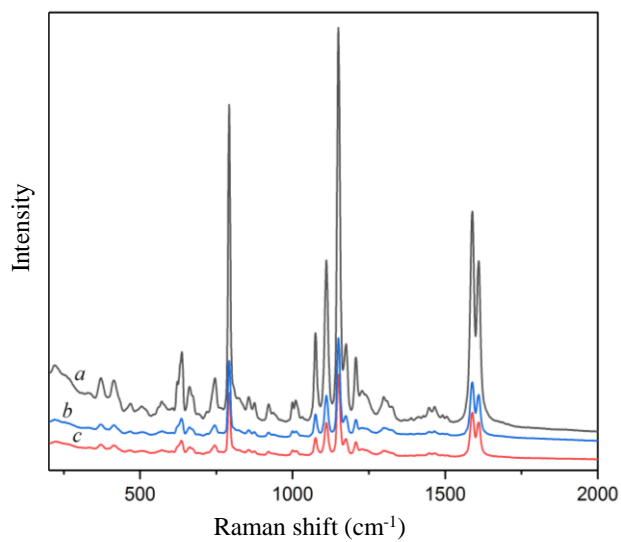


Figure 5.S7 Raman spectra between 200 and 2000 cm⁻¹ of M10 at different layers: (a) bottom surface; (b) center; (c) top surface.

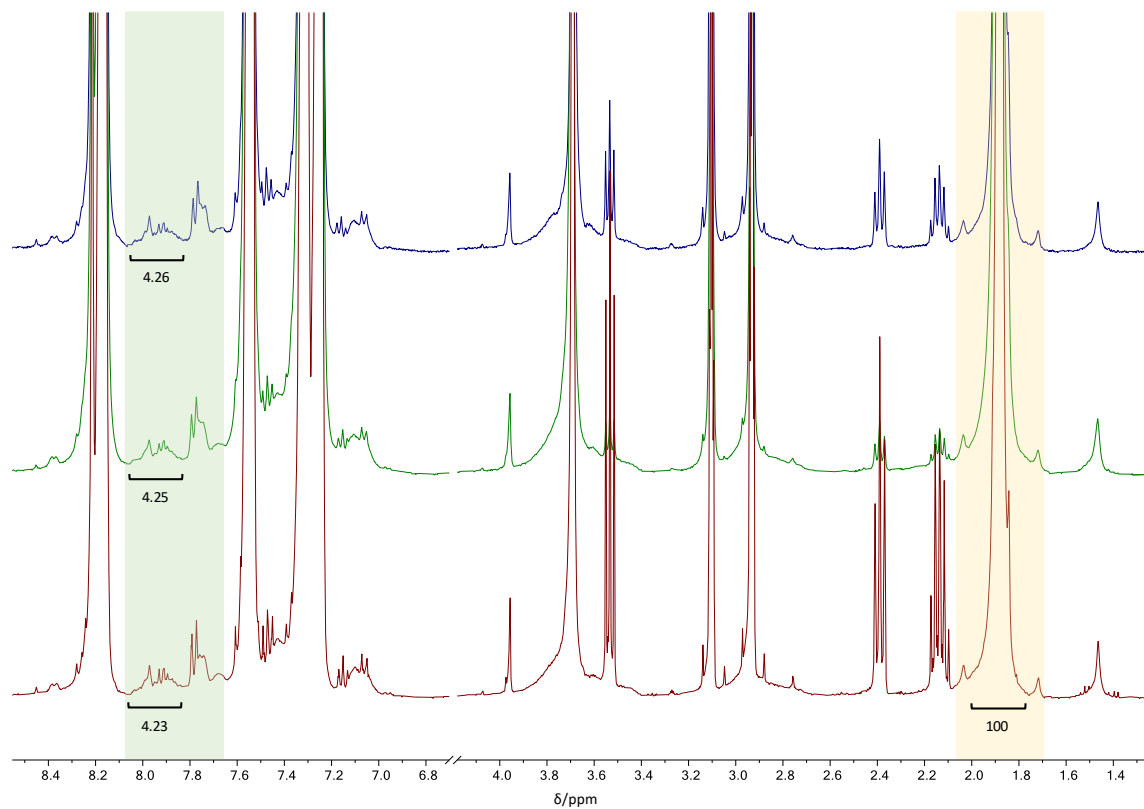


Figure 5.S8 Stacked ¹H NMR spectra (in dmf-d₆, 400 MHz) of polysulfone membrane samples with 10% additive: as-prepared (red trace), after treatment in an aqueous KOH solution (green trace) and after treatment in water (blue trace). Top: Green- and yellow-shaded areas indicate the regions of additive and polysulfone signals, respectively; no apparent change in additive signals qualitatively suggest its stability under the treatment conditions. Bottom: quantification of additive signals (8.06-7.82 ppm) relative to a reference polysulfone signal (1.88 ppm), showing no significant reduction, confirm additive stability.

UNIVERSITAT ROVIRA I VIRGILI
NOVEL POLYMERIC MEMBRANES FOR ARTIFICIAL PHOTOSYNTHESIS
Alireza Zare



This project has received funding from the European Union's Horizon 2020 research and innovation programme under the Marie Skłodowska-Curie grant agreement No. 713679 and from the Universitat Rovira i Virgili (URV).